

ABSTRACT

BURLEYSON, CASEY DALE. Environmental Controls on Stratocumulus Cloud Fraction. (Under the direction of Dr. Sandra E. Yuter).

Marine stratocumulus clouds are widespread, low, optically thick, and persist for long periods of time. Their high albedo allows stratocumulus clouds to reflect large amounts of incoming shortwave radiation. Understanding the processes that lead to changes in stratocumulus cloud fraction is critically important in capturing the effects of stratocumulus in global climate models (GCMs). This research presents two analyses which seek to better understand the governing processes that drive variability in the stratocumulus-topped boundary layer system.

The diurnal cycle of marine stratocumulus in cloud-topped boundary layers is examined using ship-based meteorological data obtained during the 2008 VAMOS Ocean-Cloud-Atmosphere-Land Study Regional Experiment (VOCALS-REx). The high temporal and spatial continuity of the ship data, as well as the 31-day sample size, allows us to resolve the diurnal transition in degree of coupling of the stratocumulus-topped boundary layer. The amplitude of diurnal variation was comparable to the magnitude of longitudinal differences between regions east and west of 80°W for most of the cloud, surface, and precipitation variables examined. The diurnal cycle of precipitation is examined in terms of areal coverage, number of drizzle cells, and estimated rain rate. East of 80°W, the drizzle cell frequency and drizzle area peaks just prior to sunrise. West of 80°W, total drizzle area peaks at 3:00 am, 2-3 hours before sunrise. Peak drizzle cell frequency is three times higher west of 80°W compared to east of 80°W. The waning of drizzle several hours prior to the ramp up of shortwave fluxes may be related to the higher peak drizzle frequencies in the west. The ensemble effect of localized subcloud evaporation of precipitation may make drizzle a self-limiting process where the areal density of drizzle cells is sufficiently high. The daytime reduction in vertical velocity variance in a less coupled boundary layer is accompanied by enhanced stratification of potential temperature and a buildup of moisture near the surface.

We also present an analysis of patterns of cloud fraction variability on a variety of time scales ranging from seasonal to sub-diurnal. The goal of this analysis is to understand which modes of variability, and thus the processes that drive variability on that time scale, may be more or less important to capturing the total variations in cloud fraction. We developed for marine regions of predominantly low cloud a novel method to separate infrared brightness temperatures measured by geostationary satellites into cloudy and cloud free pixels. The resulting cloud identification maps have a native spatial resolution of 4 km x 4 km and are available every 30 minutes from 2003-2010. Analysis of the low cloud frequency dataset shows that the diurnal cycle of low cloud fraction within a given season and region unfolds in a very regular manner. The largest diurnal cycles occur on the edges of the cloud deck where cloud fractions are generally lower. Large scale decreases in cloudiness overnight, such as those that would occur with the formation of pockets-of-open cells, occur infrequently. Total cloud fraction at sunrise is on average only a few percent lower than the maximum that occurs overnight whereas the average cloud breakup during the day is an order of magnitude larger. We show that up to 50% of the total variance of cloud fraction on 30 minute time scales can be explained solely by the time of day and day of the year. In order to improve simulation of stratocumulus within GCMs, models should be able to replicate the processes leading to variability on seasonal and diurnal time scales.

© Copyright 2013 by Casey Dale Burleyson

All Rights Reserved

Environmental Controls on Stratocumulus Cloud Fraction

by
Casey Dale Burleyson

A dissertation submitted to the Graduate Faculty of
North Carolina State University
in partial fulfillment of the
requirements for the degree of
Doctor of Philosophy

Marine, Earth, and Atmospheric Sciences

Raleigh, North Carolina

2013

APPROVED BY:

Sandra Yuter
Committee Chair

David Mechem

Matthew Parker

Walter Robinson

DEDICATION

To Mom, Dad, Joy, Aaron, and Jared
Without whom this simply would not have been possible.

BIOGRAPHY

Important Things

Family, friends, books, coffee, curiosity, and the score in the Braves game.

ACKNOWLEDGMENTS

I owe a large debt of gratitude to Dr. Sandra Yuter for taking a chance on me as an undergraduate research assistant and for maintaining faith in me throughout my graduate career. I have yet to cross paths with an advisor who works harder or more thoughtfully to develop well-rounded, capable, and happy scientists. Additional thanks are owed to members of my committee: Dr. David Mechem, Dr. Matthew Parker, and Dr. Walter Robinson for timely and constructive feedback along the way and to Dr. Simon de Szoeki for critical analysis of my work over the past several years. My friends and colleagues, both current and alumni, in the Clouds and Precipitation Processes and Patterns group have made it pleasant to come to work each and every day and for that I am grateful. And lastly I would like to acknowledge my friends and especially my family. Your love, support, encouragement, food, and infinite patience listening to me ramble on about persistent clouds in distant places means more to me than you will ever know.

TABLE OF CONTENTS

LIST OF TABLES	vii
LIST OF FIGURES	viii
Chapter 1 Introduction	1
Chapter 2 The Diurnal Cycle of Marine Stratocumulus Clouds and Precipitation	3
2.1 Introduction.....	3
2.2 Data and Methods	6
2.3 Results.....	8
2.3.1 Boundary Layer Mixing.....	8
2.3.2 Surface Variables	12
2.3.3 Cloud Measurements	15
2.3.4 Precipitation	16
2.4 Conclusions.....	21
2.5 Chapter 2 Figures	25
Chapter 3 Environmental Controls on Stratocumulus Cloud Fraction	38
3.1 Introduction.....	38
3.2 Data and Methods	48
3.2.1 Description of the Cloud Identification Methodology.....	48
3.2.2 Evaluation of the Cloud Identification Methodology	52
3.2.3 Other Limitations	56
3.2.4 Environmental Variables	57
3.3 Results.....	58
3.3.1 Annual Mean Low Cloud Fraction	58
3.3.2 Seasonal Cycles in Low Cloud Fraction.....	59
3.3.3 Interannual Variability in Low Cloud Fraction	60
3.3.4 Diurnal Cycles in Low Cloud Fraction.....	61
3.3.4.1 Areal Patterns.....	61

3.3.4.2 Rates of Change	63
3.3.4.3 Net Changes	66
3.3.5 Environmental Characteristics When Cloud Fraction Decreases	
Overnight	71
3.3.6 Environmental Sensitivity Tests	73
3.4 Discussion	76
3.5 Conclusions.....	80
3.6 Chapter 3 Tables	83
3.7 Chapter 3 Figures	86
Chapter 4 Conclusions and Future Work	131
4.1 Conclusions.....	131
4.2 Future Work.....	136
REFERENCES.....	137
APPENDICES.....	151
Appendix A Peak and Minimum Season Mean Diurnal Cycle Images.....	152
Appendix B A 10-Year Examination of Precipitation Around Lake Victoria.....	158
B.1 Introduction	158
B.2 Data and Methods.....	159
B.3 Results	160
B.3.1 Diurnal Cycle of Precipitation Frequency.....	160
B.3.2 Seasonal Cycle of Precipitation Frequency.....	162
B.3.3 Differences in Precipitation Over Land Verses	
Over The Lake	163
B.4 Conclusions and Future Work.....	164
B.5 Appendix B References.....	165
B.6 Appendix B Figures	167

LIST OF TABLES

Table 3.1	A simplified summary of some the processes which have been demonstrated to modify stratocumulus cloud fraction (CF).	83
Table 3.2	A summary of the data sources to be used in my analysis.	84
Table 3.3	The variance explained by the seasonal and diurnal cycles from a simple empirical model. Cloud fractions are calculated in the 3° x 3° boxes shown in Fig. 3.10.	85

LIST OF FIGURES

Figure 2.1	Distribution of sampling in space (a) and time (b) of hours of C-band radar data collected aboard the <i>RHB</i> . Data collected west of 80°W is displayed in pink whereas data collected east of 80°W is shown in blue.	25
Figure 2.2	Time-height profiles of the mean vertical velocity variance in the boundary layer for the region east (a) and west (b) of 80°W using data from the vertically-pointing Doppler lidar. The profiles are normalized to the base of the cloud such that a height of 1.0 represents the base of the cloud and a value of 0.2 represents a height that is 20% of the measured cloud base height. Individual data points with a signal-to-noise ratio greater than 15 dB are removed to limit the influence of precipitation on the turbulence statistics.....	26
Figure 2.3	Four hour averages of the vertical profiles of potential temperature (a), water vapor mixing ratio (b), and horizontal wind speed (c) from the soundings launched from the <i>RHB</i> . The profiles use the local solar time and are normalized to the base and top of the cloud to capture the relative heights of boundary layer mixing properties. The contour intervals are every 0.15 K for potential temperature, 0.2 g kg ⁻¹ for water vapor mixing ratio, and 0.5 m s ⁻¹ for wind speed.	27
Figure. 2.4	Time-height variation of range-corrected backscatter intensity from a vertically-pointing Doppler lidar aboard the <i>RHB</i> (a) and select RHI scans from the lidar at 6:00 am (b) and 6:00 pm (c) local time. Data shown was collected on 2 Nov 2008 near 19.6°S and 74.8°W. We plotted the 10-minute blocks of vertically-pointing data, obtained every 20 minutes, close together to make the figure easier to display.	28

Figure 2.5	Hourly mean (solid line) and interquartile range (shaded region) of the near surface air temperature (a), dew point temperature (b), wind speed (c), wind direction (d), incoming shortwave radiation (e), and incoming longwave radiation (f) from an upward-pointed sensor, plotted as a function of local time for regions east and west of 80°W.	29
Figure 2.6	Hourly mean and interquartile range of near-surface aerosol concentrations for aerosols smaller than 0.1 μm diameter (roughly Aitken mode; a) and aerosols larger than 0.1 μm diameter (roughly accumulation mode; b) for regions east and west of 80°W.	30
Figure 2.7	Hourly mean and interquartile range of cloud base heights measured by the laser ceilometer (a), cloud top heights measured by interpolating the inversion height measured by the soundings taken every four hours (b), and the resultant depths of the cloud (c) for regions east and west of 80°W.	31
Figure 2.8	Hourly mean and interquartile range of the observed liquid water path (a) and the adiabatic liquid water path derived from the cloud base and height measurements (b) for regions east and west of 80°W.	32
Figure 2.9	Diurnal variation of the mean number of drizzle cells per scan (a), mean total precipitation area per scan (b), mean (solid line) and interquartile range (shaded region) of the hourly areal-average rain rate (c), and mean (solid line) and interquartile range (shaded region) of the hourly conditional rain rate (d), derived from measurements from the scanning C-band precipitation radar aboard the RHB.	33
Figure 2.10	Distribution of drizzle cell areas for all precipitation observed during VOCALS-REx for the regions east (a) and west (b) of 80°W. The vertical axis is on a logarithmic scale.	35
Figure 2.11	Boundary layer profiles of potential temperature (black lines) and relative humidity (red lines) measured by consecutive atmospheric soundings launched at 9:45 pm on 22 November 2008 (a) and 2:30 am	

	(b) on 23 November 2008. Horizontal dotted black lines show the approximate boundaries of the cloud at the time the measurement was taken. The soundings were launched from the <i>RHB</i> while it was stationed at roughly 20°S and 84.5°W. Radar reflectivity for the corresponding times is shown in panels (c) and (d).36	36
Figure 2.12	Conceptual model showing the most common states of the stratocumulus cloud deck over the diurnal cycle. Precipitation (solid dots), surface mixed layer depth (shaded and dotted region), and turbulent mixing (circulating arrows) all vary regularly across the day.37	37
Figure 3.1	Time series of shortwave (red lines) and longwave (blue lines) radiative flux reaching the surface on a mostly cloudy day (top panel; from 11-Nov 2008 near 75°W and 20°S) and on a day when the cloud completely breaks up during the afternoon (bottom panel; from 23-Nov 2008 near 83°W and 21°S). Data were collected aboard the <i>RHB</i> during VOCALS-REx.86	86
Figure 3.2	Infrared brightness temperatures over the southeast Pacific stratocumulus deck at 1400 UTC on 16-November 2008 (left) and the bimodal distribution of brightness temperatures for the scene (right).87	87
Figure 3.3	Two examples of the accumulated brightness temperature distributions in 3°x3° boxes over the southeast Pacific. The top panel shows an example of a region well offshore where the cloud fractions are lower and the distribution of daytime temperatures more bimodal. In contrast, the distributions shown in the bottom panel come from an area closer to the coast where cloud fractions remain high even during the day, resulting in a mostly unimodal distribution of brightness temperatures.88	88
Figure 3.4	In the top row are brightness temperatures from the merged-IR dataset over the SE Pacific at 1600 UTC on 11-October 2008. The middle row contains the corresponding total cloud map generated using the new	

cloud identification methodology. The merged-IR cloud map can be compared with the GOES visible albedo shown in the bottom row. The right column shows the $8.5^\circ \times 8.5^\circ$ region that is outlined in blue in the left column.89

Figure 3.5 Merged-IR (lines) and MODIS (diamonds) total cloud fraction for $3^\circ \times 3^\circ$ boxes in each of the stratocumulus regions for the period between 4-January and 11-January 2004. MODIS pixels with fractional cloudiness greater than 0.87 are classified as cloud in the raw MODIS swaths before calculating cloud fraction to create a more direct comparison.91

Figure 3.6 An example of scenes where the merged-IR cloud identification method overestimates cloud fraction by 10% compared to the MODIS total cloud fraction (left column; 4-January 2004 at 10:00 UTC), is a perfect match (center column; 8-January 2004 at 09:30 UTC), and underestimates total cloud fraction by 10% (right column; 8-January 2004 at 22:00 UTC). The top row shows the merged-IR brightness temperatures while the merged-IR and MODIS cloud masks are in the middle and bottom rows respectively.92

Figure 3.7 Distribution of the difference between the MODIS and merged-IR total cloud fraction (left) and the cumulative frequency of the difference (right) for multiple $3^\circ \times 3^\circ$ boxes spanning an east-west gradient from 21°N to 24°N in the NE Pacific, 21°S to 18°S in the SE Pacific, and 15°S to 12°S in the SE Atlantic. Distributions are collected from roughly 5000 MODIS overpasses between 2003 and 2010.93

Figure 3.8 Data density diagram showing the frequency of occurrence of a differences between the MODIS and merged-IR total cloud fraction conditioned on the value of the observed MODIS cloud fraction in the NE Pacific (top left), SE Pacific (bottom left), and SE Atlantic (bottom

	right). Darker colors indicate more frequent occurrences. The solid black line in each plot indicates the mean difference for a given MODIS cloud fraction.94	94
Figure 3.9	Distribution of the difference between the MODIS and merged-IR total cloud fraction during daytime overpasses (left column) and nighttime overpasses (right column) for multiple 3° x 3° boxes spanning an east-west gradient from 21°N to 24°N in the NE Pacific, 21°S to 18°S in the SE Pacific, and 15°S to 12°S in the SE Atlantic.95	95
Figure 3.10	Annual mean total cloud fraction from the MODIS cloud product (left) and from the merged-IR cloud identification method (right) in the NE Pacific (top row), SE Pacific (middle row), and SE Atlantic (bottom row). Contours in the left hand column are the frequency (%) of cloud top temperatures colder than 273 K. The merged-IR data is taken only from times of a corresponding MODIS overpass (i.e. the 30 minute scene closest to the MODIS overpass). Boxes in the right column show the 3° x 3° boxes in which low cloud fraction was calculated for the time series analysis in the remainder of the chapter.96	96
Figure 3.11	The mean MODIS (top row) and merged-IR (bottom row) total cloud fraction for each of the four seasons (columns) in the NE Pacific. MODIS pixels with fractional cloudiness greater than 0.87 are classified as cloud in the raw MODIS swaths before calculating cloud fraction to create a more direct comparison. The merged-IR data is taken only from times of a corresponding MODIS overpass (i.e. the 30 minute scene closest to 1:30 am/pm). The solid line indicates regions of merged-IR data without the zenith angle correction error and where cloud top temperatures colder than 273 K occur less than 35% of the time.97	97
Figure 3.12	As in Figure 3.11 but for the SE Pacific.98	98
Figure 3.13	As in Figure 3.11 but for the SE Atlantic.99	99

Figure 3.14	Mean cloud fraction over all seasons at night (left two columns) and during the day (right two columns) in the NE Pacific (top row), SE Pacific (middle row), and SE Atlantic (bottom row). The merged-IR data is taken only from times of a corresponding MODIS overpass (i.e. the 30 minute scene closest to 1:30 am/pm). The solid line indicates regions of merged-IR data without the zenith angle correction error and where cloud top temperatures colder than 273 K occur less than 35% of the time.	100
Figure 3.15	Infrared brightness temperatures observed off the coast of California at 14:00 UTC on 10-Oct 2008. An example of the zenith angle correction error can be seen in the arcs of lower brightness temperatures within the blue box.....	101
Figure 3.16	Mean merged-IR cloud fraction for each season (column) in the NE Pacific (top row), SE Pacific (middle row), and SE Atlantic (bottom row). Overlaid on each plot are contours of the seasonal mean lower tropospheric stability (K) from ECMWF reanalysis.	102
Figure 3.17	Mean lower tropospheric stability (x-axis) and low cloud fraction (y-axis) for each of the four seasons (symbols). The solid black line indicates the best fit relationship and the dotted gray line is the best fit relationship found in Klein and Hartmann (1993). Data are shown for the NE Pacific [130°W:120°W, 20°N:30°N], SE Pacific [90°W:80°W, 20°S:10°S], and SE Atlantic [0°:10°E, 20°S:10°S].....	103
Figure 3.18	Top - Time series of monthly mean low cloud fraction with the mean annual cycle removed in the NE Pacific (blue line) and SE Pacific (green line) and the Niño 3.4 Index anomaly. Bottom - Time series of monthly mean lower tropospheric stability with the mean annual cycle removed in the NE Pacific (blue line) and SE Pacific (green line) and the Niño 3.4 Index anomaly. Cloud fraction and stability were calculated in the box [130°W:120°W, 20°N:30°N] in the NE Pacific	

	and [90°W:80°W, 20°S:10°S] in the SE Pacific. Correlations for each time series are given in the legend.....	104
Figure 3.19	Hourly mean cloud fractions across the diurnal cycle during the minimum cloudiness season (December-January-February) in the SE Pacific. The local solar time is given at the top of each plot.	105
Figure 3.20	Frequency distribution of low cloud fraction across the diurnal cycle during the peak (left column) and minimum (right column) cloudiness seasons in NE Pacific (top row), SE Pacific (middle row), and SE Atlantic (bottom row). Cloud fractions are the total low cloud fraction in the 3° x 3° boxes shown in Figure 3.10. In all panels the solid black lines indicate the 10 th and 90 th percentiles of the hourly distribution while the dotted black line indicates the hourly mean.....	106
Figure 3.21	Frequency distribution of the rate of change of low cloud fraction between subsequent 30 minute scenes across the diurnal cycle during the peak (left column) and minimum (right column) cloudiness seasons in NE Pacific (top row), SE Pacific (middle row), and SE Atlantic (bottom row). Cloud fractions are the total low cloud fraction in the 3° x 3° boxes shown in Figure 3.10. In all panels the solid black lines indicate the 10 th and 90 th percentiles of the hourly distribution while the dotted black line indicates the hourly mean.....	107
Figure 3.22	Data density diagrams showing the change of cloud fraction (y-axis) in three hour windows across the diurnal cycle conditioned on the starting cloud fraction (x-axis). Cloud fractions are calculated every 30 minutes in the 3° x 3° boxes shown in Figure 3.10. Darker colors indicate more frequent occurrences. In all panels the solid black lines indicate the 10 th and 90 th percentiles of the change distribution for a given starting cloud fraction while the dotted black line indicates the mean.....	108
Figure 3.23	As in Figure 3.22 but for the SE Pacific.	109

Figure 3.24	As in Figure 3.22 but for the SE Atlantic.	110
Figure 3.25	Data density diagrams showing the distribution of cloud fraction at dusk (y-axis) conditioned on the cloud fraction at dawn (x-axis). Cloud fractions are calculated in the 3° x 3° boxes shown in Figure 3.10. Darker colors indicate more frequent occurrences. In all panels the solid black lines indicate the 10 th and 90 th percentiles of the change distribution for a given starting cloud fraction while the dotted black line indicates the mean.....	111
Figure 3.26	Data density diagrams showing the distribution of cloud fraction at dawn (y-axis) conditioned on the cloud fraction at dusk (x-axis). Cloud fractions are calculated in the 3° x 3° boxes shown in Figure 3.10. Darker colors indicate more frequent occurrences. In all panels the solid black lines indicate the 10 th and 90 th percentiles of the change distribution for a given starting cloud fraction while the dotted black line indicates the mean.....	112
Figure 3.27	Frequency of cloud fraction changes overnight conditioned on the cloud fraction at dusk (x-axis). Cloud fractions are calculated in the 3° x 3° boxes shown in Figure 3.10.	113
Figure 3.28	Probability (top) and cumulative (bottom) distribution plots of the change in cloud fraction overnight in the NE Pacific (blue line), SE Pacific (green line), and SE Atlantic (red line). Cloud fractions are calculated in the 3° x 3° boxes shown in Figure 3.10.	114
Figure 3.29	Distributions of cloud fraction in three hour time windows after dawn for mean cloud fractions at dawn (5:00 am – 6:00 am) greater than 95% (far left column), between 75% and 95% (center left column), between 50% and 75% (center right column), and less than 50% (far right column). Data are shown for the NE Pacific (top row; [132.5°W:122.5°W, 17.5°N:27.5°N]), SE Pacific (middle row, [87.5°W:77.5°W, 22.5°S:12.5°S]), and SE Atlantic (bottom row,	

	[2.5°W:7.5°E, 20°S:10°S]). For each distribution the open square shows the median value while the filled circle shows the mean value.	115
Figure 3.30	The distribution of total cloud fraction at sunset compared to the maximum total cloud fraction at any point during the day (top) and the distribution of cloud fraction at sunrise compared to the maximum total cloud fraction at any point overnight (bottom).	116
Figure 3.31	Frequency of cloud fraction decreasing (left column), decreasing more than 10% (center column), and decreasing more than 20% (right column) overnight in the NE Pacific (top row), SE Pacific (middle row), and SE Atlantic (bottom row).	117
Figure 3.32	Top Row – Fraction of all overnight time series that have a net overnight increase in cloud fraction (black bars), net decrease (orange bars), net decrease greater than 10% (purple bars), and net decrease greater than 20% (cyan bars). Bottom Row – The distribution of drizzle area (bottom left), cloud top temperature (bottom center), and lower tropospheric stability (bottom right) for time series that have a net increase (black lines), net decrease (orange lines), net decrease greater than 10% (purple lines), and net decrease greater than 20% (cyan lines). Data are from 25 3° x 3° boxes in the NE Pacific.....	118
Figure 3.33	As in Figure 3.32 but for 28 3° x 3° boxes in the SE Pacific.	119
Figure 3.34	As in Figure 3.32 but for 28 3° x 3° boxes in the SE Atlantic.....	120
Figure 3.35	The frequency distribution of changes in low cloud fraction 1 hour (left column), 3 hours (center column), and 5 hours (right column) after a MODIS overpass. The frequency distributions are conditioned on the value on the x-axis. On each x-axis we show the percentile of a given environmental variable observed for the same 3° x 3° box. The top row shows the sensitivity to drizzle area, the middle row shows the sensitivity to cloud top temperature (low percentiles are shallow	

	clouds and high percentiles are deeper clouds), and the bottom row shows the sensitivity to lower tropospheric stability.	121
Figure 3.36	Each plot contains the same underlying data in Figure 3.35 but with the overall mean cloud fraction change distribution subtracted out. This shows the deviation from the mean value with red indicating more frequent than the overall mean and blue showing less frequent than the overall mean.	122
Figure 3.37	As in Figure 3.35 but for the SE Pacific.	123
Figure 3.38	As in Figure 3.36 but for the SE Pacific.	124
Figure 3.39	As in Figure 3.35 but for the SE Atlantic.	125
Figure 3.40	As in Figure 3.36 but for the SE Atlantic.	126
Figure 3.41	Probability (top) and cumulative (bottom) distributions of the absolute difference between the measured cloud fraction and that predicted by a simple model that predicts cloud fraction based solely on time of day and the day of the year. Cloud fractions are calculated every 30 minutes in the 3° x 3° boxes shown in Figure 3.10. Data are shown for the NE Pacific (blue line), SE Pacific (green line), and SE Atlantic (red line).	127
Figure 3.42	Percent of the total variance explained by a simple model that predicts cloud fraction based on the time of day and day of year. Cloud fractions are calculated in the 3° x 3° boxes shown in Figure 3.10.	128
Figure 3.43	Left – Figure 11b from Wyant et al. (2010) showing the mean diurnal cycle in various GCMs (colored and dashed lines) and from point measurements of longwave radiative flux from an ocean buoy at 85°W and 20°S (black line). The buoy cloud fractions are the mean value during September-October-November from 2001-2005. Right – The mean merged-IR cloud fraction calculated over the buoy in September-October-November from 2003-2005 (black line) and the predicted cloud fraction (blue line). Cloud fractions were predicted	

	using a multivariate polynomial regression, built only from values for the time of day and the day of the year, based on all available data from 2003-2010.	129
Figure 3.44	Standard deviation of the 700 hPa vertical velocity from ECMWF reanalysis for each season (column) in the NE Pacific (top row), SE Pacific (middle row), and SE Atlantic (bottom row). Black lines outline the 3° x 3° boxes in which low cloud fraction was calculated and are the same as in Figure 3.10.	130
Figure A.1	Hourly mean cloud fractions across the diurnal cycle during the peak cloudiness season in the NE Pacific.	152
Figure A.2	Hourly mean cloud fractions across the diurnal cycle during the minimum cloudiness season in the NE Pacific.	153
Figure A.3	Hourly mean cloud fractions across the diurnal cycle during the peak cloudiness season in the SE Pacific.	154
Figure A.4	Hourly mean cloud fractions across the diurnal cycle during the minimum cloudiness season in the SE Pacific.	155
Figure A.5	Hourly mean cloud fractions across the diurnal cycle during the peak cloudiness season in the SE Atlantic.	156
Figure A.6	Hourly mean cloud fractions across the diurnal cycle during the minimum cloudiness season in the SE Atlantic.	157
Figure B.1	Elevation in the Lake Victoria region of East Africa. Data are from the Global Land One-km Base Elevation (GLOBE) Project and are gridded at a 1-km spatial resolution.	167
Figure B.2	Mean precipitation frequency in 3-hour increments across the diurnal cycle. Brown lines are contours of elevation at 750 m intervals. Frequency is defined as the number of rainy pixels divided by the total number of TRMM overpasses at a given pixel. Wind vectors are surface wind speed and direction from the ECMWF reanalysis dataset.	168

Figure B.3 Monthly mean precipitation frequency over the lake (blue line) and over the surrounding land (red line) with select months shown in the bottom panel. Averaging for the pixels over the lake and over land is done within the black box shown panels b-d. Brown lines are contours of elevation at 750 m intervals. Frequency is defined as the number of rainy pixels divided by the total number of TRMM overpasses at a given pixel. Wind vectors are surface wind speed and direction from the ECMWF reanalysis dataset.170

Figure B.4 Distribution of reflectivities for rainy pixels over water (blue lines) and land (red lines) on and around Lake Victoria. The solid lines indicated the distribution of near-surface reflectivity values while the dotted lines indicated the distribution of intensities measured at 6 km. Averaging for the pixels over the lake and over land is done within the black box shown panels b-d of Figure B.3.171

Chapter 1

Introduction

Marine stratocumulus cloud-topped boundary layers in the eastern subtropical oceans form as a result of local coupling between the ocean and large scale subsidence from the descending branch of the Hadley cell. The high albedo and large spatial extent of stratocumulus clouds make them a critical component of Earth's net radiative balance. The presence or absence of clouds is not the direct result of one process or parameter, but rather is an outcome determined by complex interactions among interwoven processes acting on a wide range of spatial and temporal scales. The processes span from cloud-aerosol-precipitation interactions acting on scales less than a meter to global circulations whose spatial extent is thousands of kilometers. Stratocumulus clouds vary on temporal scales ranging from minutes to decades. The sheer number of dynamic interactions within the coupled system make stratocumulus clouds both a challenging and an intellectually stimulating topic to explore. The coupled system also presents a challenge for modelers seeking to include stratocumulus clouds in their simulations of the total climate system.

This dissertation consists of two separate analyses, each of which addresses an individual component of the cloud-topped boundary layer system. The two parts use different data sets to approach the problem. The primary goal of both chapters is the same – to attempt to better understand the governing processes that drive variability in the stratocumulus-topped boundary layer system. A secondary objective is to provide a set of targets, distributions of physical parameters of the system, which can be used by model and parameterization developers to evaluate and eventually improve the modeling of these climatologically important clouds. Each chapter is presented as a discrete unit that could stand alone as a journal article. This means that some components, notably the introductory materials, overlap between chapters. I also use the plural 'we' to acknowledge the contributions of the coauthors on the eventual papers.

Chapter 2 presents a detailed analysis of the diurnal cycle of marine stratocumulus clouds and precipitation. This material is from the final accepted version of a peer-reviewed journal article that is currently in press (Burleyson et al. 2013). In Chapter 2, I use ship-based data from the VOCALS-REx field campaign to attempt to answer a series of questions:

- 1) To what extent do key components of the system vary across the diurnal cycle?
- 2) What is the driving mechanism that forces diurnal variability?
- 3) In the cases where there is a diurnal cycle, how does the magnitude of the diurnal variation compare to the well-documented longitudinal gradients?

Chapter 3 seeks to isolate specific processes that exert the largest impact on variability of stratocumulus cloud fraction on a range of time scales. This chapter is built off of a new and unique cloud identification methodology based on high resolution (both in space and time) infrared brightness temperature data from geostationary satellites. This novel dataset allows us to look at cloud fraction variability on sub-diurnal time scales.

Chapter 4 summarizes the findings of each piece of analysis and outlines a way forward to expand and clarify new results. I include in Appendix B an additional analysis that I have completed during my doctoral work that focuses on precipitation variability in the Lake Victoria region of eastern Africa. While not directly related to my primary topic of study, the Lake Victoria analysis does give some insight into other projects I have been involved with. Appendix B is also in the form of a draft journal article.

Chapter 2

The Diurnal Cycle of Marine Stratocumulus Clouds and Precipitation

2.1 Introduction

Large areas of marine stratocumulus clouds form over the subtropical open oceans to the west of continents and underneath the strong capping inversion associated with the descending branch of the Hadley cell. Marine stratocumulus clouds are widespread, low, optically thick, and persist for long periods of time. Their high albedo allows stratocumulus clouds to reflect large amounts of incoming shortwave radiation. The limited vertical extent of stratocumulus (typical cloud tops are 1-2 km high) means they emit nearly the same amount of longwave radiation as the underlying ocean. These combined radiative properties have a net cooling effect on the earth's climate (Hartmann et al. 1992). In order to capture the effects of stratocumulus on large-scale atmospheric circulations, climate models must correctly reproduce the temporal and spatial variability of these clouds as well as their thickness and height. The radiative properties of stratocumulus remain poorly captured in general circulation models (GCMs), constituting a major source of uncertainty in climate simulations (Bony et al. 2006). Cloud-topped boundary layers are notoriously difficult to simulate; the particular deficiencies of various global models have been assessed in numerous studies (e.g. Weare 1996; Bony and Dufresne 2005; Wyant et al. 2006). GCMs often fail to capture the diurnal variation of important processes in the cloud-topped boundary layer system, such as the reduction of cloud fraction and likelihood of decoupling during the afternoon (Abel et al. 2010, Medeiros et al. 2012).

Marine stratocumulus clouds exhibit a particularly strong diurnal cycle because many of the processes that drive turbulent mixing in cloud-topped boundary layers are radiatively forced (Nicholls 1984; Betts 1990; Rogers et al. 1995). In contrast to continental boundary

layers, which are usually mixed from the bottom up, marine stratocumulus cloud-topped boundary layers are primarily turbulently mixed from the top down. Buoyancy flux in stratocumulus-topped boundary layers, the maximum of which occurs near cloud top, is the primary source of turbulent kinetic energy (Moeng et al. 1992; Bretherton and Wyant 1997). Parcels near the cloud top become negatively buoyant through a combination of evaporative cooling from the entrainment mixing of warm dry air from the free troposphere and radiative cooling (James 1959). The generation of turbulent kinetic energy by sinking negatively buoyant parcels serves to mix the boundary layer. During the day, some of the cloud-top cooling can be offset by shortwave heating, and the strength of the turbulent connection with the moist subcloud layer diminishes (Nicholls 1984; Turton and Nicholls 1987; Duynkerke 1989).

Marine stratocumulus have annual climatological cloud fractions near 70% in the southeast Pacific (SEP) (Klein and Hartmann, 1993), and are able to persist for many hours to days. Clouds persist through most afternoons when there is typically net radiative warming. Turbulence connects (or couples) the cloud with the ocean surface and supplies the cloud with moisture. Reduced turbulent mixing can cause the separation of the boundary layer into distinct cloud and subcloud layers, a state called “decoupled” (Turton and Nicholls 1987). In reality, the strength and depth of turbulent mixing in the stratocumulus-topped boundary layer exists in a continuum between fully coupled and fully decoupled. We will refer to the place in the continuum as being more or less strongly coupled. Reduced vertical moisture flux into the cloud when the boundary layer is less strongly coupled means there is less moisture to offset entrainment or sensible heating, and the cloud can evaporate. If weaker coupling persists, the cloud fraction and albedo will decrease as the cloud thins and eventually breaks apart (Betts 1990). Duynkerke (1989) showed that the decrease in the degree of coupling between the cloud layer from the surface layer can occur shortly after sunrise and persist until sunset, implying that it takes very little solar heating to reduce the strength of turbulent coupling.

In addition to cloud fraction and the degree of boundary layer coupling, cloud thickness, precipitation, and liquid water path (LWP) also have a regular diurnal cycle. Higher LWP reduces the incoming solar radiation that reaches the surface by modifying the optical depth of the cloud, with thicker clouds absorbing and scattering more incoming radiation. Cloud thickness affects the generation of precipitation (Comstock et al. 2004), which in turn removes liquid water from the cloud and can lead to mesoscale circulations that contribute to the break up the cloud. We will show cycles in precipitation and cloud thickness and how they are related to the diurnal cycle of boundary layer decoupling.

In this study we document the diurnal variation of marine stratocumulus in the SEP with the goal of better understanding the dominant processes that control these climatologically important clouds. The Variability of the American Monsoon Systems' (VAMOS) Ocean-Cloud-Atmosphere-Land Study Regional Experiment (VOCALS-REx) dataset allows us to examine the diurnal variation of multiple parameters of the stratocumulus-topped boundary layer system simultaneously. To facilitate our understanding of the complex and interrelated processes of the stratocumulus cloud system in the SEP, we examine in concert a multitude of simultaneously measured data from VOCALS-REx. The VOCALS-REx data sets used here are from ship-based instruments (de Szoeke et al. 2010a, 2012), each sampling for several weeks across a large cross section of the SEP (Wood et al. 2011). Aircraft studies of the diurnal cycle are limited by the relatively short and temporally sparse nature of the aircraft data. In comparison, the VOCALS-REx ship-based data set provides a robust diurnal signal. We build on previous work that shows the diurnal cycle in turbulent mixing dominates variability in several of the climatologically important properties of stratocumulus clouds. Our analysis of the diurnal variability of precipitation identifies a new component of the diurnal cycle, a decrease in precipitation in the western portion of the VOCALS-REx domain before the sun comes up, that had previously gone undetected. The observed diurnal cycle can serve as a potential target for future modeling studies attempting to replicate variations in a stratocumulus-topped boundary layer system.

2.2 Data and Methods

VOCALS-REx data presented here were collected aboard the National Oceanic and Atmospheric Administration (NOAA) research ship Ronald H. Brown (RHB). The RHB traversed the 20°S parallel underneath the SEP cloud deck from Arica, Chile (70°W) to 85°W three separate times during the course of the experiment. Specifically the two research cruise legs from the ship were from 25 October to 2 November 2008 and 10 November to 2 December 2008. Along the way, the ship spent several days at each of two ocean buoys moored on the 20°S parallel near 75°W and 85°W. The distribution of sampling by the scanning C-band radar (Fig. 2.1) is representative of sampling by all of the other instruments aboard the RHB. The RHB samples are temporally continuous and provide a robust picture of the diurnal cycle of the stratocumulus cloud deck. Ship-based data were gathered evenly across the diurnal cycle (Fig. 2.1). For this reason we limit our analysis to data obtained aboard the RHB.

The RHB served as an instrument platform for numerous observations of cloud structure, precipitation, and thermodynamics within the marine boundary layer (de Szoeki et al. 2010a). Of primary importance to this study are observations collected utilizing the ship's vertically-pointing W-band cloud radar (Moran et al. 2011; de Szoeki et al. 2010a, 2012), vertically-pointing passive microwave radiometer (Zuidema et al. 2005), scanning Doppler lidar (Grund et al. 2001), scanning C-band precipitation radar (Ryan et al. 2002), laser ceilometer, surface meteorology tower, and the rawinsondes launched every four hours during the cruise. The RHB was outfitted with a scanning C-band radar to observe light precipitation forming in the shallow stratocumulus clouds. The radar has a wavelength of 5 cm, making it sensitive to moderate drizzle and rain but not the clouds themselves (Ryan et al. 2002). Details of the C-band radar scan strategy used during VOCALS-REx are given in Appendix A of Burleyson et al. (2013). The 2- μ m High Resolution Doppler Lidar (HRDL) measured backscatter intensity and radial wind velocity with 30 m resolution within 6 km of

the ship. The scan strategy for the lidar was a repeating 20 minute sequence that included plan position indicator (PPI), range-height indicator (RHI), and vertically-pointing modes.

One prominent feature of the SEP stratocumulus deck is the gradual increase in boundary layer depth westward from the South American coast in conjunction with warmer underlying sea-surface temperatures (Wood and Bretherton 2004; Leon et al. 2008; Zuidema et al. 2009; de Szoeki et al. 2012; etc.). In addition, atmospheric aerosol concentrations have also been observed to decrease westward, resulting in a longitudinal gradient in cloud droplet number concentrations (Bennartz 2007; Wood et al. 2008; George and Wood 2010; Bretherton et al. 2010). There is synoptic and interannual variability in the longitudinal gradients of these properties, yet the gradients were observed most times during VOCALS-REx. Boundary layer depth and cloud droplet number concentration have both been shown to interact with the cloud-aerosol-precipitation processes in the stratocumulus clouds over the SEP, resulting in longitudinal gradients in drizzle and cloud fraction (Wood and Bretherton 2004; Leon et al. 2008; Mechum et al. 2012). The time series of data from the ship (for example Fig. 2 from de Szoeki et al. 2010a) does show diurnal, longitudinal, and synoptic variability, with the dominant signals in the time series being the diurnal and longitudinal patterns. To account for longitudinal variability in our analysis of the diurnal cycle, we have subdivided our results into two regions, east and west of 80°W, when sample sizes allow it. Subdividing the data in this way isolates the effects of the longitudinal gradients in cloud properties from the diurnal cycle. Throughout the paper, results shown in blue represent data collected in the region east of 80°W (i.e. closer to the coast, higher aerosol concentration, shallower boundary layer) and results shown in pink represent data west of 80°W (i.e. farther from the coast, lower aerosol concentration, deeper boundary layer).

The relatively slow motion of the ship compared to the evolution time of the atmosphere means that the RHB was subject to synoptic influences in the region (see Toniazzi et al. [2011] for a discussion of the synoptic meteorology conditions in the southeast Pacific during VOCALS-REx). Synoptic variability in key variables is smaller

along and north of 20°S compared to regions closer to the extratropical cyclone track further south. For example, the variability of inversion height associated with synoptic influences is roughly +/- 0.2 to 0.4 km along 20°S compared to +/- 0.8 to 1.0 km along 30°S (Toniazzi et al. 2011; their Fig. 21a). There is no reason to believe that the synoptic forcing will systematically occur at any one time during the diurnal cycle. Rather, synoptic influences will show up as small random perturbations on top of the mean diurnal cycle that comes from 31 days of data.

We examine both the mean and quartiles of several variables to capture their underlying distribution and avoid possible misinterpretation that may arise from taking averages of a non-Gaussian distribution (Taleb 2007). The hourly mean values in our analysis will be indicated by a heavy bold line, overlaid on a shaded region that indicates the area between the 25th and 75th percentiles of the hourly distributions. While most of the distributions appear to be quasi-Gaussian, with the mean lying approximately in the middle of the interquartile range, precipitation intensity and drizzle cell size are lognormal. All times given have been converted to local solar time using the longitude at which the measurement was made.

2.3 Results

2.3.1 Boundary Layer Mixing

We begin an analysis of the diurnal cycle by examining factors controlling the diurnal variation of boundary layer mixing. Our analysis focuses on the diurnal cycle of boundary layer mixing and stratification and complements recent studies of the diurnal cycle of stratocumulus in the southeast Pacific (de Szoeke et al. 2012; Painemal et al. 2013). Fig. 2.2 shows a time-height representation of the vertical profile of mean vertical velocity variance measured from the NOAA High-Resolution Doppler Lidar. Data were collected in 10-minute windows when the lidar was in vertically-pointing mode. The mean profiles were normalized to the base of the cloud such that a height of 1.0 represents cloud base while 0.2 represents a

height that is 20% of the measured cloud base height. The data were quality controlled using the signal-to-noise ratio (SNR) to remove weak signals (SNR < 0 dB) and the downdrafts associated with precipitation (SNR > 15 dB). Higher variance of the vertical velocities indicates stronger turbulent mixing.

Consistent with a mixing profile that is driven by top-down mixing (James 1959), the strongest variance values are located at the base of the cloud and top of the subcloud layer and variance decreases downward toward the surface. The diurnal cycle of boundary layer mixing is evident both east and west of 80°W. Overnight mean profiles have higher vertical velocity variance compared the midday values. Shortly after sunrise (~6:00 am) the variance values decrease sharply throughout the depth of the subcloud layer as solar heating acts to limit the generation of negatively buoyant parcels at cloud top. Vertical velocity variance remains low throughout the day and begins to slowly increase again as the sun goes down (~6:00 pm). Overall, turbulent mixing is somewhat stronger and deeper in the east (Fig. 2.2a) compared to the west (Fig. 2.2b). This is consistent with a boundary layer that is shallower and more strongly coupled closer to the coast compared to further away. We believe the anomalous values of vertical velocity variance between 2:00 and 3:00 am west of 80°W are likely an artifact due to a combination of the large variability of conditions at that time and small sample size of the vertically-pointing lidar data.

One interesting feature of this analysis is the rate at which turbulence decreases after sunrise compared to the rate at which it increases after sunset. There is a distinct decrease in the mean vertical velocity variance profiles after 8:00 am in both the eastern and western portions of the VOCALS-REx domain. This indicates a sudden reduction in the overall strength of the turbulent motions. The pace at which turbulence begins to strengthen after sunset is much slower. Strong turbulent overturning is not present until roughly 7:00-8:00 pm in the east and after 9:00 pm in the west. Because the generation of turbulence via longwave cooling is amplified by the presence of cloud, this delay in the strengthening of turbulent mixing could be due to the time after sunset that it takes for the cloud fraction to increase to

its overnight values. Previous work has shown that it takes several hours after sunset for cloud fraction to recover to its overnight value (de Szoeke et al. 2012; their Fig. 8a).

We used the four-hourly VOCALS-REx sounding data to construct mean profiles of potential temperature, water vapor mixing ratio, and horizontal wind speeds. In this case we did not divide the data into east and west regions because of the smaller sample size of the 216 radiosonde launches. To account for the east-west gradient in boundary layer depth, we normalize the height coordinate to the base and top of the cloud. The subcloud layer in each sounding is divided into ten evenly spaced bins that span the height between 50 m above the surface and the measured base of the cloud, and within the cloud five bins are evenly distributed between the measured cloud base and cloud top. Fig. 2.3a shows the diurnal cycle of average potential temperature between 50 m above the surface and the top of the cloud. Where potential temperature is constant with height, the temperature gradient is neutrally stable to adiabatic motions of unsaturated air parcels.

One salient feature of Fig. 2.3a is the nearly isentropic layer (~ 290 K) formed shortly after sunset ($\sim 6:00$ pm) from the surface up halfway to cloud base. Between midnight and 4:00 am, this nearly isentropic layer extends further upward to encompass the full vertical extent of the subcloud layer. This indicates strong upward and downward mixing. Negatively buoyant cloud parcels may descend toward the surface without encountering a stable layer. Likewise, positively buoyant subcloud parcels would encounter no strong stability boundaries during their ascent to cloud base. The projection of this vertical overturning onto the horizontal winds may also be the cause of the high wind speeds in the subcloud layer overnight (Fig. 2.3c). The sun rises between the 4:00 am and 8:00 am sounding and there is a 1 K cooling throughout most of the subcloud layer, with the strongest cooling occurring in the lowest third of the subcloud layer. Cooling of the subcloud layer in the early morning hours is likely a sign of radiatively cooled parcels from cloud top being mixed downward into the subcloud layer. Evaporative cooling from drizzle could also be contributing to the observed cooling. More importantly though, during this period around sunrise the vertical

potential temperature gradient also begins to increase, indicating a stable layer between cloud base and the surface. Between 8:00 am and noon a layer just below cloud base becomes more strongly stable, with a vertical potential temperature gradient greater than 1 K between cloud base and the surface. Horizontal wind speeds on top of the stably stratified layer decrease while remaining fairly steady within the mixed layer extending upwards from the surface. The increased stratification of potential temperature during the morning and afternoon would inhibit the availability of surface moisture to the cloud.

To investigate the effect of increased stability on the moisture, we calculated the water vapor mixing ratios (g kg^{-1}) using temperature and relative humidity data from the soundings. We use water vapor mixing ratio as a conserved tracer to indicate the vertical extent of moisture in the boundary layer. Surface evaporation rates are roughly constant across the diurnal cycle (de Szoeké et al. 2010a), so the diurnal variation in moisture content near the surface is a function of the rate at which moisture is transported away from the surface. The average water vapor mixing ratio profiles shown in Fig. 2.3b illustrate the diurnal variation of the degree of coupling of the boundary layer. Drying in the layer immediately beneath cloud base begins after sunrise and slowly extends downward toward the surface. During the day a clearly defined moist surface layer forms when the cloud deck is generally less well coupled with the surface. Moisture in the lower portion of the subcloud layer increases in time after noon. The interface between the dry subcloud layer and surface-based moist layer creates a strong vertical gradient in water vapor mixing ratio. Water vapor near the surface reaches its diurnal maximum ($\sim 9 \text{ g kg}^{-1}$) by sunset. Vertical moisture gradients decrease after sunset as moisture is again mixed upward away from the surface resulting in a more evenly distributed moisture profile. This process allows the cloud to tap into the reservoir of surface moisture resulting in a deeper stratocumulus cloud deck and higher cloud fractions overnight.

The mean sounding data indicate a fairly regular daily transition in the degree of coupling in the stratocumulus-topped boundary layer system. We can visualize one example

of this transition using lidar data collected on 2-Nov 2008 (Fig. 2.4a). The strongest scattering of the lidar beam occurs within the cloud deck and during drizzle where signal strength values upwards of 20 dB occur. Aerosols have weaker backscatter than cloud and are present in varying concentrations from cloud base to the ocean surface. Aerosol backscatter intensity is a function of number concentration and size of the scatterers. Higher ambient relative humidity also increases the lidar backscatter by swelling hygroscopic particles (Tang, 1996). From 4:00 am through 11:00 am, aerosols in the subcloud layer are vertically well-mixed and their corresponding backscatter intensity is roughly constant from the ocean surface to the cloud base (Fig. 2.4a and 2.4b). Shortly after local noon a cleaner (lower aerosol concentration) or drier (lower relative humidity) layer with lower backscatter begins to appear below cloud base and grows downward to eventually encompass almost half of the subcloud layer by sunset. The gradient in aerosol backscatter between the dirty and/or moist near-surface layer and the cleaner and/or drier air above represents the top of the well-mixed surface layer during the period when there is a decoupled boundary layer (Fig. 2.4c).

2.3.2 Surface Variables

Hourly 10 m surface air temperature values are shown in Fig. 2.5a. As expected in a cloud-topped marine boundary layer, the diurnal variation in air temperature is quite small (less than 1°C both east and west of 80°W). Daily minimum values occur near sunrise, followed by a gradual increase throughout the morning that peaks around local noon. The air temperatures after noon remain fairly constant for a period of 10-12 hours and then gradually decrease in the overnight hours. The high cloud fraction of the stratocumulus deck and large heat capacity of the underlying ocean play a significant role in the moderation of the daily temperature cycle. A minimal temperature difference between the ocean and the lower atmosphere (typically 1-2°C; Painemal et al. 2010) limits the exchange of sensible heat from the ocean to the atmosphere ($< 6 \text{ W m}^{-2}$; de Szoeki et al. 2010a). The mean air and sea surface temperatures in the western portion of the SEP stratocumulus domain are about 1°C warmer than the eastern portion (Bretherton et al. 2004).

Diurnal variation in near-surface dew point temperature is shown in Fig. 2.5b. Dew points have a diurnal minimum near sunrise, increase roughly linearly until just before sunset, and then gradually drop. The amplitude of the diurnal variation is close to 1.5°C in both the east and west, and its sinusoidal pattern follows that of temperature from midnight to noon, when the boundary layer is more coupled. When the boundary layer becomes less coupled in the afternoon, the dew point temperature rises because of the increase in moisture content of the near surface boundary layer. Surface moisture accumulates during the day when the coupling with the cloud deck is weakest and decreases overnight due to stronger vertical moisture fluxes away from the surface.

Near surface wind speed and wind direction distributions across the diurnal cycle are shown in Fig. 2.5c and 2.5d. There is only a weak cycle near surface wind speeds. The magnitude of the wind speed longitudinal gradient is larger than the diurnal variability. There is a 2 m s^{-1} difference in hourly mean wind speed between the east and west compared to a 1.2 m s^{-1} between maximum and minimum hourly mean wind speed in both the east and west. Mean wind direction in the western portion of the VOCALS-REx domain shows little diurnal variability while in the eastern portion there is a persistent backing of the near surface winds from SE to ESE during the day. This change in wind direction is consistent with the documented coastal meteorology patterns along the western coast of South America (Garreaud and Munoz 2004).

The diurnal distributions of downwelling shortwave and longwave radiative flux, measured at 10-minute intervals, are shown in Fig. 2.5e and 2.5f respectively. The underlying distribution of shortwave radiation has a positive definite cosine shape with a daily maximum mean value near local noon in both the west ($\sim 800\text{ W m}^{-2}$) and east ($\sim 700\text{ W m}^{-2}$). Previous studies have shown that the western cloud field tends to break up earlier and more often than in the eastern region closer to South America (Bretherton et al. 2010). The larger interquartile range of shortwave radiation in the western portion of the domain indicates a less consistent cloud field. Not surprisingly, downwelling longwave radiation is strongest and most

consistent ($\sim 380 \text{ W m}^{-2}$) at night, when the cloud is thickest and most spatially coherent. The afternoon minimum mean value and the larger interquartile range in both regions ($\sim 360 \text{ W m}^{-2}$) are related to cloud break up. While the extrema of the mean diurnal cycle in downwelling longwave radiation are similar throughout the VOCALS-REx domain, the range in the distribution increases slightly earlier and decreases slightly later west of 80°W . This is consistent with a cloud deck that breaks up slightly earlier and reforms slightly later in the west compared to the east. While the mean values of the ship's longwave radiative flux measurements are consistent with those from the C-130, the limited diurnal sampling of the aircraft data misses some of the subtlety of the diurnal cycle such as the increased variability in the western half of the domain (Bretherton et al. 2010).

Sulfate is the dominant submicron aerosol species in the VOCALS-REx region (Jaeglé et al. 2011; Shank et al. 2012), and the diurnal variation in its gas-phase precursors peaks overnight west of 78°W (Yang et al. 2011). Near-surface aerosol concentration observations were made at the bow of the ship ($\sim 15 \text{ m}$ above sea level) during VOCALS-REx. The near-surface concentrations of Aitken and accumulation mode aerosols, roughly less than and greater than $0.1 \mu\text{m}$ in diameter respectively, were measured at 10-minute intervals. There is large day-to-day and week-to-week variability in the measured near-surface aerosol concentrations. The hourly means and interquartile ranges of these concentrations are shown in Fig. 2.6a and 2.6b. Aerosol concentration varies for some individual days and is relatively constant for others. Consistent with previous work, we found no robust or systematic diurnal cycle in aerosol concentrations (Tomlinson et al. 2007). There was a longitudinal gradient in aerosol concentrations with higher concentrations in the east (e.g. Allen et al. 2011, de Szoeken et al. 2012). The mean near-surface accumulation mode aerosol concentration east of 80°W was $\sim 50 \text{ cm}^{-3}$ higher than in the west. In the Aitken mode, a weak east-to-west gradient of $\sim 50\text{-}100 \text{ cm}^{-3}$ occurs only during the afternoon and early evening. Whether the afternoon and early evening variation reflects changes in formation or scavenging is unclear.

2.3.3 Cloud Measurements

As with other variables, variations in the base and top of the cloud are affected by the diurnal cycle. During VOCALS-REx several instruments were deployed to measure changes of the height and depth properties of the cloud (de Szoeke et al. 2012). The east-west division allows the diurnal variability to be compared with longitudinal variability. Diurnal variations in the base of the cloud are shown in Fig. 2.7a. Shortly after sunrise the mean altitude of cloud base begins to increase, rising approximately 200 m by noon in both the eastern and western portions of the domain. After noon, the base of the cloud lowers until it reaches its overnight value by sunset, at which point the cloud base remains fairly steady throughout the night. One significant feature of the measured cloud base heights is the distinct east-west difference. Cloud bases in the western portion of the domain are on average 200 m higher than those closer to the coast.

The top of the stratocumulus cloud deck, Fig. 2.7b, coincides with the height of the subsidence inversion. Inversion base height was measured every four hours from the soundings launched from the ship. In this study, the top of the cloud is estimated from the inversion height from soundings, and interpolated from the soundings to every 10 minutes. This method of determining the stratocumulus cloud top height is consistent during both legs of VOCALS-REx, and agrees well with the measurement from the vertically-pointing W-band radar when it was available during the second leg. The strong east-west gradient of boundary layer depths manifests itself in higher cloud tops westward. Further west from the coast, the height of the inversion is nearly 250 m higher than in the eastern portion of the VOCALS-REx domain. Cloud top heights also show a significant diurnal variation. Discounting horizontal advection in the boundary layer, the height of the subsidence inversion will increase due to entrainment into the boundary layer of warm dry air from above the inversion and decrease due to subsidence of air above the inversion. For 10-hours from midnight through 10:00 am these two counteracting tendencies are balanced and the cloud top height is fairly constant east of 80°W. Overnight the cloud top height increases to its maximum altitude around midnight in the east and closer to 3:00 am in the west. As the

cloud begins to break up after sunrise the rate of subsidence outpaces entrainment deepening, causing the boundary layer to become shallower (Lewellen and Lewellen 1998). By 6:00 pm, the mean cloud top west of 80°W has decreased nearly 150 m from its overnight value. In the east, the decrease in cloud top height is between 75 and 100 m. A shallower boundary layer persists until the cloud begins to recover near sunset and entrainment warming and deepening is able to overcome subsidence.

Overnight the cloud depth is nearly constant as a result of stationary cloud base and top heights. Mean cloud depths are close to 300 m, with only slightly deeper clouds in the western portion of the domain compared to the east. After sunrise, increasing cloud base heights combine with a steady cloud top to decrease the cloud depth by a factor of two by early afternoon. The mean rate of thinning ($\sim 25 \text{ m hr}^{-1}$) is constant throughout the morning. The cloud gradually thickens after 3:00 pm. The 9 hours it takes for the cloud to thicken (at $\sim 15 \text{ m hr}^{-1}$) to its nighttime value is somewhat slower than the time it takes to thin. These rates are consistent with a boundary layer that takes longer to recouple than decouple (Fig. 2.2).

As southeast Pacific stratocumulus are largely adiabatic (Zuidema et al. 2012), the diurnal cycle of liquid water path (Fig. 2.8a and 2.8b) very closely resembles the diurnal cycle in cloud depth. Liquid water path values are at times positively skewed such that the mean is closer to the 75th percentile than the 25th percentile. Further discussion of the liquid water path characteristics for the region including diurnal and longitudinal gradients in adiabaticity is given in de Szoeke et al. (2012) and Zuidema et al. (2012).

2.3.4 Precipitation

Drizzle frequently forms in shallow stratocumulus clouds as a result of collision and coalescence of cloud droplets. When present, drizzle often organizes into discrete cellular structures, with cloud tops over drizzling cells being slightly higher than the areal averaged cloud top height (e.g. vanZanten and Stevens, 2005; Comstock et al. 2005, 2007). Drizzle

formation, fallout, and cessation is dependent on many factors such as cloud base and top height, cloud depth and liquid water content, cloud-aerosol interaction, and boundary layer turbulent moisture transport (e.g. Comstock et al. 2004, 2005; Zuidema et al. 2009). To determine drizzle cell frequency and extent, we follow Comstock et al. (2007) and use an algorithm designed to look for contiguous regions of radar reflectivity greater than 5 dBZ. This algorithm separates individual drizzle cells from the background cloud. Relaxing the minimum reflectivity threshold to 0 dBZ, a commonly accepted threshold for drizzle that is likely reaching the surface (Comstock et al. 2004), slightly modifies the drizzle cell size distributions shown in Fig. 2.10, but does not otherwise affect our results. We used a minimum cell area threshold of just over 0.5 km^2 , which corresponds to eight contiguous radar pixels. The diurnal mean values for the number of drizzle cells observed in each radar scan as well as the cumulative drizzle area for regions both east and west of 80°W are shown in Fig. 2.9a and 2.9b.

The diurnal maximum of cell counts and total precipitation area (Fig. 2.9a and 2.9b) is between midnight and sunrise when the cloud is thickest. During the night, the C-band radar observed over three times the number of drizzle cells in the region west of 80°W than in the region east of 80°W . The enhanced drizzle frequency in the west is consistent with the deeper boundary layer, slightly higher LWP, and fewer cloud condensation nuclei in the environment west of 80°W . Fig. 2.9c shows the diurnal mean and distribution of areal average rain rates for both regions of the VOCALS-REx domain. The areal-average rain rates east and west of 80°W are broadly consistent with the gradients documented in the C-130 and CloudSat data (Bretherton et al. 2010). The cloud base rain rate for drizzling stratocumulus clouds is proportional to the cloud depth and LWP (e.g. Comstock et al. 2004). The hourly conditional rain rate (Fig. 2.9d) is the average of raining pixels (those above a range-dependent sensitivity threshold) for all hours in which the precipitating area exceeded 100 km^2 (see Appendix A of Burleyson et al. 2013 for details). In the region west of 80°W , the mean conditional rain rate was 6.5 mm day^{-1} compared to 3.5 mm day^{-1} east of 80°W . The conditional rain rates for the east and west regions each show very little diurnal

variation. The diurnal variation of the areal average rain rates for a given region is primarily related to variations in the drizzling area rather than changes in the intensity of drizzle.

The size distribution of all individual drizzle cell areas observed by the C-band radar during VOCALS-REx (Fig. 2.10) is highly skewed, and drizzle cells with areas $< 1 \text{ km}^2$ outnumber cells of larger sizes throughout the diurnal cycle. The increase in the overall number of drizzle cells overnight (Fig. 2.9a) is related both to a large increase in the number of smaller drizzle cells, and to more larger cells (broadening the cell area distribution). West of 80°W the number of drizzle cells smaller than 1 km^2 nearly quadruples from 6:00 pm to 3:00 am.

The extensive VOCALS-REx radar data set provides a clear view of how drizzle varies diurnally, but also brings to light an important contrast in the timing of precipitation between the eastern and western portions of the VOCALS-REx domain. The timing of changes in the mean total area of precipitation east of 80°W is closely tied to sunrise and sunset. The total area of C-band observed precipitation decreases from $\sim 250 \text{ km}^2$ to $\sim 100 \text{ km}^2$, from a radar coverage area of roughly $10,000 \text{ km}^2$, between 7:00 am and 9:00 am (Fig. 2.9b). This decrease in precipitation occurs as the cloud thins and turbulent moisture transport begins to weaken after sunrise. The number of drizzle cells and the total drizzle area remain small throughout the day. Once the turbulent vertical moisture flux increases again after sunset, the precipitation area increases to its overnight value. In contrast, west of 80°W the maximum precipitation area occurs between 3:00 am and 5:00 am, and begins to decrease before the sun comes up. In the predawn hours, the solar radiation has yet to reduce turbulence generation and vertical moisture transport, so it cannot yet affect the cloud and precipitation. The reduction in the number of drizzle cells, the total drizzle area, and the areal average rain rate is out of phase with the diurnal variations in cloud thickness, liquid water path, and boundary layer turbulent mixing, indicating a different process limits drizzle in the early morning hours in the western region of the VOCALS-REx domain.

We examined several potential reasons for the decrease in precipitation between 3:00 and 5:00 am in the western portion of the domain. The cloud itself is generally persistent. Fig. 2.7 shows that the cloud base, cloud top, and cloud depth in the western portion of the domain are all roughly constant between midnight and 6 am. Liquid water path measurements (Fig. 2.8) have a higher mean ($\sim 150 \text{ g m}^{-2}$) and are more positively skewed between 3:00 am and 6:00 am compared to the window between midnight and 3:00 am. The impact of the “upsidence” wave, modeled by Garreaud and Muñoz (2004; their Fig. 5) and Rahn and Garreaud (2010; their Fig. 14), is inconclusive in the western portion of the VOCALS-REx domain in the 3-6 hours before sunrise. The free tropospheric subsidence anomaly is either neutral or slightly negative (upward). Wood et al. (2009; their Fig. 5a and 6) found that the region west of 80°W should have a diurnal minimum in subsidence and a higher mean liquid water path in the six hours before sunrise. Their work was based on European Centre for Medium-Range Weather Forecasts (ECMWF) analyses and passive microwave data. The modeling work of Wyant et al. (2010) showed LWP and cloud fraction changed little due to the upsidence wave in the SEP stratocumulus deck. If anything the higher liquid water paths associated with the upsidence wave would increase precipitation, in contrast to the observed decrease in precipitation. Therefore we believe that the upsidence wave is likely not the cause of the observed decrease in precipitation in the early morning hours over the western portion of the VOCALS-REx domain.

Another possible explanation for the early morning diminution of the number of drizzle cells and the areal average rain rate west of 80°W is that the precipitation itself causes a reduction in the vertical moisture transport by creating a stability boundary in the subcloud layer (Bretherton and Wyant 1997). A majority of the drizzle from marine stratocumulus clouds evaporates before reaching the surface and this evaporation will drive cooling in the subcloud layer (Comstock et al. 2004). Evaporative cooling of the subcloud layer can generate a stable lapse rate beneath the base of the cloud (e.g. the “drizzling” potential temperature profiles of Comstock et al. 2005). Jones et al. (2011) show that higher cloud base and LCL height differences, a symptom of less coupled boundary layers, are correlated with

times of heavier drizzle. This relationship was particularly evident in further from the coast where heavier drizzle is most prominent.

A possible example of the near cloud base precipitation-induced stabilization is shown in Fig. 2.11, where we compare two soundings launched roughly five hours apart on 23 November 2008 when the ship was near 85°W. Drizzle was in the vicinity of the ship for the entire time between the two soundings. In the 9:45 pm sounding (Fig. 2.11a), the subcloud potential temperature profile is isentropic all the way up to the base of the cloud. The subsequent sounding at 2:30 am (Fig. 2.11b), launched after persistent drizzle was in the vicinity of the ship for many hours, shows a potential temperature profile that increases upward from 0.9 km to cloud base at 1.2 km. This slight stability boundary could be enough to inhibit vertical moisture transport into the cloud and limit further precipitation.

It is our hypothesis that the total area of drizzle cells is self-limiting. Vertical mixing can be reduced by localized evaporative cooling and stabilization related to drizzle from individual small drizzle cells even if a detectable cold pool does not form. The combined effect of a high areal density of these small cells over time is to limit opportunities for new cells to form. Only a subset of drizzle cells are strong enough to produce sufficiently negatively buoyant air from evaporative cooling to yield surface cold pools and hence opportunities for surface convergence and new cell growth (vanZanten and Stevens 2005; Feingold et al. 2010; Terai 2011). We are not proposing that the entire domain would be stabilized by precipitation, which is unlikely given the areal average rain rates of 1.5 mm day⁻¹ or less. Rather, the ensemble of cell local stabilization effects near cloud base, such as illustrated by the soundings in Fig. 2.11, may yield a domain-wide phenomenon that manifests as a statistical decrease in the number of drizzle cells, the total precipitation area, and the areal average rain rates (Figs. 2.9 and 2.10).

The drizzle-induced reduction in vertical mixing mechanism builds on previous studies of drizzle processes in marine stratocumulus, namely Wang and Wang (1994),

Bretherton and Wyant (1997), and Wang and Feingold (2009). This postulation also allows that the upsidence wave may indirectly contribute to the noticeable precipitation decline by enhancing the ability of the cloud to precipitate, thus speeding up the rate of subcloud evaporative cooling and stabilization, which subsequently reduces the precipitation after 3:00 am. Untangling this sequence of events will require further study.

2.4 Conclusions

We used observations collected aboard the RHB during VOCALS-REx to investigate diurnal variations in the marine stratocumulus cloud deck over the SEP. We use coincident observations of boundary layer thermodynamics, cloud properties, and drizzle to identify processes that determine the state of the stratocumulus-topped boundary layer. The high temporal and spatial continuity as well as the large sample sizes provided by the RHB data allow us to resolve the diurnal transition in the degree of coupling of the stratocumulus-topped boundary layer. A conceptual schematic for the diurnal variation of marine stratocumulus clouds, surface mixed layer depth, drizzle, and boundary layer mixing in the SEP is shown in Fig. 2.12. This schematic complements other conceptual models (e.g. Fig. 15 from Wood 2012; Fig 17 from de Szoek et al. 2012) and is meant to capture the most likely state of the boundary layer system over an ensemble of days.

To account for the east-west gradient in sea-surface temperature, boundary layer depth, aerosol concentrations, and cloud liquid water path, we divided our results into regions east and west of 80°W. While there is some synoptic and year-to-year variation, in general the boundary layer in the western portion of the VOCALS-REx domain is typically warmer and deeper with fewer aerosols than the region closer to the South American coast (de Szoek et al. 2012). The net result of these features is a cloud deck with higher bases and tops in the west, but with a cloud thickness only slightly deeper in the west compared to the eastern portion of the domain (Fig. 2.7b and de Szoek et al. 2012; their Fig. 5a). The observed difference between cloud base and LCL heights, a proxy for the degree of turbulent

mixing, was larger in the west compared to the east (de Szoeke et al. 2012). The weaker connection between the moist surface layer and the cloud deck, particularly during the daytime hours, resulted in thinner clouds, a more broken cloud field, and an increase in the mean and variability of shortwave radiation reaching the surface. Total drizzle area and conditional rain rates were both higher in the western region.

Our study is consistent with work that shows the diurnal variation in marine stratocumulus clouds was largely driven by variations in subcloud turbulent moisture transport, which is strongly conditioned on vertical radiative flux divergence at cloud top (e.g. Nicholls 1984; Turton and Nicholls 1987). Vertical profiles of vertical velocity variance and potential temperature and moisture show that the subcloud boundary layer is well-mixed at night and that the strength of turbulent mixing decreases strongly after sunrise. There is a cooling in subcloud potential temperatures after sunrise and vertical gradients in the subcloud potential temperature profiles increase, indicating an emerging stratification in the subcloud layer. This deep cooling observed in the subcloud layer is consistent with a recent modeling study over the VOCALS-REx domain (Tonizzzo et al. 2012), but occurs somewhat later than the cooling generated in earlier simulations (e.g. Garreaud and Muñoz, 2004; their Fig. 3e). In the late afternoon, when the boundary layer is most stably stratified, the potential temperature is on average 1 K warmer at cloud base than at the ocean surface.

Vertical profiles of water vapor mixing ratio show that these stable layers are very effective at trapping moisture near the surface (Fig. 2.3). During the day, the cloud is subject to solar heating, evaporation, and drying via entrainment of free tropospheric air with little access to the surface moisture source. The ship-based data show significant cloud thinning as well as a marked reduction in precipitation during the late morning and into the afternoon. On average, a more decoupled state persists until after sunset, when net cloud top radiative cooling creates negative buoyancy. Overnight, the descent of the negatively buoyant plumes is a source of turbulent kinetic energy and results in higher vertical velocity variance. The turbulence mixes all the way through the subcloud boundary layer and allows the cloud to tap

the reservoir of moisture at the surface, resulting in a more evenly distributed water-vapor profile.

A new and interesting result came from the observations from the scanning C-band radar aboard the RHB which showed that drizzle peaked overnight in the west and around sunrise in the east. Drizzle was reduced but still present throughout the day. The distribution of drizzle cell areas shows that drizzle is most likely to be organized into small discrete cells, with the most frequent drizzle cell area being less than 1 km². In the western portion of the VOCALS-REx domain, where areal averaged rain rates are higher, the number of drizzle cells and total drizzle area peak 2-3 hours before sunrise, coincident with the diurnal peak in cloud top height in the west. This observation implies that vertical mixing in the boundary layer may be reduced even before shortwave heating stabilizes the system. A possible mechanism to account for the reduction of precipitation after 3:00 am is that the higher peak areal density of drizzle cells in the west creates a large number of localized areas of subcloud evaporation which together are sufficient to reduce the vertical moisture flux in the early morning hours, making drizzle a self-limiting process. In the future, we hope to use HRDL data collected aboard the RHB to track the diurnal evolution of the surface mixed layer and look for gradients in backscatter that could be indicative of stable subcloud layers associated with heavy drizzle. The timing and rate of drizzle-induced stabilization of the boundary layer has important implications for the simulation of stratocumulus. For example, Boutle and Abel (2012) showed that the unrealistic moistening and cooling of the subcloud layer due to excessive drizzle production in the UK Met Office model was responsible for persistent decoupled bias overnight.

With the exception of near-surface aerosol concentrations, near-surface wind speeds, and conditional rain rates, every variable examined in this study displayed a strong and persistent diurnal cycle. The magnitude of these daily variations is at least as large as the well documented east-west gradient in stratocumulus properties. Diurnal variation in most parameters of this complex system can be directly linked to the presence or absence of deep

boundary layer turbulent mixing. The observations collected aboard the RHB generally agree with data collected from other observational platforms during VOCALS-REx. Data from the ship provide a valuable tool for validating future modeling efforts of the diurnal cycle. These observations of the diurnal cycle can be used to test whether parameterizations of mixing and clouds are capable of simulating decoupled boundary layers.

2.5 Chapter 2 Figures

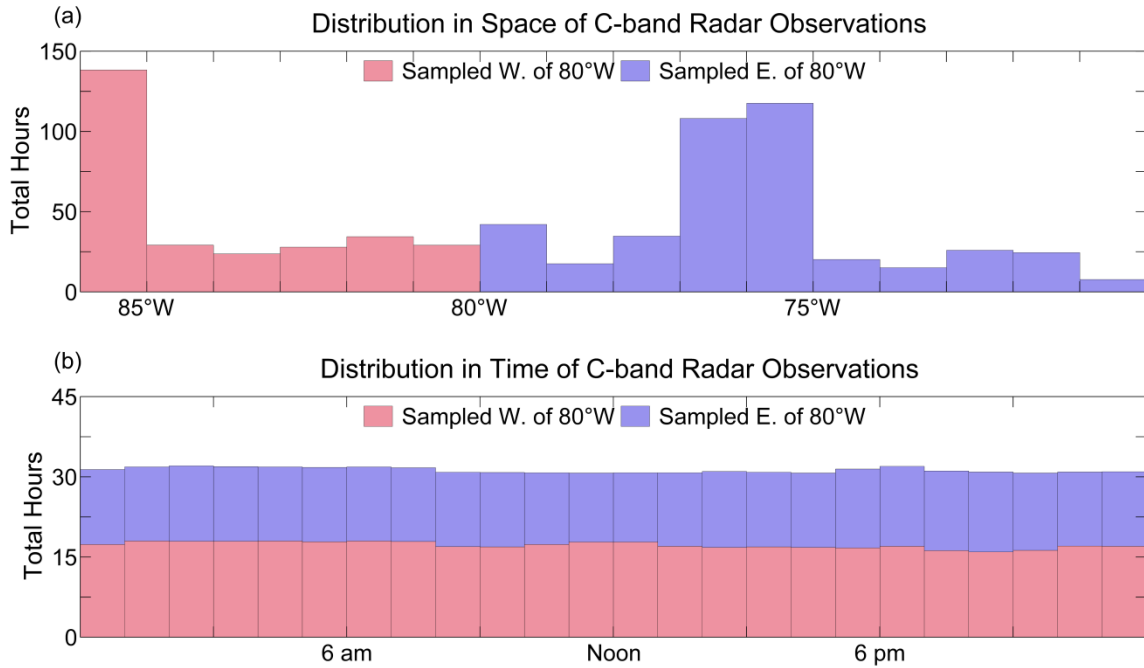


Figure 2.1. Distribution of sampling in space (a) and time (b) of hours of C-band radar data collected aboard the *RHB*. Data collected west of 80°W is displayed in pink whereas data collected east of 80°W is shown in blue.

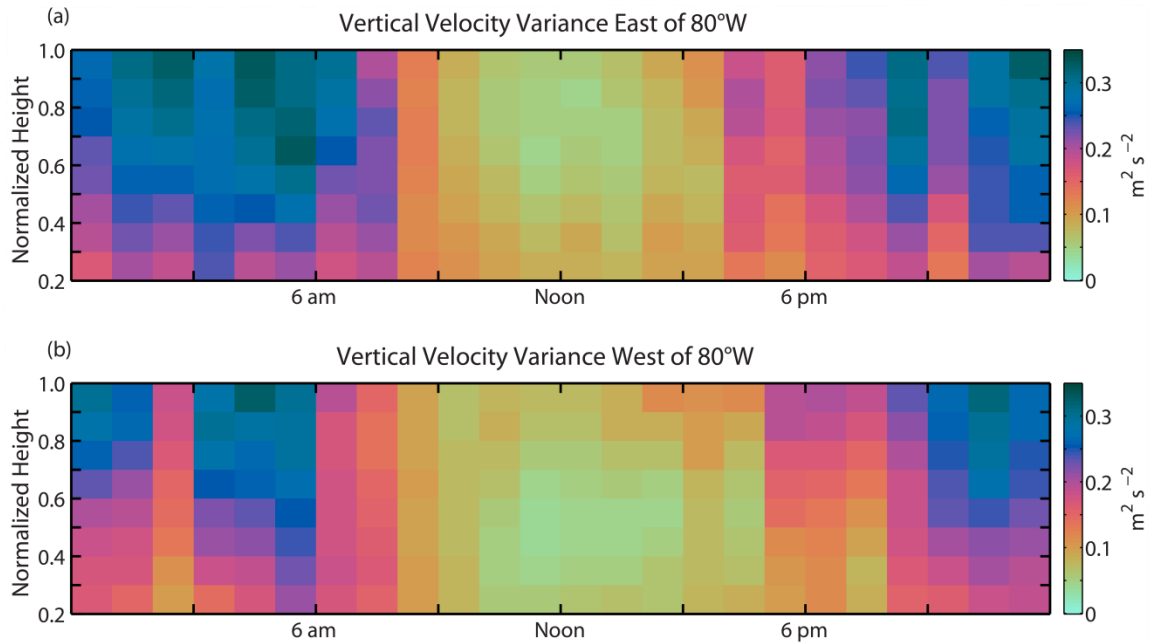


Figure 2.2. Time-height profiles of the mean vertical velocity variance in the boundary layer for the region east (a) and west (b) of 80°W using data from the vertically-pointing Doppler lidar. The profiles are normalized to the base of the cloud such that a height of 1.0 represents the base of the cloud and a value of 0.2 represents a height that is 20% of the measured cloud base height. Individual data points with a signal-to-noise ratio greater than 15 dB are removed to limit the influence of precipitation on the turbulence statistics.

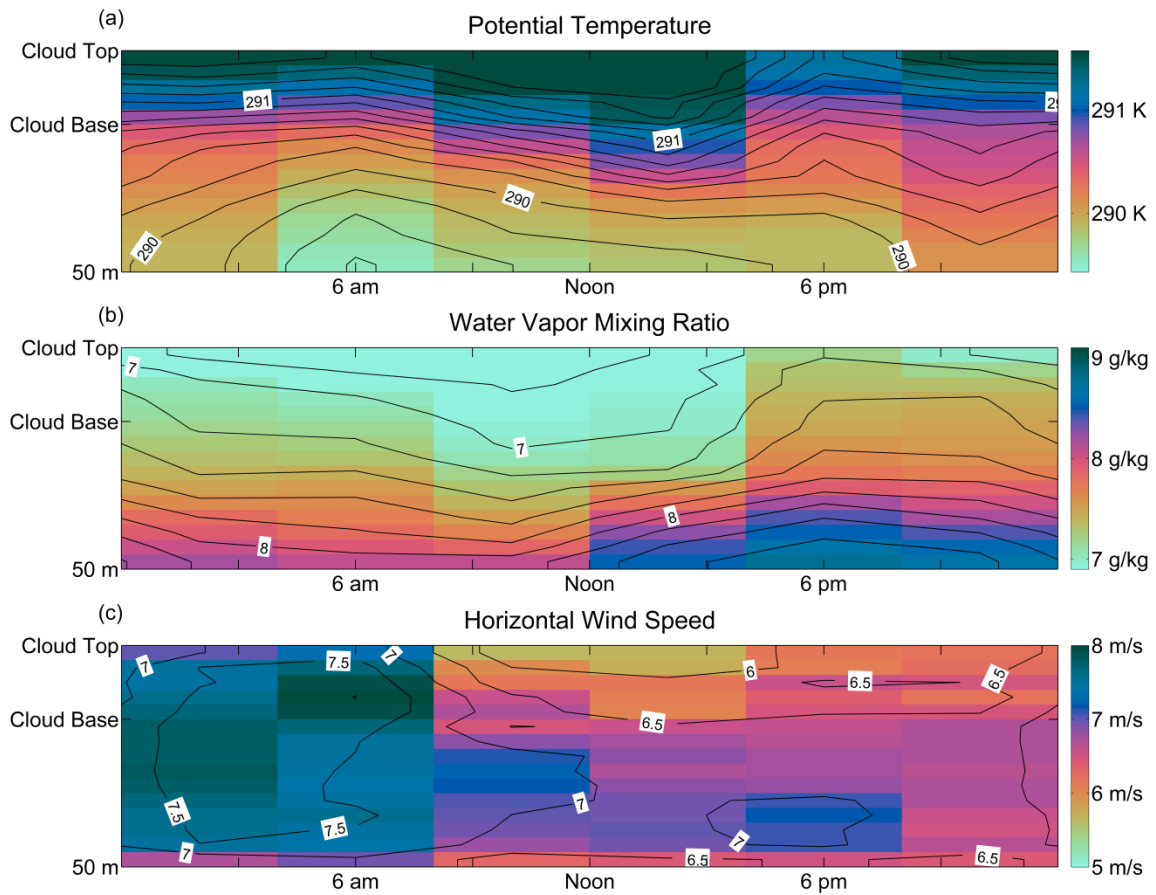


Figure 2.3. Four hour averages of the vertical profiles of potential temperature (a), water vapor mixing ratio (b), and horizontal wind speed (c) from the soundings launched from the RHB. The profiles use the local solar time and are normalized to the base and top of the cloud to capture the relative heights of boundary layer mixing properties. The contour intervals are every 0.15 K for potential temperature, 0.2 g kg⁻¹ for water vapor mixing ratio, and 0.5 m s⁻¹ for wind speed.

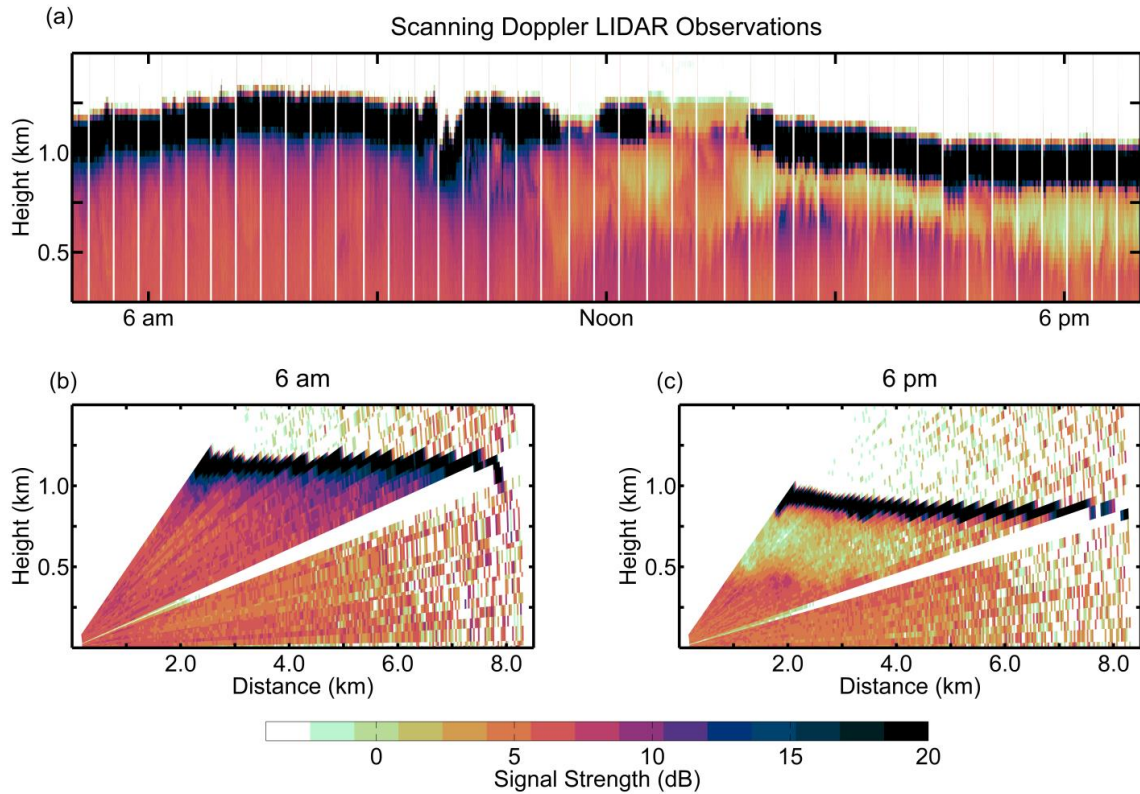


Figure 2.4. Time-height variation of range-corrected backscatter intensity from a vertically-pointing Doppler lidar aboard the *RHB* (a) and select RHI scans from the lidar at 6:00 am (b) and 6:00 pm (c) local time. Data shown was collected on 2 Nov 2008 near 19.6°S and 74.8°W . We plotted the 10-minute blocks of vertically-pointing data, obtained every 20 minutes, close together to make the figure easier to display.

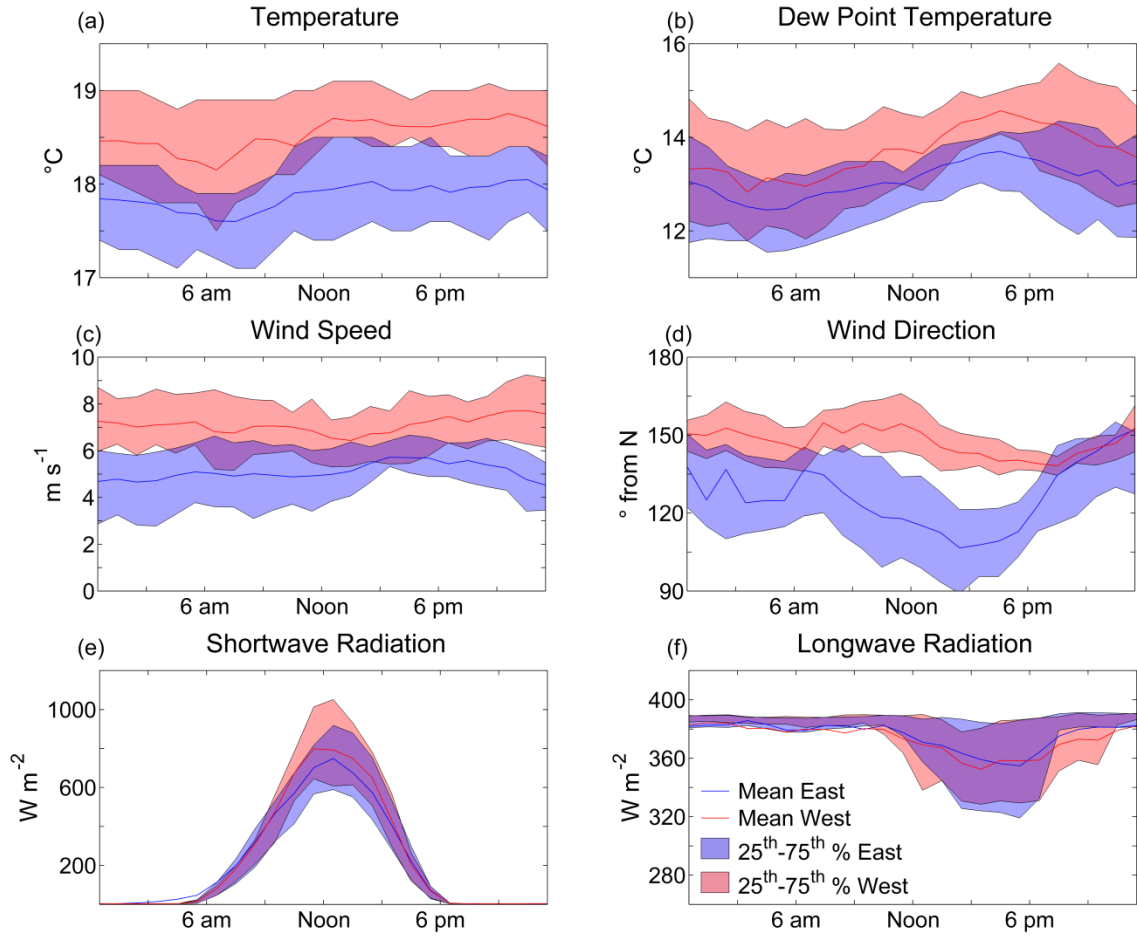


Figure 2.5. Hourly mean (solid line) and interquartile range (shaded region) of the near surface air temperature (a), dew point temperature (b), wind speed (c), wind direction (d), incoming shortwave radiation (e), and incoming longwave radiation (f) from an upward-pointed sensor, plotted as a function of local time for regions east and west of 80°W.

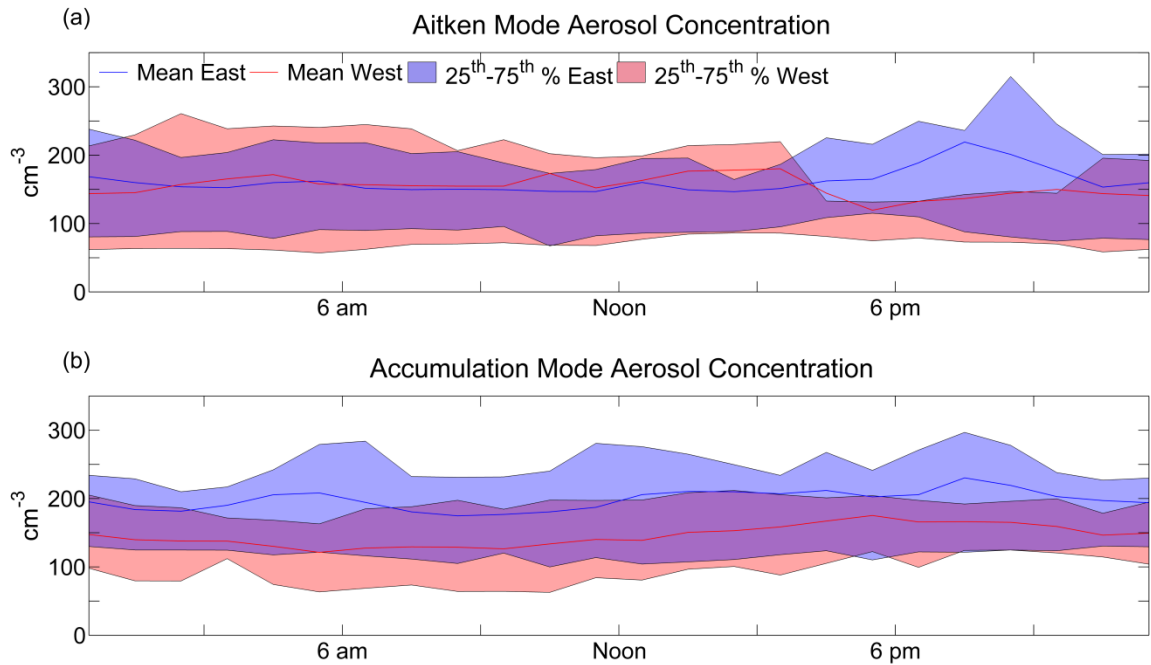


Figure 2.6. Hourly mean and interquartile range of near-surface aerosol concentrations for aerosols smaller than 0.1 μm diameter (roughly Aitken mode; a) and aerosols larger than 0.1 μm diameter (roughly accumulation mode; b) for regions east and west of 80°W.

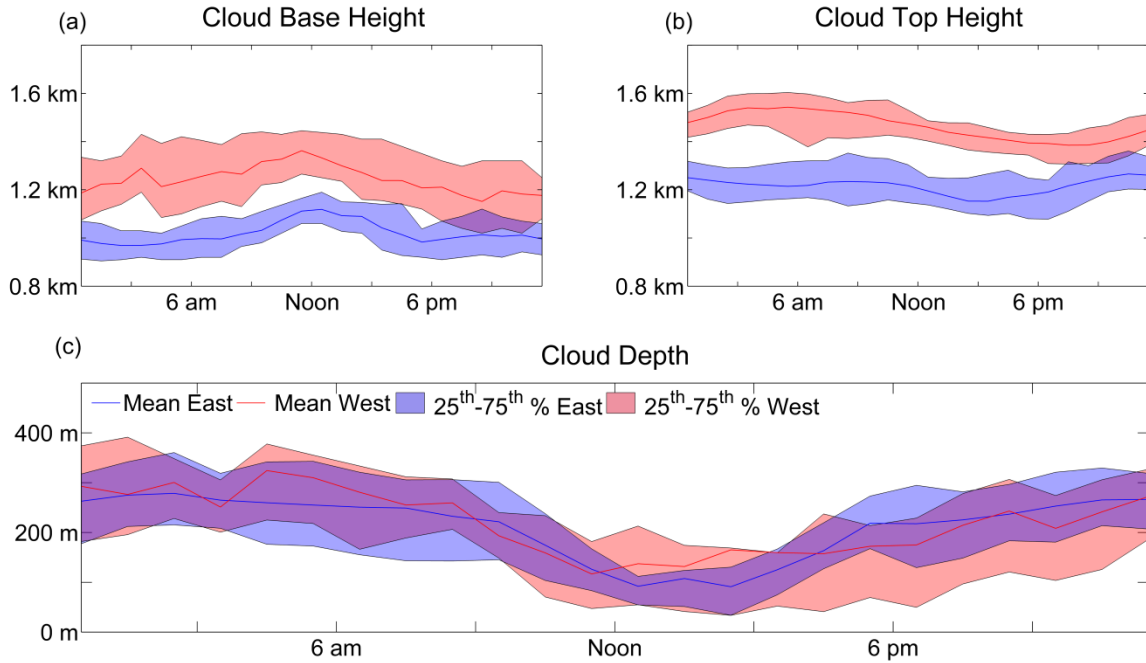


Figure 2.7. Hourly mean and interquartile range of cloud base heights measured by the laser ceilometer (a), cloud top heights measured by interpolating the inversion height measured by the soundings taken every four hours (b), and the resultant depths of the cloud (c) for regions east and west of 80°W.

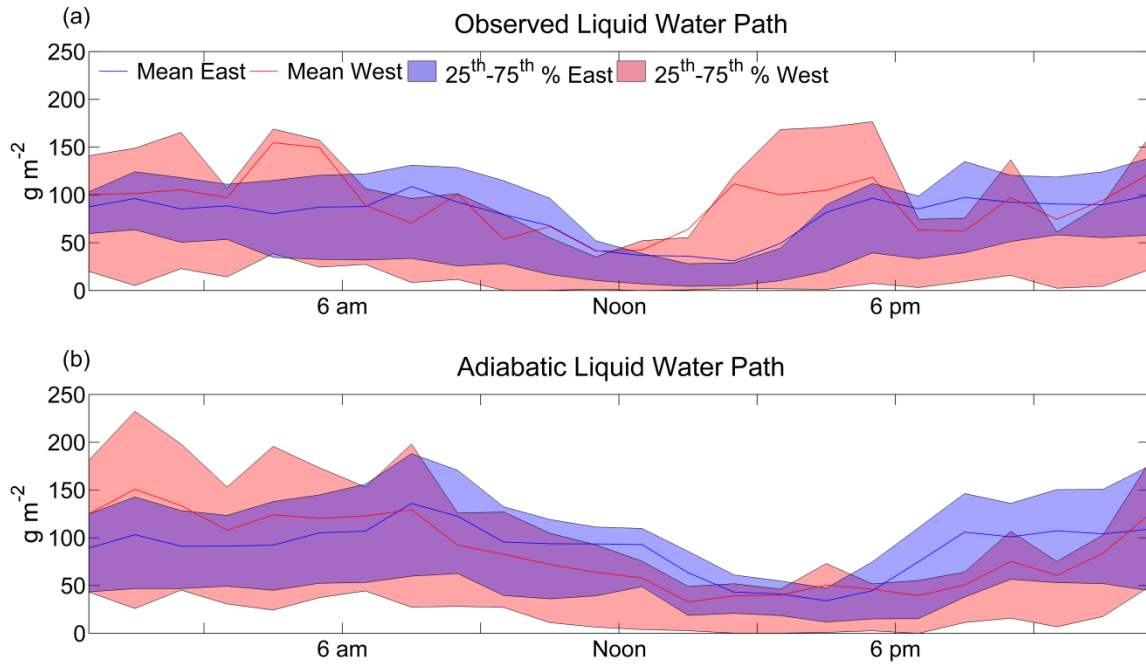
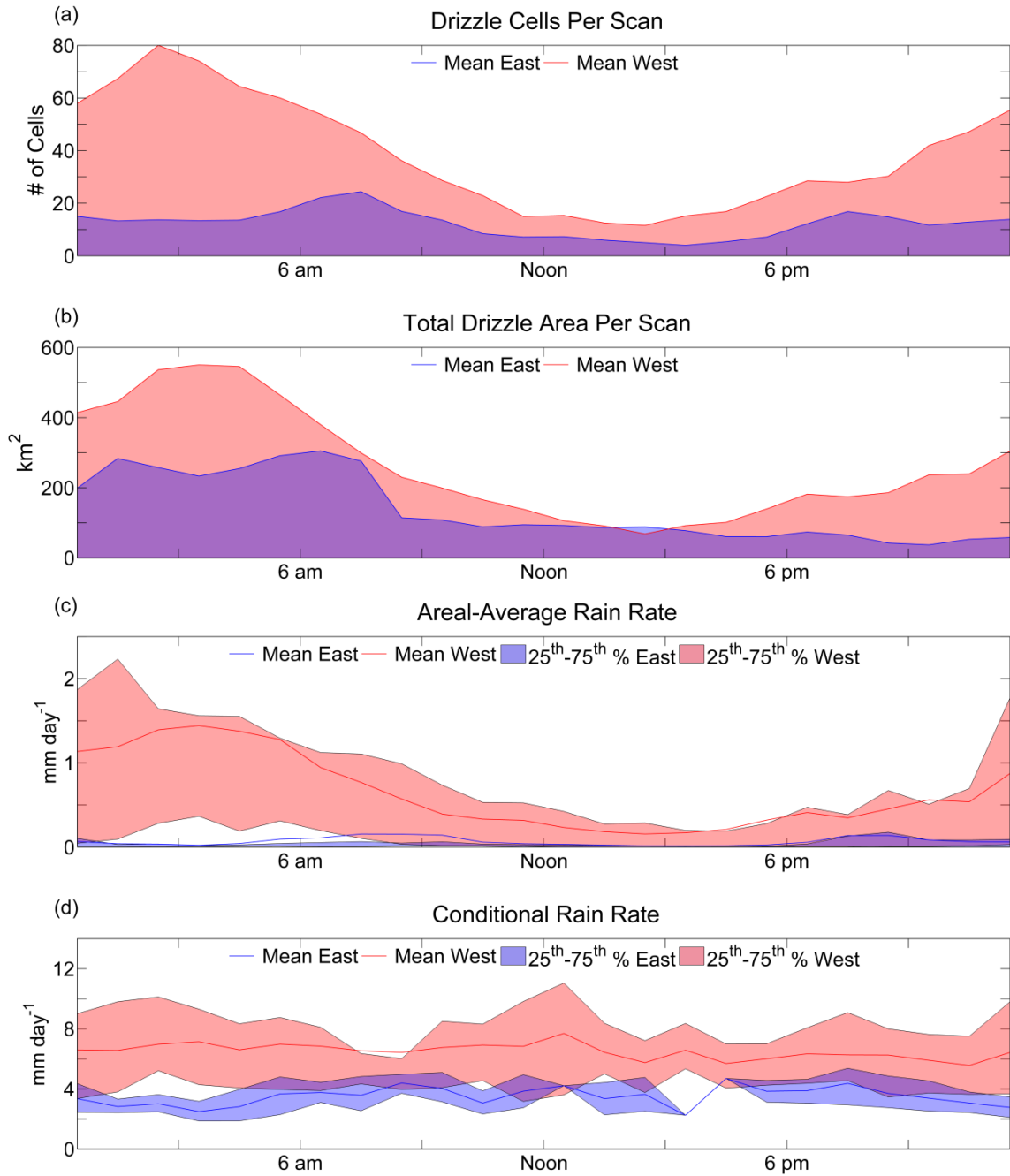


Figure 2.8. Hourly mean and interquartile range of the observed liquid water path (a) and the adiabatic liquid water path derived from the cloud base and height measurements (b) for regions east and west of 80°W .

Figure 2.9. Diurnal variation of the mean number of drizzle cells per scan (a), mean total precipitation area per scan (b), mean (solid line) and interquartile range (shaded region) of the hourly areal-average rain rate (c), and mean (solid line) and interquartile range (shaded region) of the hourly conditional rain rate (d), derived from measurements from the scanning C-band precipitation radar aboard the RHB.



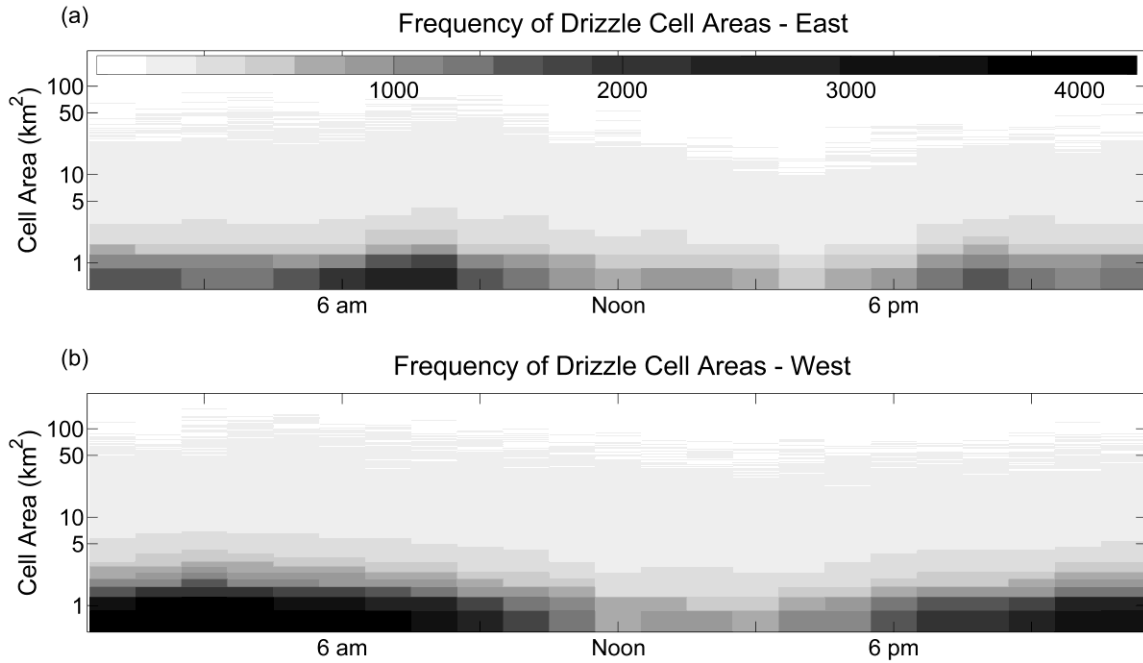


Figure 2.10. Distribution of drizzle cell areas for all precipitation observed during VOCALS-REx for the regions east (a) and west (b) of 80°W. The vertical axis is on a logarithmic scale.

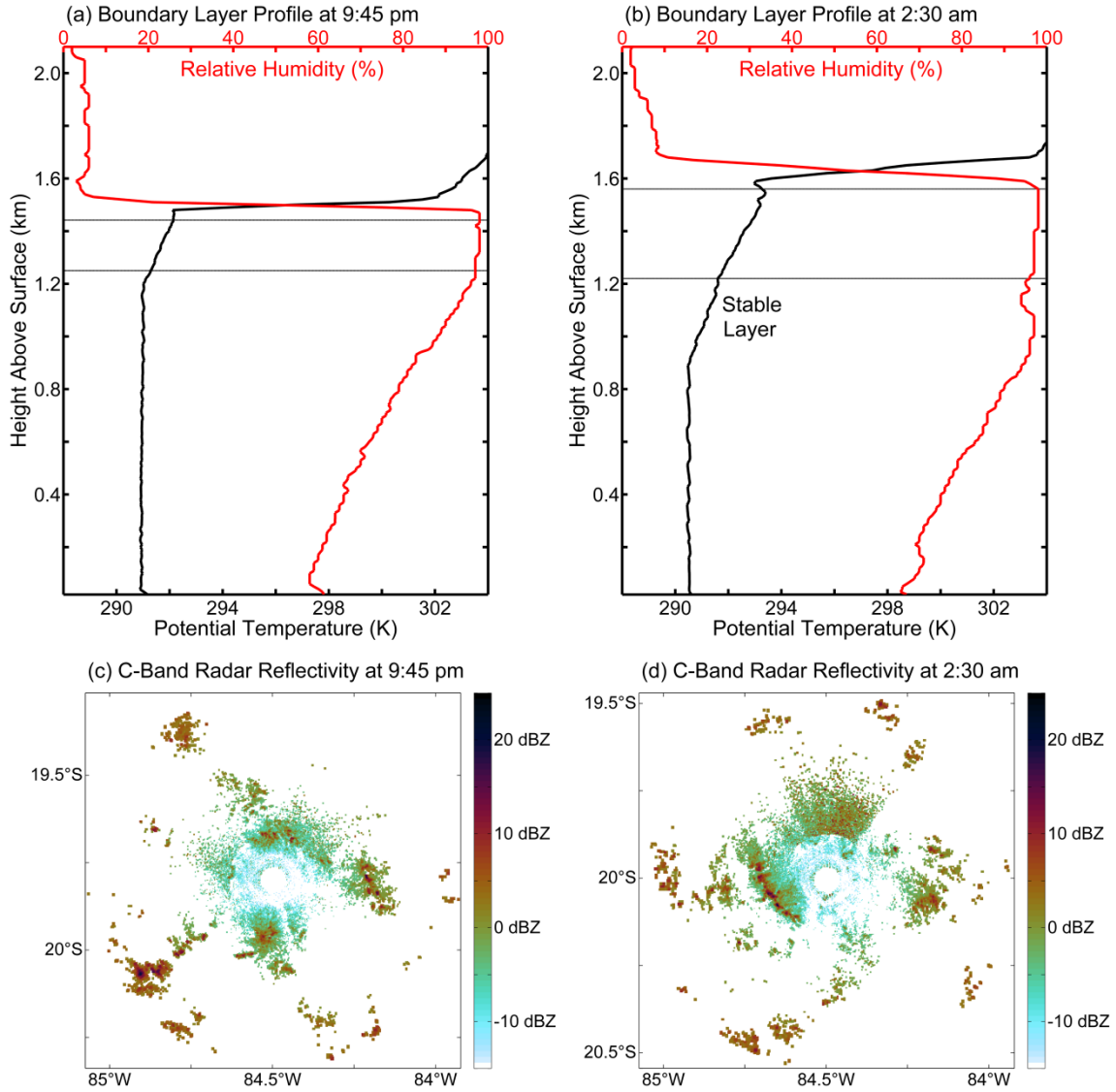


Figure 2.11. Boundary layer profiles of potential temperature (black lines) and relative humidity (red lines) measured by consecutive atmospheric soundings launched at 9:45 pm on 22 November 2008 (a) and 2:30 am (b) on 23 November 2008. Horizontal dotted black lines show the approximate boundaries of the cloud at the time the measurement was taken. The soundings were launched from the *RHB* while it was stationed at roughly 20°S and 84.5°W. Radar reflectivity for the corresponding times is shown in panels (c) and (d).

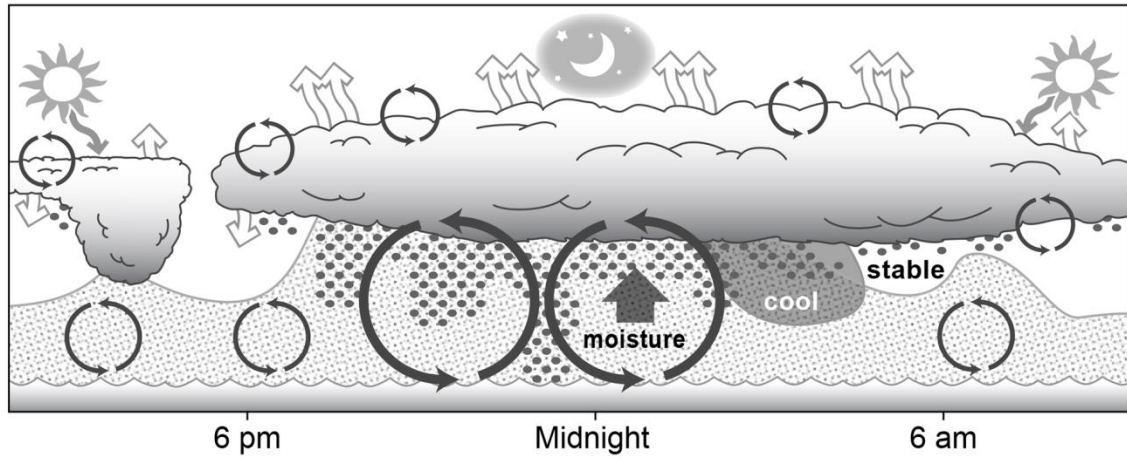


Figure 2.12. Conceptual model showing the most common states of the stratocumulus cloud deck over the diurnal cycle. Precipitation (solid dots), surface mixed layer depth (shaded and dotted region), and turbulent mixing (circulating arrows) all vary regularly across the day.

Chapter 3

Environmental Controls on Stratocumulus Cloud Fraction

3.1 Introduction

Marine stratocumulus clouds are low, liquid-phase clouds that play a critical role in moderating global radiative balance by reflecting large amounts of incoming solar radiation. Given their net cooling effect on the Earth's climate (Manabe and Strickler 1964; Hartmann et al. 1992), it follows that accurately representing the physical characteristics of these clouds, for example the spatial coverage of the cloud deck as a function of time, in general circulation models (GCMs) is important. Current GCMs struggle to produce and maintain stratocumulus in the right place at the right time; this despite increasing efforts and awareness of their impact (Abel et al. 2010; Wyant et al. 2010; Medeiros et al. 2012). Recent studies evaluating climate models and climate system sensitivity and feedbacks have identified cloud-radiative effects, of which marine stratocumulus play a large role, as the largest remaining source of uncertainty in climate model forecasts (Bony and Dufresne 2005; Wyant et al. 2006; Randall et al. 2007; Soden and Vecchi 2011).

Most of the variability of the radiative impact of stratocumulus is due to changes in cloud fraction rather than variations in cloud depth, liquid water path, or albedo (Stephens and Greenwald 1991; George and Wood 2010; de Szoeke et al. 2012). Satellite climatologies of marine stratocumulus show a reduction in shortwave flux reaching the surface of 0.63 to 1 W m^{-2} per 1% cloudiness increase (Hartmann 1992; Klein and Hartmann 1993). The impact of stratocumulus clouds being present can be seen in the daily time series of shortwave flux reaching the surface. In Fig. 3.1 we show a single day's worth of data from a mostly cloudy day (top panel) and a day in which the cloud significantly breaks up during the afternoon (bottom panel). Variations in both longwave and shortwave radiative flux are tied to changes in cloud fraction. Cloud breakup during the afternoon can be seen in the variations of

longwave radiation reaching the surface, which is primarily a function of cloud fraction. In the example shown in the bottom panel the cloud completely breaks up around 11:00 am and the downwelling longwave radiative flux is purely from water vapor in the atmosphere. The key component to this figure is the higher amounts of shortwave radiative flux recorded during the afternoon in the case of a broken cloud field. The peak shortwave flux is $\sim 200 \text{ W m}^{-2}$ higher on the day when the cloud breaks up. In the case of a broken cloud day (bottom panel of Fig. 1), when the cloud reforms briefly in the afternoon the shortwave radiation reaching the surface becomes depressed by as much as $200\text{-}300 \text{ W m}^{-2}$ compared to the normal curve of incident shortwave radiative flux.

Failure to accurately simulate marine stratocumulus cloud fraction is not surprising given the large number of physical processes that have been shown to modify cloud fraction. Field campaigns like the East Pacific Investigation of Climate (EPIC; Bretherton et al. 2004) and the Variability of the American Monsoon Systems' (VAMOS) Ocean-Cloud-Atmosphere-Land Study Regional Experiment (VOCALS-REx; Wood et al. 2011a) as well as numerical simulations of stratocumulus have been used to identify specific processes that can reduce or enhance stratocumulus cloud fraction. These include stability and inversion strength (Klein and Hartmann 1993; Wood and Bretherton 2006; Zhang et al. 2009; Myers and Norris 2013), subsidence (Zhang et al. 2009; Myers and Norris 2013), the diurnal cycle of subcloud turbulent mixing (Turton and Nicholls 1987; Duynkerke 1989; Betts 1990), mesoscale circulations (Atkinson and Zhang 1996), drizzle (vanZanten and Stevens 2005; Comstock et al. 2005; Wood and Hartmann 2006), near-surface outflow boundaries and density currents (Feingold et al. 2010; Terai 2011; Wilbanks 2013), aerosols (Albrecht 1989; Pincus and Baker 1994), boundary layer depth (Bretherton and Wyant 1997; Wood and Hartmann 2006; Mechem et al. 2012), gravity waves (Allen et al. 2012), and many others. A summary of these processes is given in Table 3.1.

The level of our understanding of how these processes can impact cloud fraction ranges from strong to open debate. An example of a high confidence relationship is the

physical link between stability and cloud fraction. Klein and Hartmann (1993) showed that seasonal cycles in subtropical stratocumulus cloud fraction can be largely explained by the seasonal variations in stability and inversion strength associated with the intensity and location of the subsidence branch of the Hadley Cell. The physical connection is straightforward: an inversion, such as those that are driven by subsidence and cap the subtropical marine boundary layer, acts to prevent moisture from detraining from the boundary into the free troposphere (Klein and Hartmann 1993). Stronger inversions also reduced the rate at which dry air entrains into the boundary layer (Bretherton and Wyant 1997). The combined effect of these two processes allows moisture to accrue in the boundary layer and clouds form as a result (Myers and Norris 2013). Another example of a well-known physical relationship is the connection between the strength and depth of turbulent mixing in the boundary layer and the diurnal cycle of cloud fraction (Turton and Nicholls 1987; Duynkerke 1989; Burleyson et al. 2013). Turbulent mixing acts to transport moisture vertically from the moist near-surface layer into the cloud (Lilly 1968; Nicholls 1984; Turton and Nicholls 1987). With a steady supply of moisture, which occurs more often at night, clouds persist against entrainment drying and cloud fractions are generally high. During the daytime when turbulent moisture transport is weaker or nonexistent clouds are cut off from their moisture supply and cloud fractions decrease as a result (Betts 1990).

Because stratocumulus-topped boundary layers are turbulently mixed from the top down, the primary driver behind variations of the strength and depth of turbulent mixing are changes in radiative divergence at cloud top (Nicholls 1984; Betts 1990; Caldwell et al. 2005). Strong longwave cooling is concentrated in the upper few meters of the cloud (Nicholls and Leighton 1986; Stevens et al. 2003a; Wood 2005a). Under a nocturnal clear dry troposphere with limited downwelling longwave radiation the radiative flux divergence at cloud top is 50-90 W m⁻² (Nicholls and Leighton 1986; Siems et al. 1993; Wood 2005a; Caldwell et al. 2005; etc.). Bretherton et al. (2010) recorded longwave flux divergence as high as 102 W m⁻² in the SE Pacific during VOCALS-REx. These values are higher than the reported values in the other subtropical stratocumulus regions indicating the longwave

generation of turbulence may be strongest in the SE Pacific. Longwave radiative divergence at cloud top drives strong localized cooling, with measured rates between 0-5 K hr⁻¹, concentrated very close (10s of meters) to cloud top (Slingo et al. 1982a; Nicholls and Leighton 1986). During the day, some of this cooling can be offset by the absorption of solar radiation (Nicholls 1984; Turton and Nicholls 1987; Duynkerke 1989; etc.). Up to 15% of incident solar radiation can be absorbed by the cloud with the absorption divided roughly 50-50 between water vapor and liquid cloud droplets (Stephens 1978a; Slingo and Schrecker 1982; Slingo 1989; Taylor et al. 1996; etc.). Given downwelling solar radiative fluxes at noon greater than 800 W m⁻² in the subtropics, even limited absorption within the cloud layer is enough to offset much of the radiative flux divergence at cloud top (10% x 800 W m⁻² = 80 W m⁻²). This means that it takes only modest amounts of shortwave radiative flux to offset longwave cooling at cloud top. Previous work has shown that a reduction in the generation of negatively buoyant parcels that act to mix the subcloud layer occurs shortly after sunrise (Duynkerke 1989). Shortwave heating rates within the cloud are dependent on the drop size distribution and the vertical distribution of liquid water content but vary between 0-2 K hr⁻¹ (Stephens 1978a). If not balanced by longwave cooling, net heating of the cloud from solar absorption can lead to the evaporation of cloud water and in extreme cases the breakup of the cloud (Betts 1990).

The driving forces behind seasonal and diurnal cycles of cloud fraction have been in the literature for close to 30 years and models simulating stratocumulus-topped boundary layers should seek to reproduce these relationships. However, in the past decade additional processes have been connected to cloudiness transitions, namely precipitation, or rather aerosol-cloud-precipitation interactions, and mesoscale processes such as gravity waves and near-surface density currents. Our understanding of these processes and how they interact with stratocumulus cloud fraction has been built from new datasets generated during field campaigns (EPIC and VOCALS-Rex), from satellites (MODIS and CloudSat), and the computational power available to run large-eddy scale (LES) simulations of cloud-topped boundary layers. Many of these processes have been studied with regards to their relationship

to pockets of open cells (POCs – Bretherton et al 2004; Stevens et al. 2005a). POCs are mesoscale regions of open-cellular cloud structures embedded within or adjacent to regions of closed-cellular cloud fields. The most important physical characteristic of POCs is their low cloud fraction in comparison to closed-cellular regions, which allows more incoming solar radiation to reach the surface. Given that stratocumulus clouds are climatologically important because of their role in modifying the global radiative balance, the change in shortwave radiative flux associated with the formation of POCs has generated considerable interest within the community.

Wood et al. (2008) was among the first to attempt to quantify the frequency of occurrence and environmental characteristics associated with POC formation. In the two cases studies presented in their paper, Wood et al. describe scenarios where cloud fractions decrease from nearly overcast (100%) to less than 60%. In total they identified 23 POC formation events in the SE Pacific within two months of data. The vast majority (> 80%) of these cases formed overnight and on short time scales (Wood et al. 2008; their Fig. 10a). The nocturnal and rapid formation of POCs implies that the physical processes leading to their development (or more clearly – leading to a reduction in cloud fraction within the POC region) are not related to the diurnal cycle of cloud fraction that results from the daytime reduction in turbulent mixing in cloud-topped boundary layers. POCs forming at night could modify the shortwave flux the following day by removing areas of cloud that would otherwise reflect some shortwave radiation during the day.

The question of what processes lead to POC formation has been actively pursued for close to a decade. Early observational evidence pointed to the role of precipitation, which can act to remove aerosols and stabilize the subcloud layer thus reducing vertical moisture transport into the cloud, as being an important factor (Stevens et al. 2005a; Savic-Jovicic and Stevens 2008; Wang and Feingold 2009). Comstock et al. (2007) showed that POCs have both larger and more intensely drizzling cells compared to neighboring closed-cellular regions. Later research built upon these observations and hypothesized that coalescence

scavenging via precipitation contributes to the formation and maintenance of open-cellular structures (Wood et al. 2011a). The net result of these works was the conclusion that drizzle is likely a necessary condition for the formation and maintenance of POCs. The community-wide desire for clarity of these processes directly led to the VOCALS project which took place in 2008. The relationship between aerosol-cloud-precipitation interactions and POCs were the basis of two of the four meteorological hypotheses that motivated the VOCALS program (Hypotheses H1b and H1d; Wood et al. 2011a).

While results from VOCALS did shed some light on the behavior of POCs, significant questions remain. The dominant question is clearly stated in the VOCALS overview paper that highlights the results and remaining questions from the project (Mechoso et al. 2013): “The frequency and climatic importance of POCs remains poorly-characterized. A full assessment of all triggering mechanisms for POC formation given realistic aerosols and meteorology has not yet been completed.” In other words, the importance of POCs relative to other sources of cloud fraction variability has not been examined. Case studies of individual POCs, of which there were five sampled by the C-130 during VOCAL-REx, cannot answer this question (Wood et al. 2011a; Wood et al. 2011b; Berner et al. 2013).

If POCs are frequent and climatologically important then, given the relationships between a plethora of physical processes and POC formation, the list of processes that must be adequately simulated in GCMs seeking to correctly simulate stratocumulus cloud fraction grows significantly. One could argue that a model would need to capture all of the processes or parameters listed in Table 3.1 in order to predict POCs. Correctly simulating any single one of these processes and their relation to cloud fraction in a GCM is a challenge. To further complicate matters, almost all of these controlling processes can be linked to the others via first order mechanisms so that they constantly modify, and are in-turn modified by, each other. Additionally, many of these processes occur or vary on spatial scales that are 1-2 orders of magnitude smaller than a typical GCM grid box (~100 km). This means that, with

few exceptions, processes controlling stratocumulus cloud fraction need to be parameterized in GCMs.

Failure to properly parameterize stratocumulus physics leads directly to errors and biases in GCMs (Medeiros et al. 2012). Some of these parameterizations, like the empirical cloud fraction-LTS relationship proposed by Klein and Hartmann (1993) and implemented by many including Miller (1997), can be fairly direct. Other relationships are more complex and circuitous. Take for example the marine boundary layer moist turbulence scheme developed by Bretherton and Park (2008), which attempts to identify and simulate the presence of individual subcloud turbulent layers, each of which can be an order of magnitude smaller than the vertical resolution of the model. More complicated still would be designing a method to simulate the effects of drizzle-induced outflow boundaries and density currents, dozens of which may be occurring in a single grid box. It is highly unlikely that GCMs will explicitly resolve these processes in the near future.

The expansiveness of the list of processes which can influence stratocumulus cloud fraction and the complicated parameterizations they require poses a significant problem for the community. With limited resources (time, personnel, computing, etc.) and a strong impetus to act, in which direction should the efforts of the community be focused? How many of these processes must we adequately simulate to produce accurate stratocumulus cloud fractions? Will different stratocumulus regions require fundamentally different parameterizations? Many previous studies have documented the impact of singular processes or parameters on stratocumulus cloud fraction (a good review is provided by Wood [2012]). However, empirical evidence on the relative importance of different processes (POCs, diurnal and seasonal cycles, precipitation, etc.) on cloud fraction is sparse. This chapter is an analysis of cloud fraction variability that seeks to identify a subset of processes that have the largest impact on stratocumulus cloud fraction. Our hope is to guide the development of future parameterization schemes by whittling down the list to a few key variables. Additionally, this work is among the first to examine in combination controls on cloud

fraction in each of the three main stratocumulus regions (the NE Pacific, SE Pacific, and SE Atlantic). Identifying the similarities and differences among environmental controls in each region will help to determine if a single parameterization approach is appropriate in all three regions.

One of the limitations in evaluating the relationships among various processes and stratocumulus cloud fraction is the lack of an appropriate low cloud detection dataset to capture cloudiness variability on an appropriate range of spatial and temporal scales – particularly sub-diurnal frequencies. Some datasets, for example the International Satellite Cloud Climatology Project (ISCCP; Rossow and Schiffer 1991) or the Climatic Atlas of Clouds Over Land and Ocean (Hahn and Warren 2007), provide useful avenues to explore variability on seasonal or longer times. ISCCP data provides information on average cloud fractions over several hundred kilometers on time scales as small as three hours and as large as seasonal means. Similarly, the cloud atlas database provides mean cloud fraction over areas on the scale of $5^\circ \times 5^\circ$. These data products are widely used and can effectively capture gross features of the seasonal and diurnal cycles of stratocumulus clouds as well as long term trends in cloudiness. However, their poor spatial resolutions limit their effectiveness at identifying mesoscale cloudiness transitions such as POCs.

In addition to the spatial resolution limitations, many of the controlling processes thought to be important to stratocumulus vary on weekly, daily, and hourly time scales. For example, drizzle, density currents, and gravity waves have all been shown to have significant diurnal cycles and can appear and disappear in windows much smaller than the three hour averages available in the ISCCP or cloud-atlas datasets (Allen et al. 2012; Wilbanks 2013; Burleyson et al. 2013). The four-times daily cloud fraction estimates from the sun-synchronous Moderate Resolution Imaging Spectroradiometer (MODIS; Platnick et al. 2003) sensor aboard NASA's Terra satellite can capture gross features of the diurnal cycle, but provides no information on time scales of a few hours. Polar-orbiting satellites also require the stitching together of adjacent swaths to allow for a complete viewing of the rather large

stratocumulus cloud decks. The swath issue creates edge effects that can hamper cloud identification and leads to a phasing of observation times between subsequent adjacent overpasses. Their limited temporal resolutions restrict the utility of these commonly used datasets in answering the questions posed in this chapter.

Visible imagery from geostationary satellites has a rapid update time and the necessary spatial resolution, but does not work at night. This limits the ability of visible data to capture cloudiness transitions such as POC formations which primarily occur at night (Wood et al. 2008). Some previous studies, for example de Szoeke et al. (2012), have used surface-based cloud fraction retrievals obtained during field campaigns. While these datasets often have high temporal and spatial resolution and continuity, they are by necessity time limited and are only available in a single stratocumulus region. This means field campaign data has limited usefulness in comparing and contrasting cloud fraction behavior among different stratocumulus cloud decks.

Analysis of cloudiness transitions in this chapter is built primarily upon a new cloud identification dataset derived from geostationary observations of the infrared (IR) emission of stratocumulus clouds. IR brightness temperatures can be retrieved at any time of day and the geostationary platform allows for a rapid update time and a homogenous field of view in all three subtropical stratocumulus decks. By converting the pixel-scale IR brightness temperatures into cloudy and cloud-free pixels we can retrieve cloud fraction overnight. We use the 4 km Global IR Dataset (a.k.a. TRMM Ancillary Merged IR) from the Climate Prediction Center, National Center for Environmental Prediction, and the National Weather Service (Janowiak et al. 2001; http://www.cpc.ncep.noaa.gov/products/global_precip/html/README). The global IR (hereafter merged-IR) product merges data from multiple geostationary satellites (GOES, METEOSAT, and GMS) into a spatially complete field of IR brightness temperatures from 60°S to 60°N around the globe at 30 minute time resolution. The merged-IR dataset allows us to perform analysis of cloud fraction variability on short time scales, across the diurnal

cycle, and to replicate the analysis in each of the subtropical stratocumulus decks in the NE Pacific, SE Pacific, and SE Atlantic.

The availability of IR-based cloud maps at night is a critical component of this study. Not only do most POCs form overnight, but the juxtaposition of relevant processes overnight creates an interesting set of natural experiments. It is well known that increased boundary layer turbulence overnight is connected with increasing cloud fractions (e.g. Lilly 1968; Nicholls 1984; Turton and Nicholls 1987). However, precipitation, which has a strong maximum in area and areal-average rain rates overnight, is thought to be associated with decreasing cloudiness (Stevens et al. 2005a; Savic-Jovicic and Stevens 2008; Wang and Feingold 2009; Burleyson et al. 2013). An additional parameter – boundary layer depth, which for a given location is maximized overnight – is also associated with a negative tendency in cloud fraction (Wood and Hartmann 2006; Mechem et al. 2012). Analyzing the patterns of overnight cloud fraction changes that result from the superposition of these processes, one of which creates a tendency for cloud fraction to increase overnight and two of which create negative tendencies, is an indirect way to gauge the relative importance of each process. Every night at a given location is a miniature natural experiment in which our IR cloud identification methodology allows us to record the data points at different times during the experiment and shed light on the relative importance of the underlying process. Answering the question of the relative importance of various processes to cloudiness changes overnight will go a long way toward diagnosing why models often fail to produce accurate diurnal cycles of stratocumulus cloud fraction (ex. Wyant et al. 2010; their Fig. 11).

In the Data and Methods section we outline of our method for converting the IR temperatures into low cloud maps. We discuss multiple ways in which we evaluate the fidelity of our new product by comparing our results to previously used datasets on annual and seasonal scales. In the results section, we document the patterns associated with the diurnal cycle of cloud fraction and the relative role of various environmental processes. Finally, we close by summarizing our findings.

3.2 Data and Methods

3.2.1 Description of the Cloud Identification Methodology

Longwave emission from the atmosphere, clouds, ground, and ocean is measured by a variety of geostationary and polar-orbiting satellites managed by various national agencies. Of these platforms, the geostationary satellites provide a full disk view of emission over large contiguous areas with update times ranging from minutes to hours. Utilization or combination of these geosynchronous IR datasets is hampered by the restrictions associated with getting data from multiple agencies of various nationalities, subtle differences in the observation strategies and instrument characteristics of different satellites, and the fact that different satellites view different areas around the globe. The benefit of the merged-IR dataset is that the legwork involved in combining multiple datasets, each of which has its own unique characteristics, together has already been completed. The merged-IR dataset also provides a consistent view of infrared emission around the globe without requiring the stitching together of differing fields of view from multiple geostationary satellites or different sampling swaths from a single polar-orbiting satellite.

The merged-IR data is available every 30 minutes from February 2000 onward and has a native spatial resolution of 4 km x 4 km. One issue in measuring emission from space is the extinction of radiation as it traverses through the atmosphere from the source to the instrument. This is particularly an issue at high viewing angles where radiation emitted is more strongly attenuated after passing through longer paths of the atmosphere (Wark et al. 1962). The merged-IR data product has an empirical zenith angle correction built using adjacent satellites whose field of view overlaps along the edges (Janowiak et al. 2001). This correction means the merged-IR product is a consistent measurement across the full field of view. The zenith angle correction also reduces the spatial discontinuities at the boundaries between the fields of view of neighboring satellites. Intercalibration between satellites was not performed in the version of the merged-IR product we used (Version 1), but the

intercalibration effect is likely an order of magnitude smaller than the viewing angle dependence effect (Joyce and Arkin 1997).

Low cloud fraction, defined here to be the area fraction of warm clouds ($T > 273$ K), in this study will be determined using a new method that is applied to the dataset of merged-IR brightness temperatures. IR brightness temperatures measured by satellite are the radiative emissions from both the cloud and the underlying ocean surface. Stratocumulus clouds are largely transparent to the outgoing longwave radiation from the underlying ocean surface (Hartmann et al. 1992). This means the IR emission measured for cloudy pixels is a combination of the emission from the cloud and the ocean. To be usable as a cloud identification tool, we must be able to classify whether the measured emission for a given pixel is the combined emission from cloud and the underlying ocean (a cloud is present within the pixel) or is only the emission from the ocean surface (the pixel is cloud free). This is made possible by the fact that low clouds and the ocean surface emit radiation at slightly different temperatures. Looking at IR brightness temperatures from individual scenes over the subtropical stratocumulus regions, it is possible to distinguish by eye areas of cloudy and cloud free pixels (left panel of Fig. 3.2). The distribution of IR brightness temperatures for a single scene reflects the relative frequency of cloud (lower temperature mode) and ocean (higher temperature mode) pixels (right panel of Fig. 3.2). By identifying the temperature that separates the two modes (hereafter the separation temperature), a low cloud mask can be created the scene. Each pixel within the scene can be identified as either cloud or ocean by comparing the IR brightness temperature of the pixel to the separation temperature, with pixels with IR temperatures colder than the separation temperature classified as clouds and pixels with IR temperatures warmer than the separation temperature classified as ocean.

Cloud top temperature and SST in the stratocumulus regions each vary slowly in both space and time (de Szoeko et al. 2012). Hence, accumulated distributions of IR brightness temperature over several weeks or over a large area often show a more clearly bimodal structure compared to distributions from single scenes (top panel of Fig. 3.3). In this study,

the IR brightness temperature distributions are accumulated over a moving 4-week window centered on a given day. The distributions are spatially aggregated in $3^\circ \times 3^\circ$ (roughly 6800 4 km x 4 km pixels) boxes that cover each of the subtropical stratocumulus regions. The separation temperature between the cloud and ocean temperature modes in each box and time window is found in one of two ways. It is necessary to use two methods because in some seasons and regions cloud fractions are sufficiently high such that only the lower temperature cloud mode is present or sufficiently low such that only the higher temperature ocean mode is present. In these regions the IR brightness temperature distribution is no longer clearly bimodal.

Method 1) In this more straightforward case, the distribution of IR brightness temperatures is strongly bimodal, meaning there is a clear minimum in frequency between the cloud and ocean surface modes (top panel of Fig. 3.3). When this occurs, the separation temperature is defined as the temperature with the minimum frequency that occurs between the two modes in the daytime data distribution. The underlying premise is that the minimum frequency between the two modes corresponds to the temperature that is least likely to be in either the cloud or cloud free mode and thus most likely to separate the two. The daytime distributions are used because cloud fraction is most often minimized during the day (Turton and Nicholls 1987; Betts 1990; de Szoeki et al. 2012), creating a more evident SST mode to compare against. Implicit in the use of daytime scenes to identify a separation temperature is the assumption that SSTs do not vary significantly (more than 1-2 K) across the diurnal cycle (de Szoeki et al. 2010a; Painemal et al. 2010).

Method 2) A slightly different approach is required in regions where only one of the lower temperature cloud mode or the higher temperature ocean mode is present. These tend to be regions of very high or very low cloud fractions. In these areas, the distribution of IR brightness temperatures aggregated in space and time has a unimodal or weakly bimodal distribution even during daytime scenes (bottom panel of Fig. 3.3). When this occurs, we first take the derivative of the daytime IR brightness temperature distribution and then select the

temperature warmer than the colder temperature mode (in high cloud fraction regions where mostly cloudy pixels are present) or colder than the higher temperature mode (in low cloud fraction regions where mostly cloud free pixels are present) in which the derivative goes closest to zero. This temperature is chosen in an attempt to isolate the lone mode that is present in the IR brightness temperature distributions. This approach to identifying the separation temperature is applied only rarely within the stratocumulus regions used in this analysis.

Once a separation temperature is found for every box and every day, the time series of daily separation temperatures for a given box is filtered to remove outliers (data points in which the separation temperature for a single day differs from the running two week mean value by more than 2 K) and then interpolated in time to fill in gaps in time where neither method found a reasonable separation temperature (roughly 5-10% of the time). The time series for each $3^\circ \times 3^\circ$ box is then used to create a separation temperature map for every day. We use spatial interpolation between boxes to reduce horizontal discontinuities in the separation temperature found for adjacent boxes. This creates a separation temperature map that is smoothly varying in both space and time. Once we have a separation temperature map for every day we can create a cloud map for all 30 minute scenes during that day by identifying pixels colder (cloud) and warmer (ocean) than the separation temperature.

Our method of identifying low cloud pixels is designed for regions in which cloud top temperatures and sea surface temperatures are spatially homogeneous and both vary slowly in time. The subtropical stratocumulus regions are therefore good candidates for the application of this methodology. We restrict our analysis to areas where low clouds, mostly stratocumulus but possibly cumulus, are the primary cloud type. A rough method to identify areas where the cloud type is predominantly low clouds is to look at the frequency of ice clouds (cloud top temperature colder than 273 K). The annual mean ice cloud frequency is shown as black contours in the left column of Fig. 3.10. Our analysis is based solely on data collected in areas where clouds with ice occur less than 35% of the time.

In addition to limiting our analysis to regions where ice clouds are infrequent, our low cloud fraction calculations are the area fraction of clouds with IR brightness temperatures warmer than 270 K – a conservative threshold for separating clouds colder than freezing. Only the low cloud fractions are used in the quantitative portion of our analysis where we are interested in low cloud variability. In addition to the low cloud masks, we also create a total cloud mask which allows us to compare our cloud identification methodology against other products that do not discriminate between low and high clouds (for example the MODIS total cloud product). The total cloud masks are all pixels colder than the separation temperature, not just those warmer than 270 K. The total cloud masks are not used in the quantitative portion of our analysis.

3.2.2 Evaluation of the Cloud Identification Methodology

The most direct qualitative method to evaluate the performance of the cloud identification methodology is to compare cloud masks from our product to Geostationary Operational Environmental Satellites (GOES) visible albedo maps during daytime scenes. In Fig. 3.4, we show one such comparison over the southeast Pacific from 1600 UTC on 11-October 2008. From a regional perspective (left column) our product captures the broad scale features of the stratocumulus cloud deck, including the east-west decrease in cloudiness and the reduction in cloud fraction along the Peruvian coastline. The right column shows a smaller $8.5^\circ \times 8.5^\circ$ region in which we can compare finer scale details of the cloud deck. Our methodology picks up on the high cloud fraction characteristics of the closed cellular regions in the southeast and northeast corners of the plot as well as many of the intricate cloud edges within the open cellular region in the center of the frame. Our cloud map does not capture some of the very fine scale features like the slight reduction in cloudiness between adjacent cells in the closed cell regions. Comparing the raw brightness temperature maps (top row) to the GOES visible albedo plots (bottom row) leads us to believe that these subtle differences are not an erroneous identification of cloudiness but rather are due to discrepancies in the native resolution of the IR (4 km x 4 km) and the GOES visible albedo data (1 km x 1 km).

The impact of the coarser IR resolution is minimized in our analysis by only considering cloud fraction variability on spatial scales much larger than an individual pixel.

We can also compare our cloud identification data with the MODIS cloud product, which contains a numeric cloud fraction for each pixel that allows for a more quantitative evaluation. The MODIS MOD06_L2 cloud product is a widely used dataset that provides fractional cloudiness values for pixels with a 5 km x 5 km surface resolution during each of the four-times daily overpasses at roughly 10:30 am/pm and 1:30 am/pm locally (Platnick et al. 2003). One complication of this comparison method is that the MODIS product gives fractional cloudiness values for each 5 km x 5 km pixel. In contrast, the merged-IR cloud mask is a binary (either cloud or no cloud) value for each 4 km x 4 km pixel. So despite the fact that the pixel resolution of the two products is roughly equal, a transfer standard must be established to convert the MODIS cloud fraction for each pixel to a binary cloud mask. We used an iterative error minimization approach where we compared error statistics computed using varying thresholds between 0-1 to create a robust transfer standard. A threshold value of 0.87 had the smallest root mean squared error between the MODIS cloud fractions and our merged-IR cloud fractions. In other words, an individual MODIS pixel must be filled with clouds that cover 87% of the pixel area (25 km^2) before our algorithm will likely identify the associated merged-IR pixel (16 km^2) as being cloudy. While evaluating our product we compare our merged-IR cloud masks to the multispectral MODIS product by classifying all MODIS pixels with fractional cloudiness greater than 0.87 as cloud and all remaining pixels as ocean. The transfer standard was designed to minimize the *total error* for the entire time series and thus may not produce the right conversion for an individual scene. Additionally, the MODIS cloud fraction used is the total cloud fraction – meaning that it includes the fractional cloudiness from both low ($T > 273 \text{ K}$) and high ($T < 273 \text{ K}$) clouds. To account for this, when comparing against the MODIS product we do not filter our data to only include pixels with brightness temperatures warmer than 270 K.

An example of the twice daily MODIS cloud fraction values compared against the 30 minute merged-IR cloud fractions is shown in Fig. 3.5. Here we compute cloud fraction in $3^\circ \times 3^\circ$ boxes for each of the stratocumulus regions for the time period between 4-January and 11-January 2004. The boxes and time period selected are somewhat arbitrary and a similar result is obtained for other times and areas. The time series in Fig. 3.5 is an example of the benefit of having data at a 30 minute rather than four-times daily resolution, as the MODIS product misses many instances of sizeable variations in cloudiness between subsequent overpasses. For a large majority of the data points in these examples our cloud identification methodology produces a cloud fraction within 1-2% percent of the MODIS value at each overpass time. In a handful of instances during this time frame our product underestimates or overestimates cloud fraction by 10-20%. A closer look at the errors within the time series from the NE Pacific is given in Fig. 3.6. Here we show the merged-IR brightness temperature (top row) and cloud mask (middle row) along with the associated MODIS cloud mask (bottom row) for three different scenes from the time series in the NE Pacific. The MODIS pixels have been converted to binary cloud masks using the aforementioned 0.87 threshold. The left column of Fig. 3.6 shows an example in which cloud fraction within the blue box is 10% higher for the merged-IR product compared to the MODIS product. The overestimation appears to be due to misclassified cloud pixels within the broken cloudiness region in the middle right portion of the blue box. The middle column of Fig. 3.6 shows a scene in which the cloud fractions within the blue box matched perfectly while the right column shows an example of when the merged-IR cloud fraction is 10% too low compared to the MODIS value. In the underestimation example, it appears that the MODIS cloud mask identifies too much cloud in the center of the blue box.

We can accumulate statistics about the difference between the MODIS cloud fraction and our merged-IR product by doing a similar comparison for an extended period of time. Fig. 3.7 shows the probability (left column) and cumulative (right column) distributions of difference values for the time period 2003-2010 in multiple $3^\circ \times 3^\circ$ boxes spanning each of the stratocumulus regions. Here the boxes for each region span an east-west gradient along

the latitude of highest cloud fraction in each region. The goal of distributing the boxes in this way is to probe for a spatial bias in the cloud identification from the merged-IR data. Each of the error probability distributions in every region is roughly normally distributed with a large mode centered at 0%. The distributions are marginally positively skewed in both the NE Pacific and SE Atlantic, which means our product tends to slightly underestimate cloudiness in these regions. The merged-IR cloud fractions are within +/- 10% of the MODIS cloud fraction 65% of the time in the NE Pacific, 80% of the time in the SE Pacific, and 70% of the time in the SE Atlantic. Examples of what a +/- 10% error looks like are shown in Fig. 3.6. The area between the 16th and 84th percentiles, corresponding to +/- 1 standard deviation (σ) for a normal distribution, is between -7.3% and +23.4% error in cloud fraction in the NE Pacific, -7.9% and +5.9% in the SE Pacific, and -7.5% and +25.7% in the SE Atlantic. Because the lines for each of the 3° x 3° boxes in each region have the same shape and significantly overlap with each other, we conclude that there is no measureable spatial bias in the cloud identification methodology within a given region.

We can probe for other biases in the merged-IR cloud identification methodology by looking at error characteristics for different categories of environmental conditions. In Fig. 3.8, we show the frequency of differences between the MODIS and merged-IR cloud fractions conditioned on the MODIS cloud fraction. For any given MODIS cloud fraction (x-axis), the frequency of differences is tightly clustered around 0%. The mean difference (black line) for any observed MODIS cloud fraction is +/- 10%. This tells us that the merged-IR cloud fraction methodology performs well at the full range of observed cloud fractions. Finally, we can separate the difference distributions into categories from only the day (left column of Fig. 3.9) and night (right column of Fig. 3.9) MODIS overpasses. Consistent with the lack of bias for any given MODIS cloud fraction, there are no significant differences in the shape or skewness of the error distribution for day or night overpasses.

We further examine the possibility of spatial or relative cloudiness biases in our merged-IR product by aggregating the cloud maps from individual scenes into annual,

seasonal, and diurnal means and comparing against the MODIS product. The annual mean MODIS cloud fraction is shown in the left column of Fig. 3.10 for each of the subtropical stratocumulus regions. Here again we apply a 0.87 cloudiness threshold to each pixel before aggregating the individual MODIS swaths. The corresponding annual mean merged-IR cloud fraction is shown in the right column of Fig. 3.10. The merged-IR cloud fractions are taken only from the 30 minute merged-IR scene closest to the MODIS overpass. Comparing the datasets in this way demonstrates that our product captures the spatial structure and annual mean cloud fraction in the areas where the dominant cloud type is low cloud. Significant differences only occur in non-stratocumulus regions where our methodology was not designed to work – for example within the Intertropical Convergence Zone (ITCZ) in the NE Pacific region.

In addition to compositing the cloud masks on annual scales we can also examine the seasonal and diurnal mean cloud fractions in each region. We show the mean total MODIS and merged-IR cloud fraction for each season (June-July-August, September-October-November, December-January-February, and March-April-May) in all three regions in Figs. 3.11-3.13. We are again applying the 0.87 fractional cloudiness threshold to the MODIS data and masking out regions with high ice cloud frequency. The merged-IR product is able to capture variability in the seasonal amplitude of cloud fraction in each region as well as the significant changes to the shape and structure of the cloud deck for each season. The diurnal composites in Fig. 3.14 show similar frequencies of cloud during the day and night respectively compared to the MODIS product. As with the seasonal composites, the merged-IR cloud maps are able to replicate the changing shape of the cloud deck across the diurnal cycle.

3.3.3 Other Limitations

The annual mean cloud fraction plot also shows significant differences between the two products north of 25°N in the NE Pacific region. In the annual mean merged-IR cloud fraction image (top right panel of Fig. 3.10) there is a clear arc along the northern edge of the

stratocumulus field beyond which our cloud fraction values are noticeably lower than the MODIS values. Examining the underlying brightness temperatures in the merged-IR product in this region shows similar shaped arcs of brightness temperatures in the same location. One example of this is demonstrated within the teal box in Fig. 3.15. We believe these errors are associated with the zenith angle correction applied to account for erroneously cold values at high viewing angles. This correction is built into the base merged-IR brightness temperature product. The degradation of data quality in areas where the zenith angle correction is apparently not performing well leads to uncorrectable errors in our cloud identification algorithm and an erroneous estimation of cloud fraction in this region. For this reason data from this area are removed from our analysis. This area in the northern region of the NE Pacific stratocumulus deck is the only obvious example of bad data quality in any of the three regions examined.

3.2.4 Environmental Variables

We use multiple measures to characterize the state of the environment at different times in order to judge the impact of different physical processes on stratocumulus cloud fractions. The key processes/parameters described in the introduction will either be explicitly represented (ex: precipitation) or captured through a proxy variable (ex: representing boundary layer depth via cloud top pressure). The details of each dataset are provided in Table 3.2. Lower tropospheric stability (LTS; Klein and Hartmann 1993) is calculated using ERA-Interim reanalysis data from the European Centre for Medium-Range Weather Forecasts (ECMWF, 2009). Reanalysis data is available every 6 hours with a surface resolution of $0.7^\circ \times 0.7^\circ$.

$$LTS = \theta_{700} - \theta_{1000} \quad (3.1)$$

In addition to the reanalysis data, we use cloud top temperature and cloud top pressure – either of which can be used as proxy for boundary layer depth – from the MODIS MOD06_L2 cloud product. Cloud top temperature is available from the multispectral retrieval algorithm outlined by King et al. (2003). Data is available during both night and day at pixel-level resolution. Cloud droplet number concentration (CDNC), a proxy for aerosol

concentrations within the cloud layer, is calculated following Bennartz (2007). The CDNC algorithm uses estimates of cloud effective radius and optical thickness from the MODIS sensor. Because the estimation relies on measurements of cloud effective radius it is available only during the day. The CDNC retrieval is performed only when pixel scale cloud fraction and liquid water content are relatively high (80% and 30 g m^{-3} respectively). The algorithm yields cloud droplet number concentration with uncertainty less than 20%. Drizzle is identified using the empirical detection method of Miller and Yuter (2013). The drizzle detection algorithm uses 89-GHz passive microwave brightness temperature measurements. After screening out clouds with ice in them, drizzle is found by detecting local maxima in emission energy measured against a cloud-free background temperature and comparing them to empirically defined thresholds. This method can determine pixel scale occurrence of heavy drizzle, roughly equivalent to liquid water paths (LWP) larger than 200 g m^{-2} , over large areas and can be applied uniformly in all of the marine stratocumulus regions.

3.3 Results

3.3.1 Annual Mean Low Cloud Fraction

Examining the annual mean low cloud fraction from the merged-IR product (right column of Fig. 3.10), several similarities and differences are apparent among the regions. The SE Pacific has the highest annual mean low cloud fraction – both in the highest value for any pixel and in the area of high cloud fractions. Annual mean cloud fractions are similar in the NE Pacific and SE Atlantic (60% - 70%). The annual mean cloud fraction plots in Fig. 3.10 can also be used to examine the spatial structure of the stratocumulus cloud deck in each of the subtropical regions. In every region the maximum cloud fractions are located a short distance offshore of their respective continents to the east. This westward displacement is associated with coastal gradients in sea surface temperatures, relative humidity, and boundary layer depth (Neiburger et al. 1961; Wood and Bretherton 2004; Myers and Norris 2013). The distance offshore varies somewhat by region – from closest to shore in the SE Pacific to furthest offshore in the NE Pacific. In the SE Pacific, the stratocumulus deck

shows the well documented westward decrease in cloud fraction associated with deeper boundary layers further west of the South American continent (Wood and Bretherton 2004; Leon et al. 2008; Zuidema et al. 2009; de Szoeki et al. 2012). A similar but weaker relationship holds in the SE Atlantic, which has a westward decrease in cloud fraction as well as a sharp negative gradient along the southern (roughly 20°S) and northern (roughly 10°S) edges of the cloud field. The shape of the stratocumulus cloud deck in the NE Pacific shows very little relationship to the contours of the west coast of North America. The lack of shape to the stratocumulus deck in the NE Pacific may be related to the larger distance from shore (roughly 10° west and south) compared to the two southern hemisphere regions. In all regions the highest cloud fractions are located in the center of the cloud deck and cloud fraction decreases gradually toward the edges of the cloud deck.

3.3.2 Seasonal Cycles in Low Cloud Fraction

The seasonal mean low cloud fraction for each of the regions is shown in Fig. 3.16. In the NE Pacific (top row of Fig. 3.16), the highest stratocumulus cloud fractions occur during March-April-May and the lowest during September-October-November. The amplitude of the seasonal cycle is roughly 10-15%, a value that is in agreement with previous work by Wood (2012). Interestingly, the shape of the cloud deck is consistent among seasons as is the location of maximum cloudiness. The same cannot be said for the SE Pacific (middle row of Fig. 3.16) which shows significant seasonal variations in the structure and location of the stratocumulus cloud deck. The amplitude of the seasonal cycle is dependent on location but ranges from upwards of 50% along the Peruvian coastline to as little as 5% offshore of northern Chile. Closer to South America, cloud fraction peaks in June-July-August but is maximized in September-October-November further offshore. The biggest change in SE Pacific stratocumulus cloud fractions during the peak season (September-October-November) is a 10°-15° westward expansion of high cloud fractions which can be seen by comparing cloudiness between seasons along a given latitude (20°S for example). The largest seasonal variation in low cloud fraction of any of the three regions occurs in the SE Atlantic (bottom row of Fig. 3.16), where cloud fractions range from greater than 90% during the

peak season (September-October-November) to less than 40% during the minimum season (March-April-May). As in the SE Pacific, peak season spatial patterns in the SE Atlantic are most notable for the westward expansion of the cloud deck which spans out past 15°W in September-October-November. Stratocumulus clouds remain largely constrained between 10°S and 20°S during all seasons. The increased amplitude of the seasonal in the southern hemisphere regions is consistent with previous work and may be related to the close proximity to continents on the eastern edge of the stratocumulus cloud deck (Richter and Mechoso 2006; Wood 2012).

In the SE Pacific and SE Atlantic the spatial patterns associated with the seasonal cycle of low cloud fraction closely follows the variability and spatial structure of lower tropospheric stability (shown as contours in Fig. 3.16). This is consistent with previous work, notably Klein and Hartmann (1993; their Fig. 13), which showed the seasonal mean stratocumulus cloud fraction was linearly related to the mean seasonal stability for the region. Interestingly, the NE Pacific stratocumulus deck, which has the lowest amplitude seasonal cycle, only weakly follows the contours of LTS during any season. In Fig. 3.17, we recreate Fig. 13 from Klein and Hartmann (1993) using the merged-IR cloud identification method to get cloud fractions and ECMWF reanalysis to calculate stability. The best fit line utilizing our data (solid black line in Fig. 3.17) closely resembles the best fit line from Klein and Hartmann (dotted gray line in Fig. 3.17). The correlation between LTS and low cloud fraction in all regions combined is 0.86 using our data and was 0.88 in the Klein and Hartmann data (which included additional regions of stratocumulus clouds). As shown in Fig. 3.17, the NE Pacific (squares) regions has the weakest relationship between stability and low cloud fraction.

3.3.3 Interannual Variability in Low Cloud Fraction

The physical connection between stability, which is a combined function of sea surface and free tropospheric temperatures, and low cloud fraction also creates a pathway through which interannual variability in large scale circulations can manifest itself in

interannual variations of low cloud fraction. One obvious candidate for causes of perturbations on interannual time scales is the El Niño-Southern Oscillation (ENSO). ENSO, which has a well-documented impact on sea surface temperatures in the Pacific, varies on time scales of 3-7 years. Klein and Hartmann (1993) found a decrease in the annual mean low cloud fraction in the SE Pacific of about 5% per 1 K change in SSTs. The top panel of Fig. 3.18 shows the deviation of the monthly mean low cloud fraction from the mean annual cycle in the NE Pacific (blue line) and SE Pacific (green line) and the Niño 3.4 Index anomaly (black line; Trenberth 1997). The bottom panel of Fig. 3.18 shows the relationship between the Niño 3.4 Index anomaly and the deviation of lower tropospheric stability from the mean annual cycle. In the SE Pacific a positive ENSO index is associated with warmer SSTs (and correspondingly a lower stability). This should in turn result in depression of low cloud fraction compared to the mean value (Klein and Hartmann 1993). The time series shows that this relationship does hold for some time frames (mid-2003 through 2007), but is out of phase for others (2007 through 2010). A stronger relationship holds in the NE Pacific where, with the exception of the year between mid-2006 and mid-2007, a positive value of the Niño 3.4 Index anomaly is associated with a decrease in low cloud fraction and a negative Niño 3.4 Index anomaly is associated with a decrease in low cloud fraction. These time series show that ENSO can impact low cloud fraction in the subtropical stratocumulus regions via a modification of SST and stability, but that the relationship is not perfect and other sources of variability occasionally decrease the strength of the relationship. This is consistent with a recent study from Myers and Norris (2013), which showed that the connection between stability and cloud fraction on interannual time scales can be overwhelmed by other influences.

3.3.4 Diurnal Cycles in Low Cloud Fraction

3.3.4.1 Areal Patterns

The mean low cloud fraction over all seasons at night (6:00 pm to 6:00 am; the two left columns) and during the day (6:00 am – 6:00 pm; the two right columns) is shown for all

regions in Fig. 3.15. As expected, all of the subtropical stratocumulus regions show a significant decrease in cloudiness during the day. Previous work has shown that, at a given location, this decrease in cloud fraction is associated with a daytime reduction in subcloud turbulent mixing which supplies moisture to the cloud (Turton and Nicholls 1987; Betts 1990; Burleyson et al. 2013). Mean low cloud fraction in all regions is roughly 15-20% lower during the day compared to overnight. The largest decrease in cloudiness occurs on the edges of the cloud field. An example of the mean diurnal transition in cloudiness is shown in Fig. 3.19. Here we show the hourly mean cloud fraction measured during the season of minimum cloudiness. These transitions are best viewed as a movie (and will be included as an electronic supplement in the paper), but are shown here as static images. The corresponding images for peak and minimum season diurnal cycles in all three regions are given in Appendix A. The maps shown in Fig. 3.19 are a representative example of the variability at other times and in other regions.

The images in Fig. 3.19 show that the mean diurnal cycle evolves in a very structured way. Total cloud fraction for the region is maximized between 5:00-7:00 am (roughly sunrise) and reaches a diurnal minimum between 3:00-5:00 pm. In between the peak and minimum times cloudiness gradually decreases from the edges of the cloud field toward the center. Regions of low cloud fraction on the edge of the cloud deck break up earlier than regions of higher cloud fraction closer to the center. Cloud fractions at the center of the cloud deck remain above 60% throughout the day. After 3:00-5:00 pm, cloud fraction gradually increases in time back to its diurnal peak value just before sunrise. Cloudiness increases slowest in the regions of low cloud fraction on the edge of the cloud deck.

The patterns evident in the spatial structure of the mean diurnal cycle indicate that cloud decrease is more likely and occurs earlier in the day in regions of low cloudiness. This is consistent with previous studies (Rozendaal et al. 1995; Klein et al. 1995). This could result from a positive feedback whereby regions of low cloud fraction create conditions more favorable to cloud break up. One possible cause of a positive feedback is closely linked to the

diurnal transition in subcloud turbulence. The radiative cooling at cloud top is strongly dependent on the liquid water content and thus, for a given region, also proportional to cloud fraction (Nicholls and Turton 1986). Having clouds present creates a source of longwave cooling and the potential to create negatively buoyant parcels that act to mix the boundary layer. Since cloud fraction is closely tied to the supply of moisture to the cloud deck via turbulent mixing, lower cloud fraction regions that produce weaker or more intermittent turbulent overturning can more easily be disconnected from their moisture source. The opposite would be true in the high cloud fraction region at the center of the cloud deck where negatively buoyant parcels are produced at a higher rate and turbulent coupling persists for a larger part of the day. Under this positive feedback, low cloud fraction regions would experience cloud breakup earlier in the day as less shortwave heating would be required to offset longwave cooling at cloud top.

3.3.4.2 Rates of Change

The unique benefit of having a cloud identification methodology that works at 30 minute resolution is the ability to look at higher frequency (time scales of a few hours) changes to the cloud deck. The dataset allows us to examine facets of the diurnal cycle that have previously gone unresolved with lower temporal resolution datasets. In Fig. 3.20 we show the distribution of low cloud fraction across the diurnal cycle during the peak (left column) and minimum (right column) cloudiness season for each region. The goal of looking at the peak and minimum season separately is to remove one source of variability – the annual cycle – from our analysis of the diurnal cycle. Additionally, we calculate the rate of change between subsequent scenes and plot the distribution of those rates Fig. 3.21. The low cloud fraction time series used in these plots are calculated over all of the $3^\circ \times 3^\circ$ boxes shown in the right column of Fig. 3.10.

Starting in the peak season in the NE Pacific (top left panel of Fig. 3.20), the mean low cloud fraction decreases during the day from its peak value just over 70% at sunrise to a diurnal minimum of 55% around 3:00 pm. Mean cloudiness increases after 3:00 pm until it

reaches its nocturnal steady state value in the early morning hours. Looking at the distribution of the rate of change of low cloud fraction in Fig. 3.21, the breakup of the cloud field (shown as negative rates of change) can be seen as early as 6:00 am in the mean value. This is consistent with the idea that it takes very little solar heating to offset longwave cooling and induce decoupling in the subcloud layer (Duynkerke 1989). By 8:00 am low cloud fraction in the NE Pacific is decreasing more than 90% of the time. The maximum rate of decreasing cloudiness, roughly $4\% \text{ hr}^{-1}$ in the peak season, occurs between 9:00 am and 12:00 pm, after which cloud fractions are still most often decreasing but at a slower rate. Between 6:00 pm and midnight low cloud fraction is decreasing only 10% of the time. Comparing and contrasting the variations of cloudiness during the peak (left column) and minimum (right column) seasons of cloudiness shows that the same general patterns persist no matter the season. Despite lower cloud fractions (the mean is roughly 10% lower while the mode decreases by as much as 20%) compared to the peak season, the rates of change of cloudiness are similar between seasons.

Diurnal distributions of cloud fraction for the SE Pacific are shown in the middle row of Fig. 3.20. Consistent with Fig. 3.16, peak season cloud fractions are higher than in the NE Pacific. The overnight mean and mode are both greater than 90% and the mean cloud fraction during the afternoon stays above 70%. The width of the cloud fraction distribution is also smaller than in the NE Pacific. Cloud fractions less than 70% are rarely observed overnight during the peak season. As in the NE Pacific, the mean and mode cloud fraction begin to decrease shortly after sunrise. A much larger diurnal cycle of cloudiness is observed during the minimum season compared to the peak cloudiness season in the SE Pacific. Overnight mean and modal cloud fractions are greater than 70%, but the cloud deck during the minimum season routinely breaks up to less than 50% coverage during the afternoon. These combined features require much higher rates of increasing and decreasing cloudiness – a fact that is reflected in the distributions in Fig. 3.21. On average, cloud fraction decreases by $6\% \text{ hr}^{-1}$ between 10:00 am and noon and increases by $4\% \text{ hr}^{-1}$ between 7:00 pm and midnight. Both of these represent the highest mean values measured during any region or season.

Like in the SE Pacific, a very small diurnal cycle occurs during the peak season of cloudiness in the SE Atlantic (bottom row of Fig. 3.20). During the peak season the mode of the cloud fraction distribution varies by less than 15% across the diurnal cycle. Consistent with the patterns in Fig. 3.16, the differences in the cloud fraction distribution between the peak and minimum seasons in the SE Atlantic is the largest of any of the regions. In the minimum season the highest mode of cloud fraction tops out at just above 60% in the early morning hours and there are very few instances of cloud fraction greater than 70%. Mean cloud fraction drops below 40% during the afternoon.

The diurnal evolution of total cloud fraction in the subtropical stratocumulus regions unfolds in a fairly regular and predictable manner. Subtle differences in the patterns are observed amongst the regions or seasons, but on the whole the direction and magnitudes of the change are similar. Consistent with previous work (Turton and Nicholls 1987; Klein et al. 1995; Rozendaal et al. 1995; etc.), the diurnal minimum in cloud fraction occurs near 3:00 pm. One interesting pattern present in all three regions is that the maximum rate at which the cloud deck breaks up occurs just before or at local solar noon. This corresponds to the time when shortwave radiative flux is also maximized. After noon but before 3:00 pm the cloud generally continues to break up but at a slower rate. This suggests that the rate which the cloud deck as whole breaks up is strongly tied to shortwave radiative flux. The diurnal variability in turbulent mixing is driven by variations in the net cloud top radiative flux (longwave cooling + shortwave heating; Nicholls 1984). Variations in longwave cooling during the day can come from changes in cloud fraction, cloud thickness, or cloud top height. That cloud break up maximizes with the maximum shortwave flux implies that the rate of change of cloud fraction is mostly driven by changes in the incoming shortwave heating rather than variations in longwave cooling. Evidence for this can be seen in the rate at which cloud fraction increases during the afternoon (after 3:00 pm) compared to after sunset. Between 3:00 pm and sunset the rate at which cloud fraction increases accelerates (becomes faster) in time. By contrast, between sunset and midnight, or when the cloud fraction closes in on 100% thus limiting the potential for further increases, the rate at which cloud fraction

increases in time is largely constant in all regions and seasons. Because of these relationships it is apparent that the rate at which the stratocumulus cloud deck as a whole increases or decreases in time is strongly dependent on the magnitude of the shortwave radiative flux.

3.3.4.3 *Net Changes*

Another interesting component of Fig. 3.21 is the near complete lack of data points showing decreasing cloudiness overnight or increases in cloudiness during the day. In all regions and seasons negative rates of change between 6:00 pm and midnight occur less than 10% of the time. Decreasing cloudiness occurs slightly more often between midnight and 6:00 am, but the rate of decrease is much smaller than that observed during the day. We explore these patterns in more detail in Figs. 3.22-3.24 where we show the frequency distribution of the three hour change in cloud fraction (y-axis) conditioned on the starting cloud fraction at a particular time (x-axis). In contrast to Fig. 3.20, the data shown here are the distributions of individual values calculated for each $3^\circ \times 3^\circ$ box rather than the total cloud fraction over all boxes combined. The data are not separated by season. The patterns shown in these plots are generally consistent among regions so the discussion of these patterns applies to all three regions unless otherwise stated.

In the three hour window beginning at sunrise (top left panel of Figs. 3.22-3.24), the mean (dotted line) and mode (darkest color) change in cloudiness is negative in all regions. The greatest negative change occurs when cloud cover at dawn is broken (between 25% and 75%). When the cloud cover approaches 100% at dawn the decrease in the early morning hours is smaller than when there is broken cloud. A similar pattern is seen in the next two windows between 9:00 am and noon and between noon and 3:00 pm. Consistent with the results shown in Fig. 3.20, the mean change in cloud fraction becomes positive in the window between 3:00 pm and 6:00 pm (top right panel of Figs. 3.22-3.24). In the three hours after sunset low cloud fraction in all regions is rapidly increasing in time. In the remainder of the overnight windows (bottom row) cloud fraction is increasing in time for all values of

starting cloud fraction. The only exception is for the highest starting cloud fractions (right edge of x-axis), where the cap of cloud fraction at 100% limits the possibility for increases.

The gross patterns shown in Figs. 3.22-3.24 are consistent with the results shown in Fig. 3.20 and with previous work (Turton and Nicholls 1987; Klein et al. 1995; Rozendaal et al. 1995). The benefit of analyzing the data in this way is that it provides more evidence for the repeatability of cloud fraction changes during the day and at night. In any given daytime window, cloud fractions are increasing in time in just over 10% of the boxes and times observed. This can be seen by looking at the top solid line – which indicates the 90th percentile of the distribution – and its relationship to the 0% change line. Overnight around 10% of the boxes have cloud fractions that decrease in time. When cloud fraction does decrease overnight it does so only marginally – most often much less than 20% in any three hour window. These patterns are particularly evident in the SE Pacific and SE Atlantic regions.

We can examine at the net result of cloudiness changes during the day by looking at the cloud fraction in a given 3° x 3° box at sunset compared to the cloudiness in that box at sunrise (Fig. 3.25). Similarly, the total changes overnight can be seen by looking at the cloud fraction at dawn as a function of the cloud fraction at sunset (Fig. 3.26). Cloud fractions at dawn are the average cloud fraction from 5:00 am to 6:00 am while cloud fractions at dusk are the average cloud fraction between 5:00 pm and 6:00 pm. The interpretation in each of these plots is that given some starting position on the x-axis, what is the probability of observing a given cloud fraction twelve hours later (y-axis)? Starting in Fig. 3.25, for all cloud fractions at dawn greater than 20-30% (depending on which region you examine) the mean cloud fraction at dusk is always lower. All three regions show a resistance to change on the extreme ends of the x-axis. When cloud fraction at dawn is low (say less than 30%) it is very likely to remain low throughout the day. For cloud fractions at dawn greater than 90%, the mode of cloud fraction at dusk is also greater than 90%. Strong signals of increasing cloudiness overnight are seen in Fig. 3.26. For all possible cloud fractions at dusk the mean

value by the following dawn is always higher. The greatest gain in the mean cloud fraction is associated with lower starting cloud fractions, which can increase by as much as 40% overnight. The mode (darkest color) of the distribution shows that cloudiness frequently increases all the way to 100% when cloud fraction at dusk is greater than 20%.

The distribution of cloud fraction changes overnight shown in Fig. 3.26 also strongly reflects the low probability of observing net decreases in cloud fraction overnight. In the SE Pacific and SE Atlantic the lower black line (which indicates the 10th percentile of the cloud fraction at dawn distribution), hugs tightly to the silver line which diagonally transects the figure. This means that roughly 10% of the time series observed showed a decrease in cloudiness overnight. This value is slightly larger for high starting cloud fractions in all three regions and for all cloud fractions at dusk in the NE Pacific. To help with interpretation, we show the frequency of positive and negative changes overnight conditioned on the cloud fraction at dusk in Fig. 3.27. The blue line shows the frequency of any negative change overnight. As in Fig. 3.26, the frequency of negative changes overnight is between 10-20% for all starting cloud fractions less than 80% in the SE Pacific and SE Atlantic. Slightly higher frequencies are observed in the NE Pacific. This figure also shows the frequency of cloudiness decreases greater than 10% (cyan line) and greater than 20% (green line). Cloud fraction decreases overnight larger than 10% occur less than 10% of the time in the SE Pacific and SE Atlantic and less than 15% of the time in the NE Pacific. One final way of visualizing these changes is shown in Fig. 3.28 where we show the probability (top panel) distribution and cumulative (bottom panel) distribution of cloud changes overnight for the NE Pacific (blue lines), SE Pacific (green lines), and SE Atlantic (red lines).

The data shows that cloud fraction is very unlikely to decrease overnight and when cloud fraction does decrease overnight those changes are most often small. We find no evidence that large scale clearing of cloudiness within a given 3° x 3° area is routinely occurring. Within the SE Pacific and SE Atlantic, over 8 years of data using all of the time series in 28 boxes, a total sample size greater than 55,000 data points in each region, cloud

fractions decrease more than 30% from their starting value at sunset only 2% of the time. To account for cases where cloud fraction has a net increase overnight but shows a large decrease before the sun comes up we can look at $3^\circ \times 3^\circ$ boxes where cloud fraction goes above 90% at any point during the night but is broken at sunrise. Of all boxes in which cloud fraction at any point during the night goes about 90% (more than 37,000 cases each in the SE Pacific and SE Atlantic), these regions end up with a cloud fraction lower than 60% at sunrise between 1-2% of the time. Measuring the changes in cloud fraction overnight is a way to gauge the relative importance of boundary layer mixing, precipitation, and boundary layer depth. The distribution of net overnight cloud fraction changes suggests that the increase in turbulent mixing overnight overwhelms the negative tendencies from increased precipitation and deeper boundary layers a vast majority of the time.

This is a significant result because it puts into context the relative role of POCs in modifying stratocumulus cloud fractions. Here we are using the term POCs to describe an event where the environment transitions from a high cloud fraction into a relatively lower cloud fraction. We make no attempt to actually classify the mesoscale organization within the observed cloud field. We use the overnight change in cloud fraction as a proxy for POC formation. Examining individual cases where cloud fraction decreases significantly overnight, we can find clear examples where POCs are forming. There are also many examples where POCs that had already formed advected into a neighboring $3^\circ \times 3^\circ$ box. Many of the cases are also transitions that are not related to POCs. These include regions where the edge of the cloud deck moves over a given region overnight or frontal clearing of the cloud deck which leads to a large decrease overnight. So of all the data points where cloudiness decreases overnight, POCs are only a component. Classifying every time series where cloud fraction decreases overnight as a POC thus *overestimates* the frequency of POCs. The vast majority (>80%) of POCs are thought to form overnight (Wood et al. 2008; their Fig. 10). In the two case studies presented in their paper, Wood et al. describe scenarios where cloud fractions decrease from nearly overcast (100%) to less than 60%. Analysis of our merged-IR cloud fraction time series shows that such transitions rarely occur.

The overwhelming tendency for cloud fraction to increase and remain high overnight means that POCs likely represent outlier behavior in the cloud-topped boundary layer system.

POCs have generated interest within the community because overnight changes from high cloud fraction closed cellular organizations to low cloud fraction open cellular organizations could go on to impact the net radiation reaching the surface during the day. So the question remains, even though POCs appear to be occurring relatively infrequently, could they have a sizeable impact on the net radiative budget via their impact on cloudiness the following day. Analysis of the daytime changes in cloud fractions shows a strong tendency for cloudiness to decrease during the day. Because of this, regions in which cloud fraction decreases overnight are likely to maintain a reduced cloudiness state during the day (Fig. 3.25). We can use the time series of merged-IR cloud fractions to analyze this by looking at cloud fraction distributions at later points during the day conditioned on the cloud fraction value at dawn (Fig. 3.29). What this figure shows is that, given the relatively constrained rates of change during the day, the largest determining factor in cloud fraction at any given point during the day is the value of cloud fraction at dawn. Regions with lower starting cloud fraction will allow more radiation to reach the surface during the day. However, Fig. 3.26 shows that broken clouds at dawn are much more likely the result of a scenario where cloud fractions were increasing overnight but did not become completely overcast. For example, for a starting cloud fraction at sunset of 30%, the mean cloud fraction by the following dawn is less than 70% for all three regions. Scenarios in which cloud fractions decrease overnight from 100% at sunset to 70% at sunrise rarely occur. Thus low cloud fractions at dawn are most likely a result of cases in which cloudiness was increasing overnight but did not reach overcast conditions.

Fig. 3.25 shows the overall trend of decreasing cloudiness during the day no matter the starting cloud fraction. The impact of POC-like transitions in cloudiness overnight can be put into context relative to the magnitude to these normal daytime decreases. In Fig. 3.30, we show the distribution of cloud fraction at dusk compared to the maximum value at any point

during the day (top panel) and the distribution of cloud fraction at dawn compared to the maximum value at any point overnight (bottom panel). The goal of measuring these distributions is to judge the relative areas of decreasing cloudiness during the day compared to the night. The daytime distribution (top panel) shows frequent decreases of cloudiness greater than 30%. The mean value in all regions is between 20-35%. This means on an average day, cloud fraction by sunset is roughly 30% lower than its maximum value at any point during the day. By contrast, the maximum decrease ever observed overnight is 30% in the NE Pacific and roughly 15% in the SE Pacific and SE Atlantic. On average, cloud fractions at sunrise are only a few percent lower than their maximum value overnight and the vast majority of cloud fractions at sunrise are equal to their maximum value overnight. The data shows that the maximum decrease in net cloudiness overnight ever observed is equal to the mean daytime decrease that occurs on any given day. This, combined with the relative infrequency of POC-like cloudiness transitions overnight, strongly suggests that models that fail to capture diurnal patterns in cloud fraction (for example – Wyant et al. 2010; their Fig. 11) are more likely to be missing the basic radiatively forced diurnal variability in turbulent mixing and its relationship to cloudiness rather than outlier behavior like POC formation.

3.3.5 Environmental Characteristics When Cloud Fraction Decreases Overnight

To shed some light on what may be causing the rare cases of cloud fraction decreases overnight we can examine the environmental conditions present when these cases occur. In this analysis we use the environmental data described in section 3.2.4. In the case of using MODIS data, we use the nighttime overpass (~1:30 am) that covers the $3^\circ \times 3^\circ$ box where the decrease occurs. While using a single swath that samples the environment for a brief moment in the middle of the night might not capture the full variability present in the environment, it can give a general idea about the state of the environment.

The spatial structure of the probability of observing a decrease in cloudiness overnight could reflect the underlying cause. All three subtropical stratocumulus regions have significant spatial variability in precipitation, boundary layer depth, aerosol

concentrations, and stability. Most of these vary longitudinally with increasing precipitation and boundary layer depth and decreasing aerosol concentrations and stability further from the coast (Wood and Bretherton 2004; Leon et al. 2008; Zuidema et al. 2009; de Szoeki et al. 2012; etc.). We show the spatial structure of the probability of observing a decrease in cloudiness overnight in Fig. 3.31. Within a given region there are only weak spatial gradients. In all three regions the probability of decreasing cloudiness is slightly higher along the edges of the cloud field compared to the interior. Given that cloud fraction gradually decreases from peak values in the center of the cloud deck to lower values along the edges (Fig. 3.10), this means that lower cloud fraction regions on the edges of the cloud deck are slightly more likely to observe a net decrease overnight. Also evident in this figure is the higher probabilities of observing a net decrease in the NE Pacific compared to the two southern hemisphere regions. This is consistent with Fig. 3.28.

We show the annual variability of overnight decreases in the top rows of Figs. 3.32-3.34. In the SE Pacific the highest frequency of overnight decreases occurs during June-July-August, where a net decrease occurs between 20-25% of the time. Most of these net decreases are quite small. The probability of observing a large decrease (more than 20%) is less than 5% at any point during the year. Data from the SE Atlantic also show an annual cycle with a broader peak that spans from April through September. The annual cycle of decreasing cloud fraction overnight in the SE Pacific and SE Atlantic indicates that a net overall decrease is most likely to occur during the peak season of cloudiness within each region. This is consistent with Fig. 3.27, which shows that net decreases occur more frequently when the cloud fractions at dusk are greater than 80%. Overnight decreases in these scenarios are most often small changes (-10 to -20%; Fig. 3.25).

We show the distribution of environmental characteristics during periods in which cloud fraction decreases overnight in the bottom rows of Figs. 3.32-3.34. Starting with precipitation (bottom left plots), the distribution of the area fraction of heavy drizzle is virtually identical for time series in which cloud fraction increases, decreases, and decreases

significantly overnight. One thing to point out in this figure is the high probability of observing little to no drizzle even in areas where cloud fraction decreases overnight. This result is significant with regards to the VOCALS hypothesis H1b: “Precipitation is a necessary condition for the formation and maintenance of pockets of open cells (POCs) within stratocumulus clouds (Wood et al. 2011a)”. The combined merged-IR cloud fraction and drizzle frequency datasets indicate that drizzle is not a necessary condition for large decreases in cloud fraction on $3^\circ \times 3^\circ$ scales.

In contrast with drizzle area, the cloud top temperature in regions where cloud fraction decreases more than 10-20% overnight has a distinctly different distribution than regions where cloudiness increases. Cloud tops are generally lower (higher temperature) in regions of significant overnight decreases. Lower cloud top heights overnight could be found in regions of cooler boundary layers or stronger subsidence. A more likely explanation is that the lower cloud tops result from reduced turbulence in the boundary layer. Cloud tops increase in height overnight via entrainment deepening (Nicholls 1984; Bretherton and Wyant 1997; Lewellen and Lewellen 1998; etc.). Strong turbulent overturning that results from net radiative cooling at cloud top creates turbulent eddies that impinge upon the inversion at cloud top. These eddies lead to the entrainment of warmer air from the free troposphere and the eventual deepening of the boundary layer. Higher cloud top temperatures during times when cloud fraction decreases overnight could be a sign of weaker turbulence that simultaneously prevents the boundary layer from deepening overnight and reduces cloud fraction. In this way lower cloud tops could be a symptom rather than a cause of reduced cloudiness overnight.

3.3.6 Environmental Sensitivity Tests

The net distributions of environmental conditions for different scenarios of increasing or decreasing cloudiness overnight indicated that cloud top temperature might be a useful discriminator for identifying regions likely to experience a POC-like decrease in cloudiness. There is value in looking at these distributions, but doing so does not fully leverage the

benefit of having a cloud map available every 30 minutes. To take advantage of the high temporal resolution data we performed an additional set of analyses in which we used the environmental conditions measured during the MODIS overpass as an “initial condition” and then tracked the cloud fraction evolution in the subsequent hours. This is a unique way to examine the sensitivity of cloud fraction to changes in each of the environmental parameters we are interested in.

In Figs. 3.35-3.40 we show the distribution of cloud fraction change in a period of a few hours after the MODIS overpass conditioned on the value of drizzle area, cloud top temperature, and lower tropospheric stability. Cloud fraction and the environmental variables were measured in the $3^\circ \times 3^\circ$ boxes shown in Fig. 3.10. We classified the environmental variables measured at the time of the MODIS overpass into ten different percentile bins based on their distribution over all eight years of data. For example, if a cloud top temperature of 280 K is measured within a given box we would classify that value into a percentile of cloud top temperature by comparing the value of 280 K to the full range of cloud top temperatures measured within that box during all 1:300 am MODIS overpasses from 2003-2010. Analyzing the data in this way allows us to see the evolution of the cloud field in times where cloud top temperature, for example, is relatively high or low for a given region. Cloud fraction is tracked for a period of one, three, and five hours after the overpass. After five hours (~6:00 am) the sun comes up and the system is modified by shortwave heating and the sensitivity to initial conditions measured at ~1:30 am loses value. Since some of the sensitivities are subtle, we also show the data density diagrams with the total distribution of cloud fraction change from all times subtracted out. This shows the deviation from the baseline distributions for a given set of initial conditions.

In all of the panels in Figs. 3.35, 3.37, and 3.39 the distribution of cloud fraction changes after one, three, and five hours are tightly clustered around 0% with the mode of each distribution being slightly positive. Physically, this means that cloud fraction in these regions is most likely to be changing very little between 1:30 am and sunrise. This is

consistent with Fig. 3.21 and reflects the fact that by 1:30 am cloud fraction in a large subset of the data has increased to near 100%, thus limiting the possibility of further positive increases. The distribution of cloudiness changes five hours after the MODIS overpass is more diffuse than one hour but is still slightly positive.

Subtle changes in the distribution of cloudiness changes can be seen in Figs. 3.35, 3.37, and 3.39, but these changes are made more apparent by subtracting out the total distribution of cloud fraction changes for all times (Figs. 3.36, 3.38, and 3.40). The sensitivity to drizzle area is shown in the top panel of Figs. 3.36, 3.38, and 3.40. Data from all three regions show that at lower percentile drizzle areas there is a slightly increased probability of observing cloudiness decreases within the next five hours. This signal is stronger one hour after the MODIS overpass compared to three or five hours. At higher percentile drizzle areas there is actually a decrease in the probability of negative cloud fraction changes and a slight increase in the frequency of weakly positive or neutral cloudiness changes. These patterns are contrary to what would be expected if drizzle were routinely associated with the break-up of clouds. The drizzle sensitivity plots seem to indicate that cloud fractions must remain high in order to maintain high drizzle areas. This result, added to the evidence that there was little drizzle observed in times of decreasing cloudiness overnight, further serves to cast doubt on the claim that drizzle is a necessary condition for POC-like cloud break up. Cloud fraction sensitivity to stability is shown in the bottom rows of Figs. 3.36, 3.38, and 3.40. The dominant signal is a slight increase in the frequency of decreasing cloudiness for low stability values and a slight decrease in the frequency of decreasing cloudiness for high stability values. This signal is weaker compared to the drizzle sensitivity plots and the exact nature of the sensitivity varies by region.

Cloud fraction appears to be more sensitive to changes in the value of cloud top temperature than to changes in either drizzle area or stability. This is consistent with the fact that distributions of cloud top temperature are different in scenarios where cloud fraction increases, decreases, and decreases significantly overnight. In all three regions, the lowest

percentiles of cloud top temperature (corresponding to relatively shallow clouds), are associated with a sizeable increase in the frequency of cloud fraction decreases. Similarly, for environments where cloud top temperature corresponds to a high percentile (relatively deeper clouds) there is a decrease in the frequency of cloudiness decreases and a slight increase in the frequency of neutral events. As with drizzle area and stability, the strength of these relationships weakens over time. In the SE Pacific, there is a slight increase in the frequency of cloud fraction increases from one to three hours after the MODIS overpass for shallow clouds (low cloud top temperature percentiles). Combined with more common cloud fraction decreases for the same conditions, this would indicate that cloud fraction is more variable in cases where cloud tops are anomalously low. The environmental sensitivity tests in the NE Pacific have no strong signals associated with any of the variables.

3.4 Discussion

The results presented in this chapter point to a system in which cloud fraction varies in a fairly regular manner on seasonal and diurnal time scales. To put the seasonal and diurnal cycles into context, we use a multivariate polynomial regression to create a simple model of cloud fraction that depends only on the time of day (diurnal cycle) and the day of year (seasonal cycle). By creating a separate model for each $3^\circ \times 3^\circ$ box there is an implicit dependence on location as well. We use this simple model to predict the cloud fraction at 30 minute intervals in all of the boxes in each of the subtropical stratocumulus regions. The empirical model used time of day (X_1 ; rounded to the nearest hour) and day of year (X_2 ; rounded to the nearest 10 days) as independent variables and the merged-IR cloud fractions (Y) as the dependent variable. We used Matlab's "polyfitn" function, which is based on the least-squares regression technique, to calculate the coefficients (B_i) for each parameter and "polyvaln" to evaluate the model and create the time series of predicted cloud fractions. The regression model used a 3rd order polynomial which was sufficient to capture the sine-wave-like curves of the diurnal and seasonal cycles. We tested models up to a 5th order polynomial

but the added complexity only marginally improved the fit. The general form of the third order polynomial regression is:

$$\begin{aligned}
 Y = & B_0 + B_1X_1 + B_2X_2 + B_3X_1^2 + B_4X_2^2 + B_5X_1X_2 + B_6X_1^3 \\
 & + B_7X_2^3 + B_8X_1^2X_2 + B_9X_1X_2^2 + Error
 \end{aligned}
 \tag{3.2}$$

The distributions of the difference between the predicted cloud fraction and the measured merged-IR cloud fraction for every 30 minute time period from 2003-2010 are shown in Fig. 3.41. The errors vary somewhat by region, with the smallest net error occurring in the SE Pacific and the largest in the NE Pacific. The total variance explained by the simple model, built only from the time of day and the day of the year, is equal to the squared correlation coefficient between predicted and measured cloud fraction time series (Fig. 3.42). In some portions of the SE Pacific and SE Atlantic the model explains up to 50% of the total variance in cloud fraction on 30 minute time scales. Naturally, the most variance is explained in regions with large seasonal or diurnal cycles in cloud fraction. This means that less variance is explained in locations where the seasonal cycle is small (most of the NE Pacific and off the coast of northern Chile in the SE Pacific; Fig. 3.16) or the diurnal cycle is small (high cloud fraction regions which have a smaller amplitude diurnal cycle; see Fig. 3.19 for an example). The most variance is explained in the SE Atlantic which has the largest seasonal cycle of low cloud fraction (Fig. 3.16). When looking on longer time scales, for example the monthly mean cloud fraction, up to 90% of the total variance is explained by the seasonal and diurnal cycles (Table 3.3).

Numerical models are sometimes evaluated against observations to examine their ability to produce accurate diurnal cycles of cloud fraction (ex. Abel et al. 2010; Wyant et al. 2010; Medeiros et al. 2012). In Fig. 11b of Wyant et al. (2010; shown here in the left panel of Fig. 3.42), the authors compare observations of the diurnal cycle of cloud fraction to values calculated by various GCMs. The cloud fraction observations (solid black line) in their plot are from a climatology by Ghate et al. (2009), who calculated cloud fraction using a point

measurement of longwave radiative flux from a radiometer stationed on an oceanographic buoy located at 85°W and 20°S. Model cloud fractions (colored and dotted lines) were calculated in a 1° x 1° box centered on the buoy. Wyant et al. use this comparison to show that very few GCMs come close to producing cloud fractions near observed values at any point in the diurnal cycle. We can evaluate our simple empirical model by replicating their comparison. In the right panel of Fig. 3.43, we show the same baseline climatology of cloud fraction (black line) calculated from the merged-IR cloud dataset. The cloud fractions are calculated over the same 1° x 1° box used by the models. The box, centered at 85°W and 20°S, is in a region where roughly 20% of the total variance on 30 minute time scales is explained by the seasonal and diurnal cycle. In addition to the base diurnal cycle observations, we show the mean cloud fraction predicted using our empirical model. The simple prediction system more closely resembles the mean diurnal cycle from observations (the black line in either panel) than any of the fully-coupled GCMs. The close resemblance between the empirical model and the observations shows that seasonal and diurnal cycles go a long way toward capturing the dominant behavior of the cloud-topped boundary layer system.

Comparing the NE Pacific plots to those in the southern hemisphere in Fig. 3.42, we see that diurnal and seasonal cycles explain a smaller portion of the total variance in the NE Pacific. This result is consistent with the patterns observed in the rest of this chapter. Stratocumulus clouds in the NE Pacific have the smallest seasonal cycle (Fig. 3.16), the widest distribution of cloud fraction across the diurnal cycle (Fig. 3.20), and the largest number of examples where cloud fraction decreases overnight (Fig. 3.27). However, the subtropical stratocumulus region in the NE Pacific has similar annual mean values of LTS and estimated inversion strength (Wood and Bretherton 2006) and shows the same relationship between stability and cloud fraction and between boundary layer depth and cloud fraction as the SE Pacific (Wood and Hartmann 2006).

So why do stratocumulus-topped boundary layers in the NE Pacific behave so differently? One major difference between stratocumulus in the NE Pacific and those in the SE Pacific is the latitude at which they form (Klein and Hartmann 1993; Wood and Hartmann 2006; Wood 2012). The stratocumulus cloud deck in the NE Pacific forms closer to the northern hemisphere storm track than the two southern hemisphere stratocumulus regions. The northern and southern hemisphere storm tracks as well as the ITCZ show up as increased variability in the plot of seasonal standard deviations of the 700 hPa vertical velocity from the ECMWF reanalysis (Fig. 3.44). In the NE Pacific the stratocumulus cloud deck is within 10° latitude of either of the northern hemisphere storm track (December-January-February or March-April-May) or the ITCZ (June-July-August or September-October-November) in all seasons. By contrast, the southern hemisphere storm track remains more than 10° latitude south of the stratocumulus deck in the SE Pacific and SE Atlantic in all seasons. The ITCZ never approaches the cloud decks in the southern hemisphere.

Our results are consistent with previous investigators and we concur with them that increased synoptic variability in the NE Pacific caused by proximity to the ITCZ and the northern hemisphere storm track results in larger deviations from the base seasonal and diurnal cycles. Previous work has shown that synoptic variability in the subtropics can lead to variations in stability (George and Wood 2010), boundary layer depth (Toniazzi et al. 2011) and the formation of POCs (Allen et al. 2012). The interaction can take the form of cold air advection, fronts crossing through the region or mesoscale disturbances such as gravity waves generated by synoptic systems. Anecdotally, examining a few days' worth of cloud fraction movies at a time you can find many examples of frontal boundaries moving through the NE Pacific cloud deck. Also associated with these features is a much higher occurrence of ice clouds in the NE Pacific compared to the SE Pacific or SE Atlantic (left column of Fig. 3.10). Ice clouds forming on top of the stratocumulus cloud deck would modify the radiative balance at cloud top by trapping or reflecting much of the outgoing longwave radiation. This could lead to scenarios in which the generation of the negatively buoyant parcels at cloud top that act to mix the subcloud layer is diminished overnight.

Further examination of the interaction between synoptic processes and stratocumulus in all regions is required before any decisive conclusions can be made.

3.5 Conclusions

Patterns of cloud fraction variability in each of the three subtropical marine stratocumulus regions are documented using a new cloud identification dataset. We developed for marine regions of predominantly low cloud a novel method to separate infrared brightness temperatures measured by geostationary satellites into cloudy and cloud free pixels. The resulting cloud identification maps have a native spatial resolution of 4 km x 4 km and are available every 30 minutes from 2003-2010. This unique dataset of marine stratocumulus regions allows us to examine cloud fraction variability on time scales of a few hours, in all three regions, and across the diurnal cycle. The key results from our analysis using this dataset are summarized below. These results are synthesized with the results from the previous chapter in the conclusions and future work chapter.

Confirmatory Results:

- 1) Seasonal mean cloud fraction in each of the three regions is strongly correlated to seasonal mean lower tropospheric stability (Fig. 3.17). In the SE Pacific and SE Atlantic, the spatial structure of seasonal mean low cloud fractions very closely resembles the spatial patterns in stability (Fig. 3.16). [Klein and Hartmann 1993; Klein 1997; Wood and Bretherton 2006; Myers and Norris 2013]
- 2) There is interannual variability in low cloud fraction and lower tropospheric stability in all three regions. In some, but not all, years the variability is in phase with the expected changes from the El Niño Southern Oscillation (Fig. 3.18). [Klein and Hartmann 1993; Clement et al. 2009; Wood 2012]
- 3) Cloud fraction variability in the NE Pacific is larger than the two southern hemisphere regions and is less strongly driven by annual and seasonal cycles (Fig. 3.20; Fig. 3.27; Fig. 3.42). This may be related to the proximity of the cloud deck

to the northern hemisphere storm track and the ITCZ (Fig. 3.44). [Klein and Hartmann 1993; Wood and Hartmann 2006; George and Wood 2010; Toniazzo et al. 2011]

New Results:

- 1) The diurnal cycle of low cloud fraction within a given season and region unfolds in a very regular manner. Total low cloud fraction begins to decrease shortly after sunrise and continues to decrease until roughly 3:00 pm (Fig. 3.20). The maximum rate at which the cloud deck breaks up occurs just before or at local solar noon (Fig. 3.21). The rate of change of cloud fraction is closely tied to incoming shortwave radiative flux.
- 2) The largest diurnal cycles and earliest time of cloud break up occur on the edges of the cloud field where cloud fractions are in general lower (Fig. 3.19 and Appendix A). This could be indicative of a positive feedback through which low cloud fraction regions create conditions more favorable for cloud breakup.
- 3) Cloud fractions within a given $3^\circ \times 3^\circ$ box are very likely to have a net decrease during the day and a net increase overnight (Fig. 3.25-3.26). Deviations from these trends occur relatively infrequently, particularly in the SE Pacific and SE Atlantic. Localized decreases in cloud fraction greater than 20% overnight, such as those that would result from the formation of POCs, occur less than 5% of the time in the SE Pacific and SE Atlantic (Fig. 3.28). In the SE Pacific and SE Atlantic, a $3^\circ \times 3^\circ$ region that saw cloudiness increase above 90% at any point during the night has only a 1 in 50 chance of having a cloud fraction lower than 60% at sunrise.
- 4) In the SE Pacific and SE Atlantic, over eight years of data, the largest fractional decrease in total low cloud cover overnight (~15% in both regions) was smaller than the mean amount of total cloud breakup that occurs on any given day (30% in the SE Pacific and 35% in the SE Atlantic). The mean amount of cloud breakup overnight is an order of magnitude smaller than the mean decrease in cloudiness observed during the day (Fig. 3.30).

- 5) Cases where cloud fraction does decrease overnight are more likely to occur on the edges of the cloud deck and during the peak cloudiness season (Fig. 3.31 and Figs. 3.32-3.34).
- 6) The distribution of the area fraction of heavy drizzle is similar on nights where cloud fraction increases, decreases, and decreases significantly overnight (Figs. 3.32-3.34). Many of the cases where cloud fraction significantly decreases overnight have little to no drizzle present. This suggests that drizzle is not a necessary condition for cloud breakup overnight. Drizzle area is not strongly correlated with changes in cloud fraction on time scales of a few hours.
- 7) For a given $3^\circ \times 3^\circ$ box, cloud top temperatures have a tendency to be anomalously warmer (shallower clouds) on nights in which cloud fraction decreases overnight (Figs. 3.32-3.34). It is not clear if this is a cause or result of low cloud fractions. The deepening of the boundary layer overnight via entrainment could be suppressed in low cloud fraction scenarios thus creating lower cloud tops.
- 8) We were able to explain up to 50% of the total variance of cloud fraction (calculated on 30 minute time scales in $3^\circ \times 3^\circ$ boxes) with an empirical model that only took into account the time of day and day of the year (Fig. 3.42). More variance was explained in regions with larger seasonal and diurnal cycles and less variance was explained in the NE Pacific compared to the SE Pacific or SE Atlantic.

3.6 Chapter 3 Tables

Table 3.1. A simplified summary of some the processes which have been demonstrated to modify stratocumulus cloud fraction (CF).

Process/Parameter	Impact	Modified By
Cloud Condensation Nuclei Concentration	Concentration \uparrow - CF \uparrow	Boundary layer winds, precipitation, shortwave radiation, boundary layer mixing
Boundary Layer Depth	Depth \uparrow - CF \downarrow	Boundary layer temperature, shortwave radiation, tropospheric subsidence, boundary layer mixing
Boundary Layer Mixing	Coupled – CF \uparrow Decoupled – CF \downarrow	Shortwave radiation, precipitation and outflow boundaries, winds
Inversion Strength	Stronger Inversion – CF \uparrow Weaker Inversion – CF \downarrow	Tropospheric subsidence, boundary layer temperature, sea surface temperature
Precipitation	Precipitation \uparrow - CF \downarrow	Boundary layer depth and gravity waves, aerosol concentrations, boundary layer mixing

Table 3.2. A summary of the data sources to be used in my analysis.

Variable (Proxy)	Input Data Product	Native Spatial Resolution	Spatial Coverage	Temporal Resolution	Temporal Coverage
Cloud Fraction	Merged-IR Brightness Temp.	4 km x 4 km	60°S:60°N	30 min	Feb-2000 to Dec-2012
Aerosol/CCN Concentration (Cloud Droplet Number Concentration)	MODIS Level-3 Effective Radius and Optical Thickness	5 km x 5 km	Global	Once Daily ~1:30 pm local	Sep-2002 to Aug-2011
Boundary Layer Depth (Cloud Top Temperature and Pressure)	Infrared and Visible Emission	5 km x 5 km	Global	Twice Daily ~1:30 am/pm local	Sep-2002 to Aug-2011
Inversion Strength (Lower Tropospheric Stability)	ECMWF ERA-Interim Reanalysis	0.7° x 0.7°	Global	0Z, 6Z, 12Z, and 18Z	1989 - Current
Precipitation (Drizzle Detection)	AMSRE 89-GHz Passive MW	6 km x 4 km	Global	Twice Daily ~1:30 am/pm local	Sep-2002 to Aug-2011

Table 3.3. The variance explained by the seasonal and diurnal cycles from a simple empirical model. Cloud fractions are calculated in the 3° x 3° boxes shown in Fig. 3.10.

	30 Minute Cloud Fraction	Daily Mean Cloud Fraction	Weekly Mean Cloud Fraction	Monthly Mean Cloud Fraction
NE Pacific	Mean = 11% Max = 19%	Mean = 20% Max = 60%	Mean = 22% Max = 72%	Mean = 38% Max = 88%
SE Pacific	Mean = 32% Max = 63%	Mean = 33% Max = 71%	Mean = 45% Max = 83%	Mean = 60% Max = 90%
SE Atlantic	Mean = 33% Max = 51%	Mean = 36% Max = 60%	Mean = 51% Max = 76%	Mean = 70% Max = 88%

3.7 Chapter 3 Figures

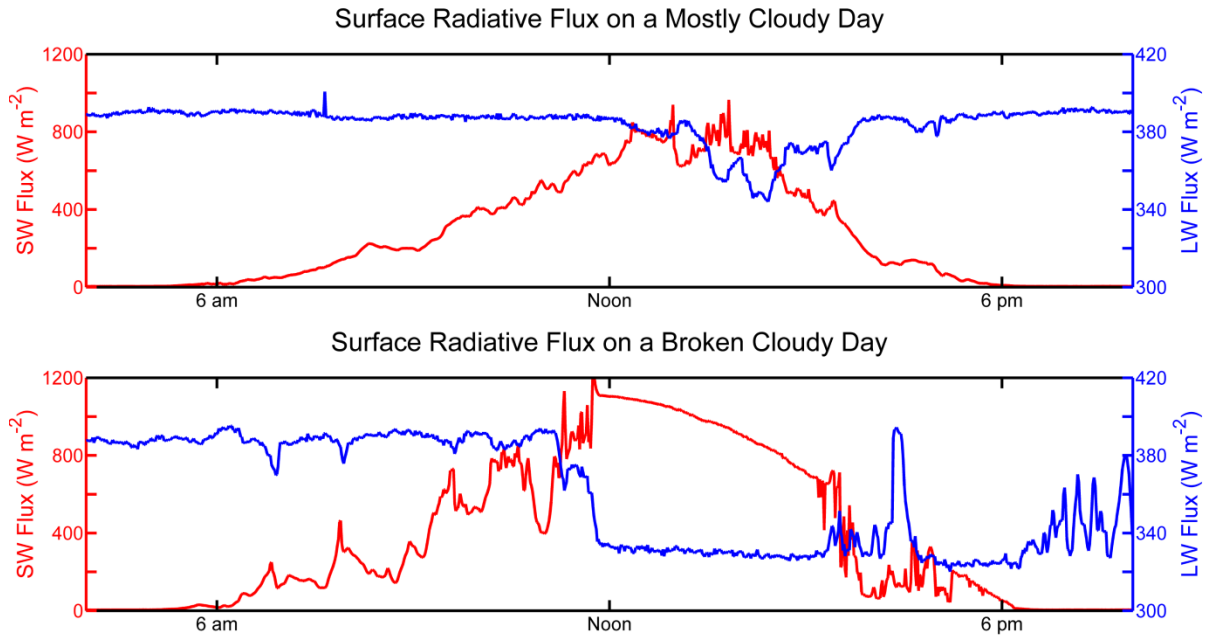


Figure 3.1. Time series of shortwave (red lines) and longwave (blue lines) radiative flux reaching the surface on a mostly cloudy day (top panel; from 11-Nov 2008 near 75°W and 20°S) and on a day when the cloud completely breaks up during the afternoon (bottom panel; from 23-Nov 2008 near 83°W and 21°S). Data were collected aboard the *RHB* during VOCALS-REx.

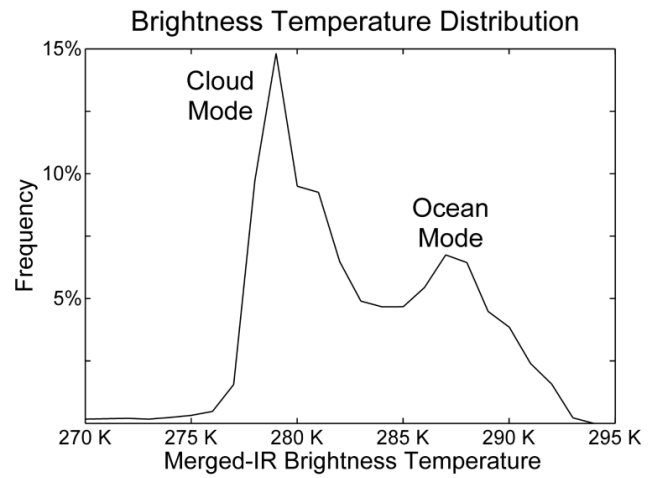
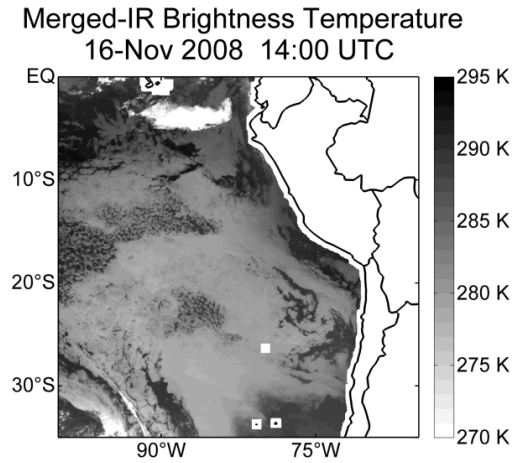


Figure 3.2. Infrared brightness temperatures over the southeast Pacific stratocumulus deck at 1400 UTC on 16-November 2008 (left) and the bimodal distribution of brightness temperatures for the scene (right).

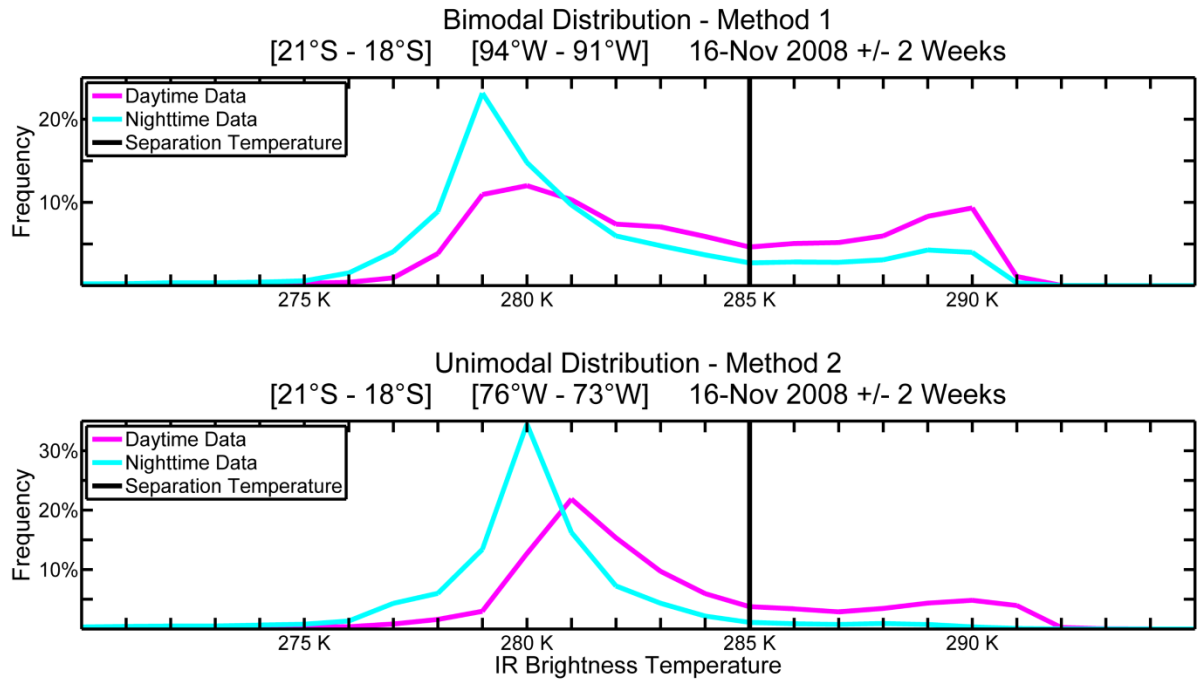
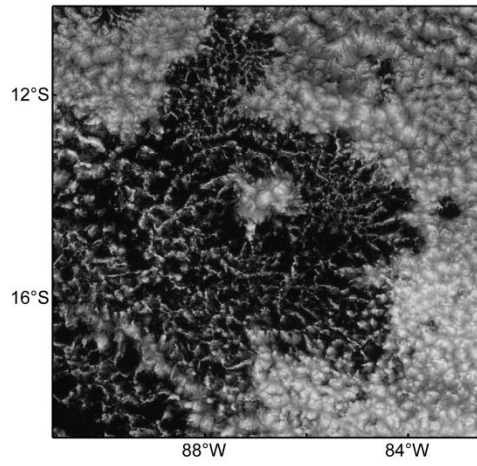
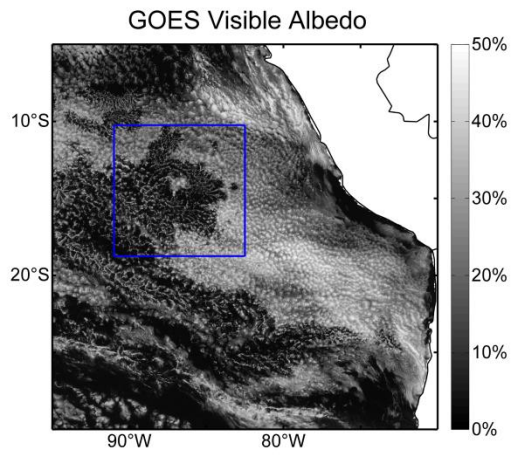
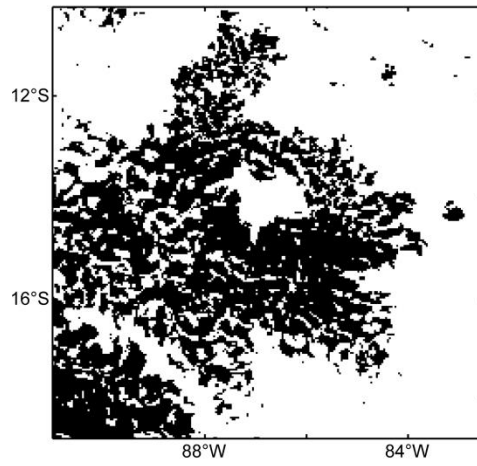
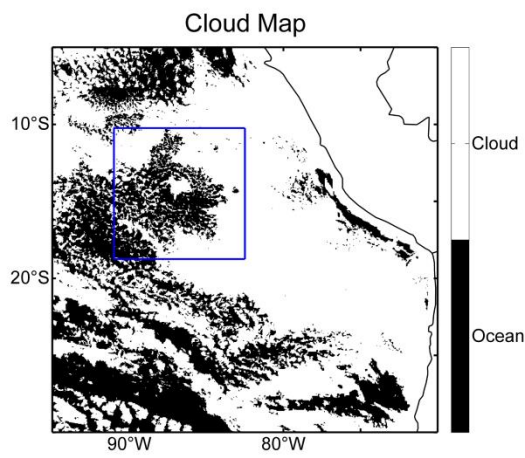
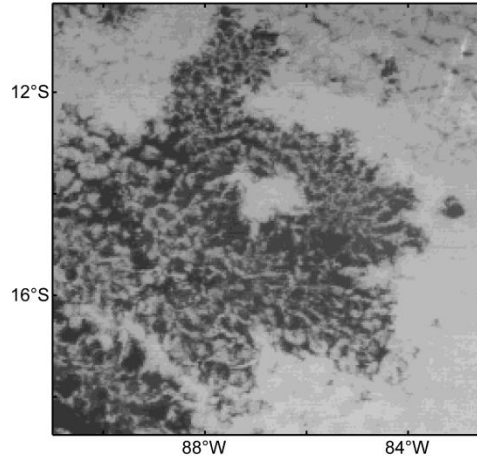
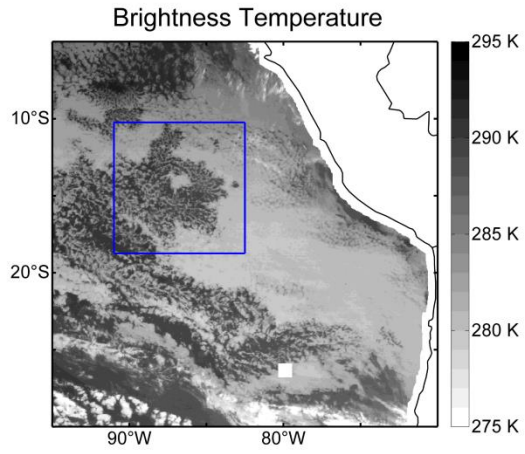


Figure 3.3. Two examples of the accumulated brightness temperature distributions in $3^\circ \times 3^\circ$ boxes over the southeast Pacific. The top panel shows an example of a region well offshore where the cloud fractions are lower and the distribution of daytime temperatures more bimodal. In contrast, the distributions shown in the bottom panel come from an area closer to the coast where cloud fractions remain high even during the day, resulting in a mostly unimodal distribution of brightness temperatures.

Figure 3.4. In the top row are brightness temperatures from the merged-IR dataset over the SE Pacific at 1600 UTC on 11-October 2008. The middle row contains the corresponding total cloud map generated using the new cloud identification methodology. The merged-IR cloud map can be compared with the GOES visible albedo shown in the bottom row. The right column shows the $8.5^\circ \times 8.5^\circ$ region that is outlined in blue in the left column.



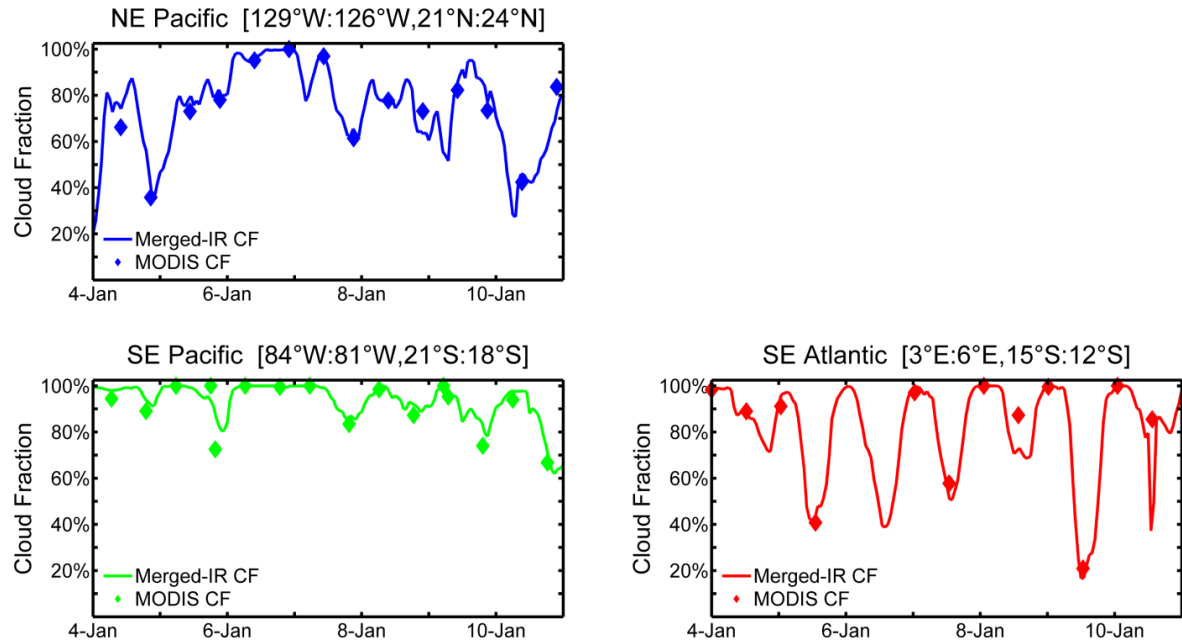


Figure 3.5. Merged-IR (lines) and MODIS (diamonds) total cloud fraction for $3^\circ \times 3^\circ$ boxes in each of the stratocumulus regions for the period between 4-January and 11-January 2004. MODIS pixels with fractional cloudiness greater than 0.87 are classified as cloud in the raw MODIS swaths before calculating cloud fraction to create a more direct comparison.

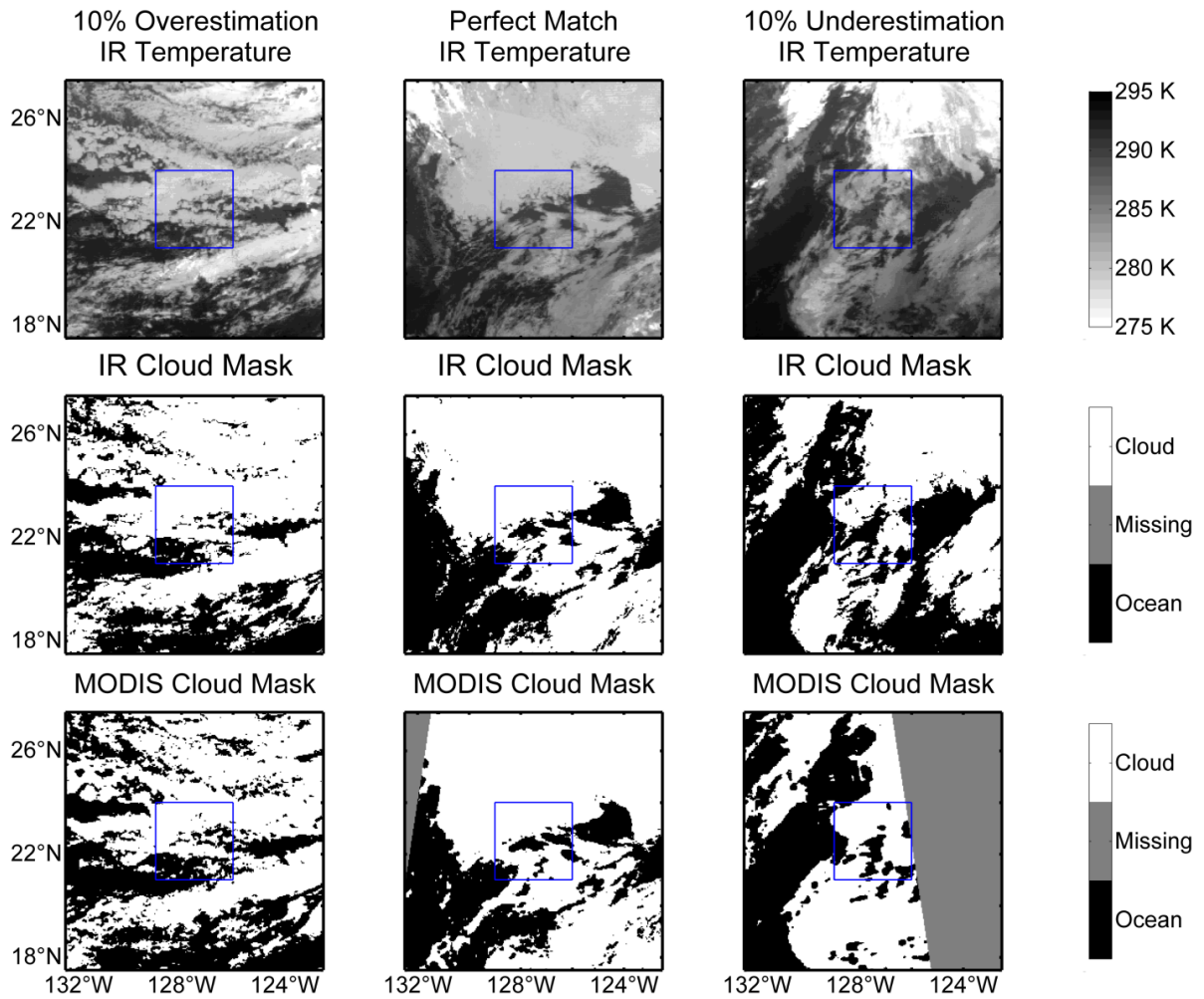


Figure 3.6. An example of scenes where the merged-IR cloud identification method overestimates cloud fraction by 10% compared to the MODIS total cloud fraction (left column; 4-January 2004 at 10:00 UTC), is a perfect match (center column; 8-January 2004 at 09:30 UTC), and underestimates total cloud fraction by 10% (right column; 8-January 2004 at 22:00 UTC). The top row shows the merged-IR brightness temperatures while the merged-IR and MODIS cloud masks are in the middle and bottom rows respectively.

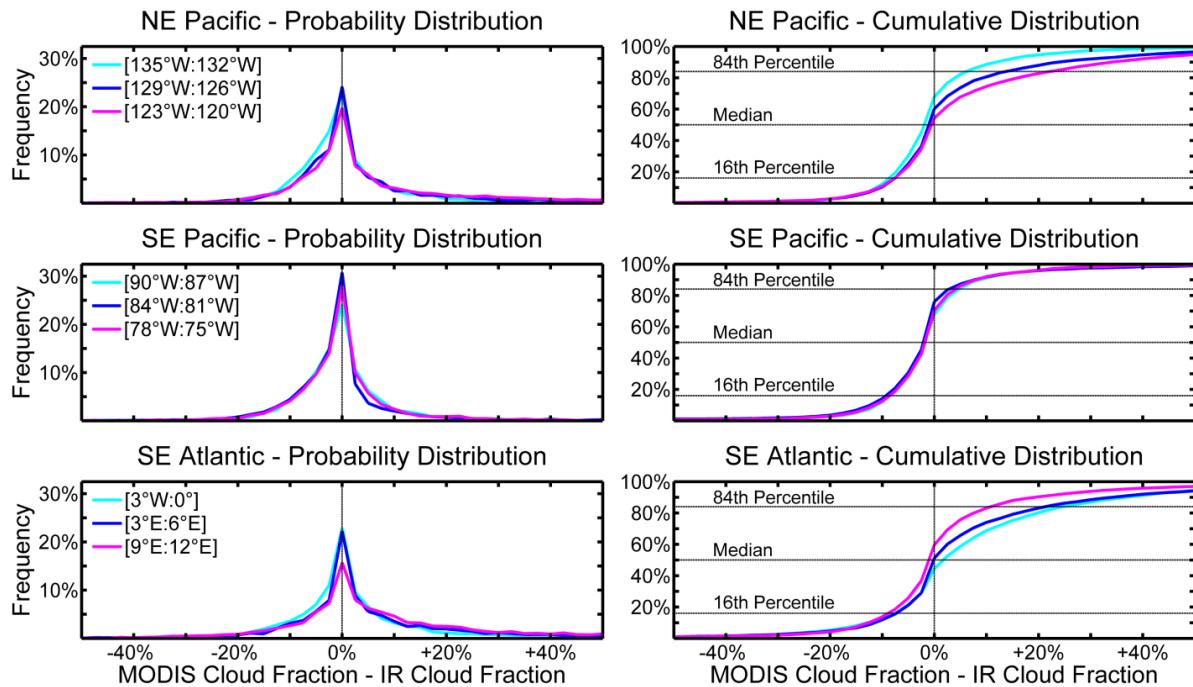


Figure 3.7. Distribution of the difference between the MODIS and merged-IR total cloud fraction (left) and the cumulative frequency of the difference (right) for multiple $3^\circ \times 3^\circ$ boxes spanning an east-west gradient from 21°N to 24°N in the NE Pacific, 21°S to 18°S in the SE Pacific, and 15°S to 12°S in the SE Atlantic. Distributions are collected from roughly 5000 MODIS overpasses between 2003 and 2010.

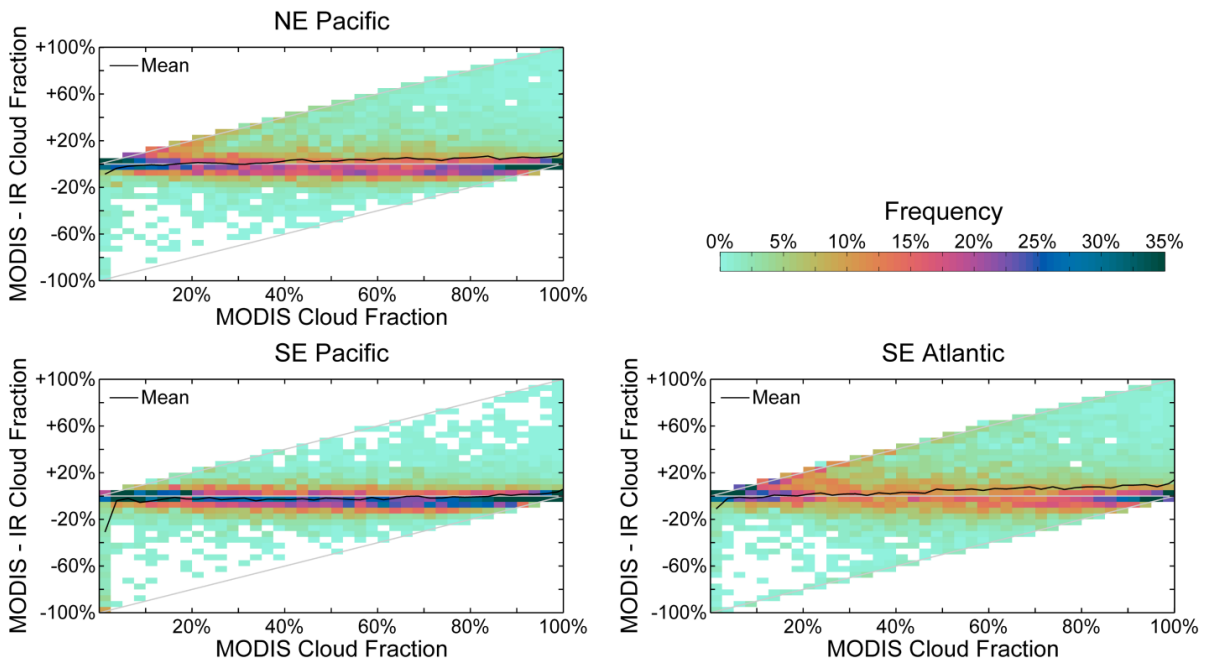


Figure 3.8. Data density diagram showing the frequency of occurrence of a differences between the MODIS and merged-IR total cloud fraction conditioned on the value of the observed MODIS cloud fraction in the NE Pacific (top left), SE Pacific (bottom left), and SE Atlantic (bottom right). Darker colors indicate more frequent occurrences. The solid black line in each plot indicates the mean difference for a given MODIS cloud fraction.

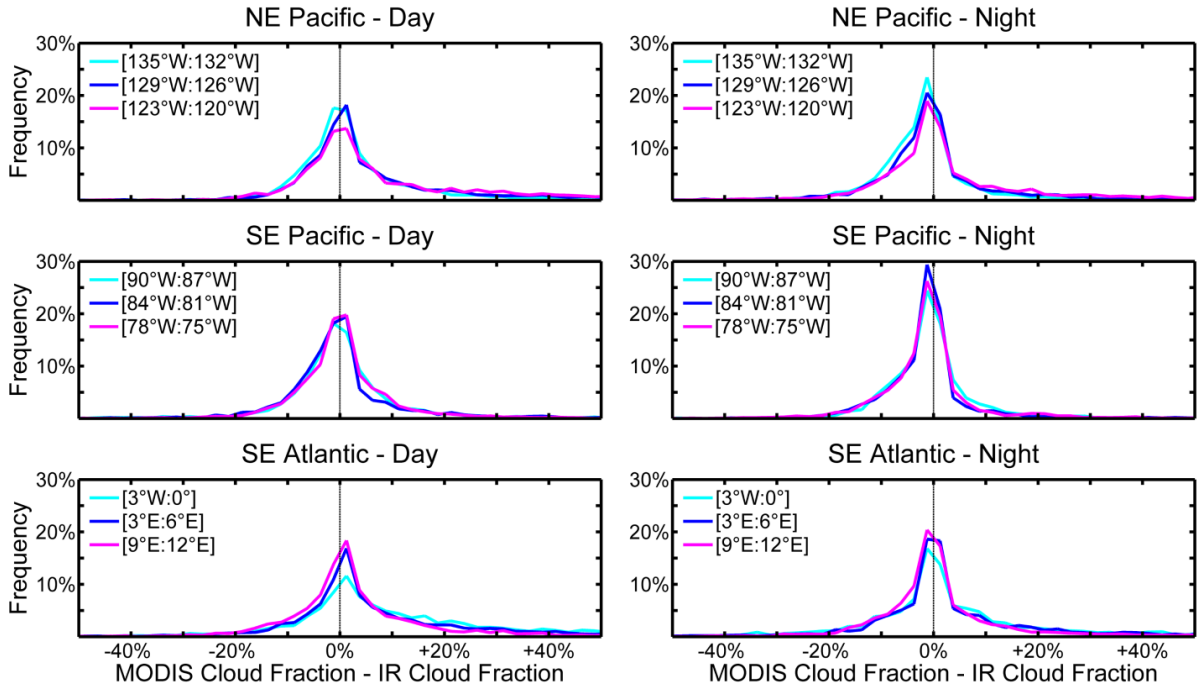


Figure 3.9. Distribution of the difference between the MODIS and merged-IR total cloud fraction during daytime overpasses (left column) and nighttime overpasses (right column) for multiple $3^\circ \times 3^\circ$ boxes spanning an east-west gradient from 21°N to 24°N in the NE Pacific, 21°S to 18°S in the SE Pacific, and 15°S to 12°S in the SE Atlantic.

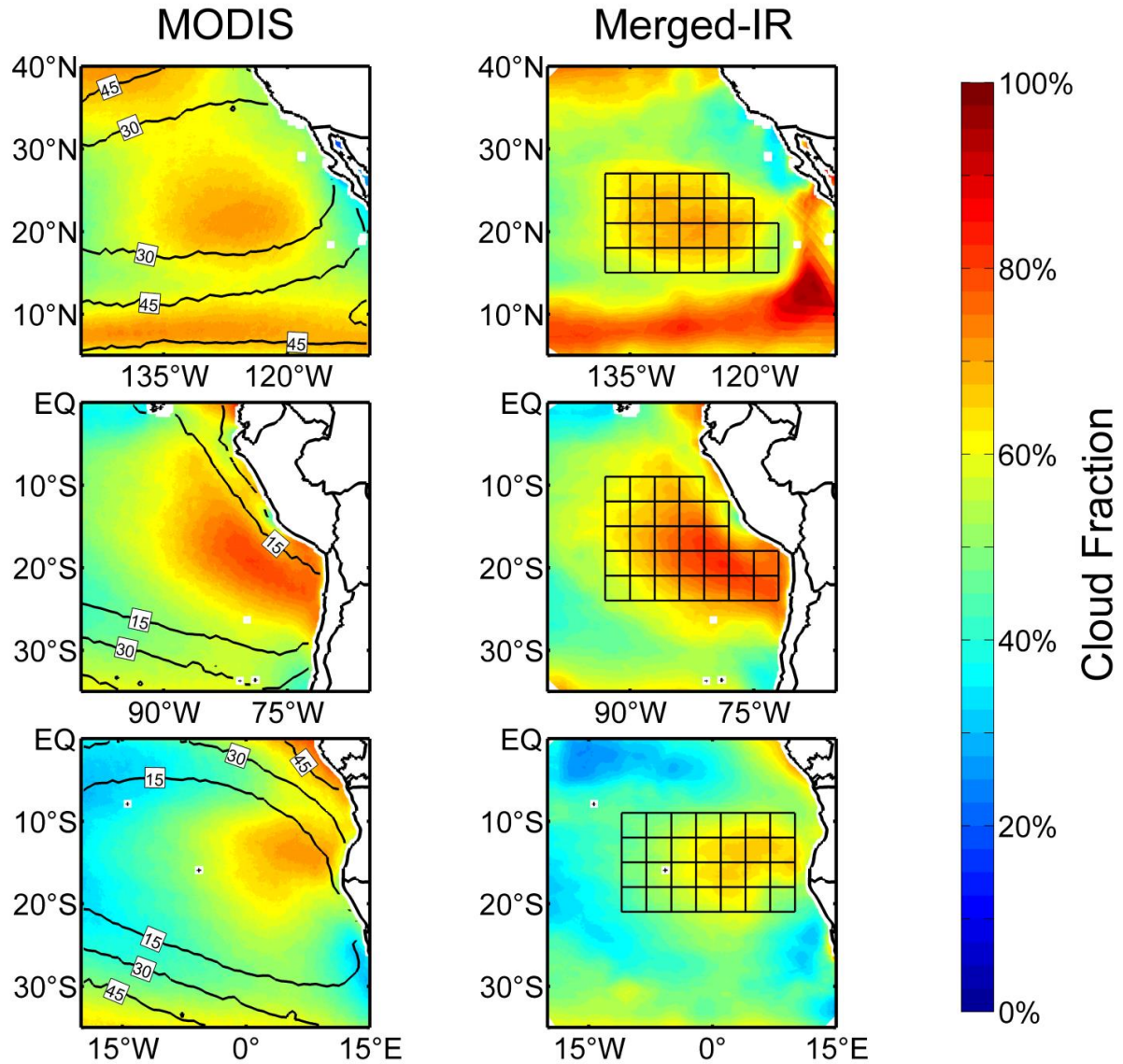


Figure 3.10. Annual mean total cloud fraction from the MODIS cloud product (left) and from the merged-IR cloud identification method (right) in the NE Pacific (top row), SE Pacific (middle row), and SE Atlantic (bottom row). Contours in the left hand column are the frequency (%) of cloud top temperatures colder than 273 K. The merged-IR data is taken only from times of a corresponding MODIS overpass (i.e. the 30 minute scene closest to the MODIS overpass). Boxes in the right column show the $3^\circ \times 3^\circ$ boxes in which low cloud fraction was calculated for the time series analysis in the remainder of the paper.

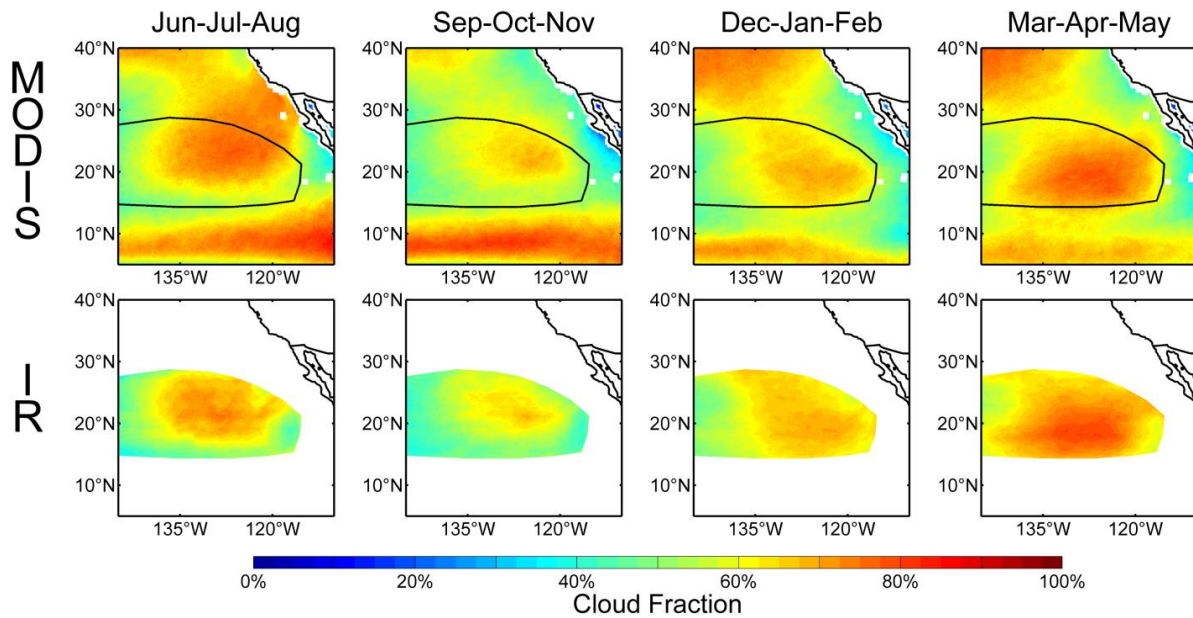


Figure 3.11. The mean MODIS (top row) and merged-IR (bottom row) total cloud fraction for each of the four seasons (columns) in the NE Pacific. MODIS pixels with fractional cloudiness greater than 0.87 are classified as cloud in the raw MODIS swaths before calculating cloud fraction to create a more direct comparison. The merged-IR data is taken only from times of a corresponding MODIS overpass (i.e. the 30 minute scene closest to 1:30 am/pm). The solid line indicates regions of merged-IR data without the zenith angle correction error and where cloud top temperatures colder than 273 K occur less than 35% of the time.

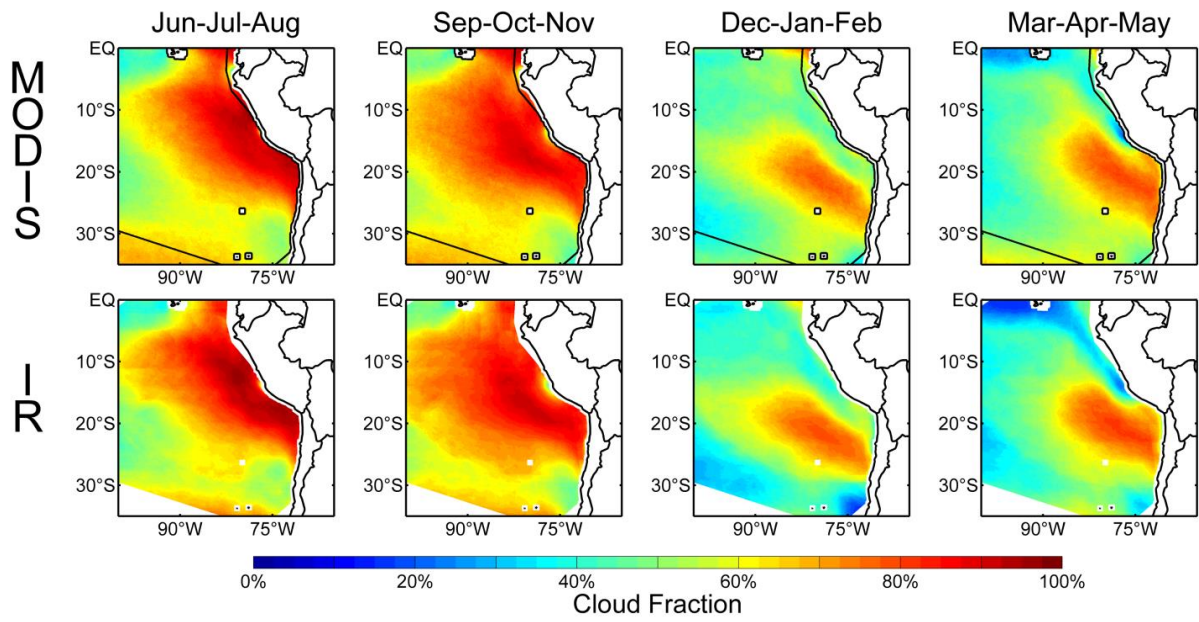


Figure 3.12. As in Figure 3.11 but for the SE Pacific.

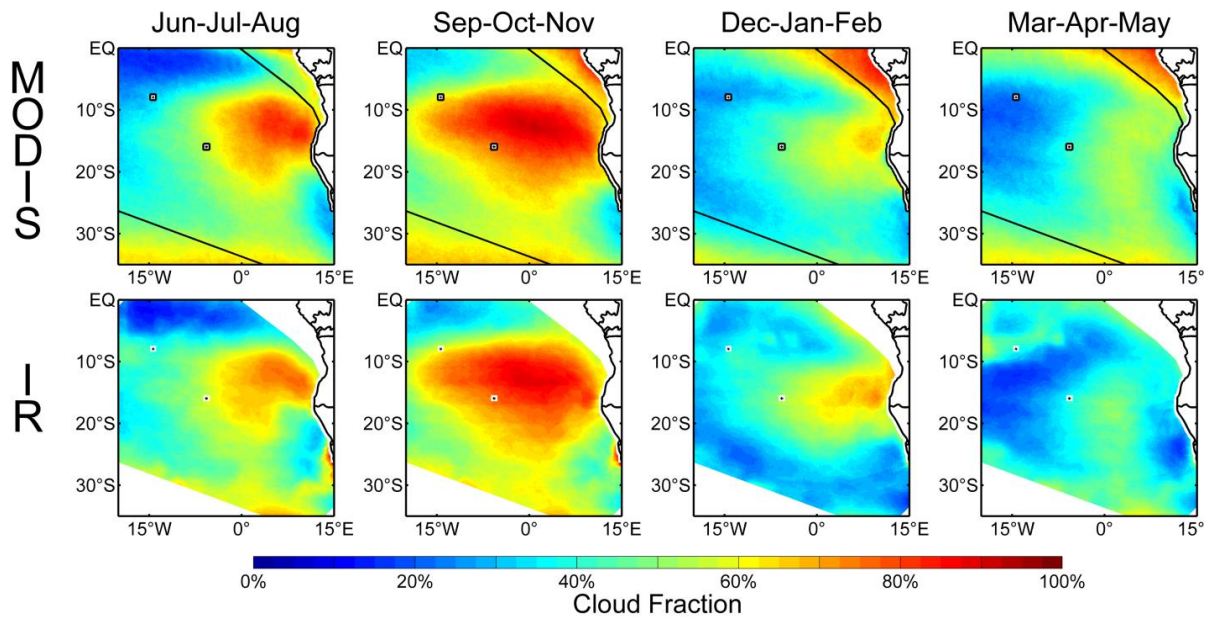


Figure 3.13. As in Figure 3.11 but for the SE Atlantic.

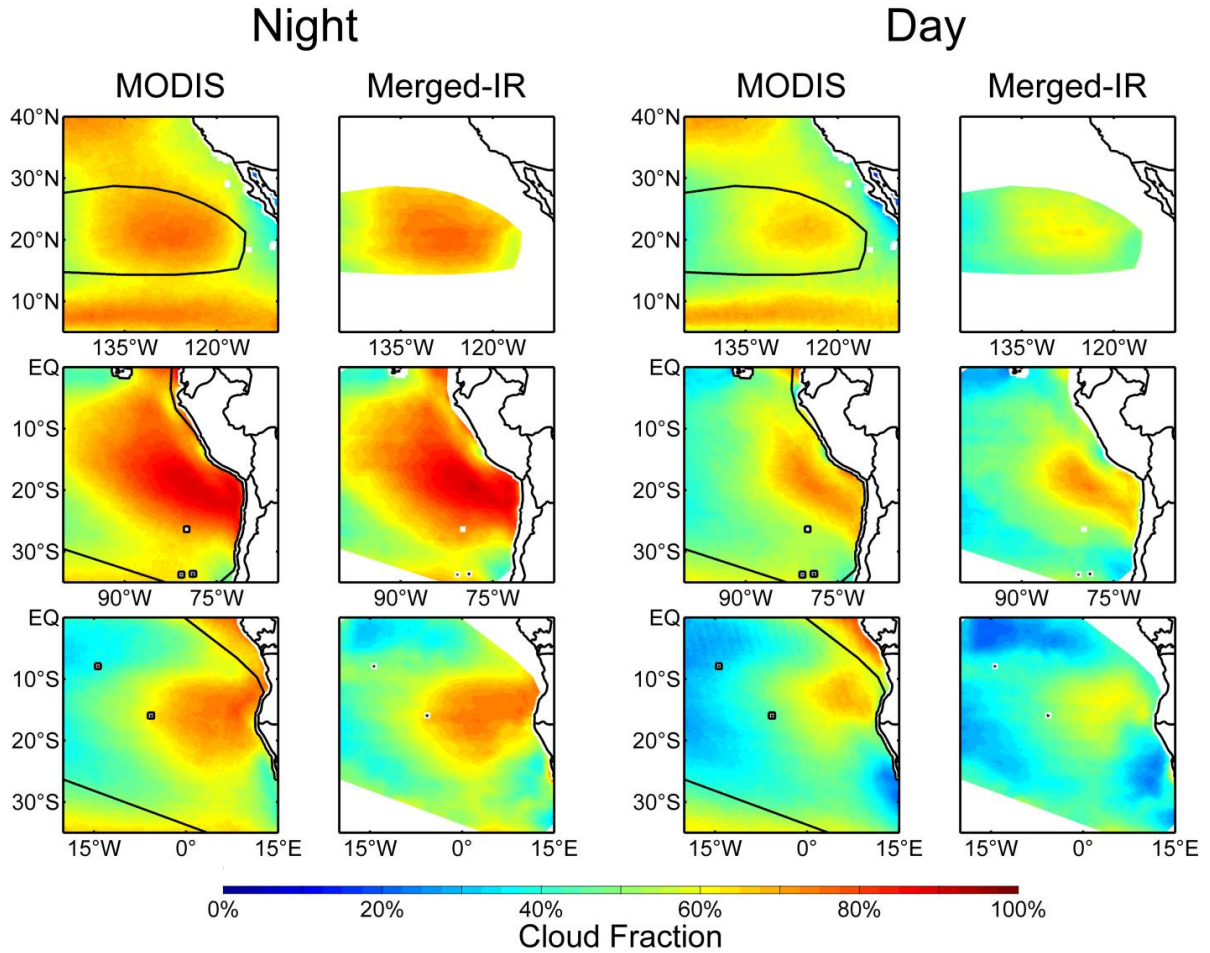


Figure 3.14. Mean cloud fraction over all seasons at night (left two columns) and during the day (right two columns) in the NE Pacific (top row), SE Pacific (middle row), and SE Atlantic (bottom row). The merged-IR data is taken only from times of a corresponding MODIS overpass (i.e. the 30 minute scene closest to 1:30 am/pm). The solid line indicates regions of merged-IR data without the zenith angle correction error and where cloud top temperatures colder than 273 K occur less than 35% of the time.

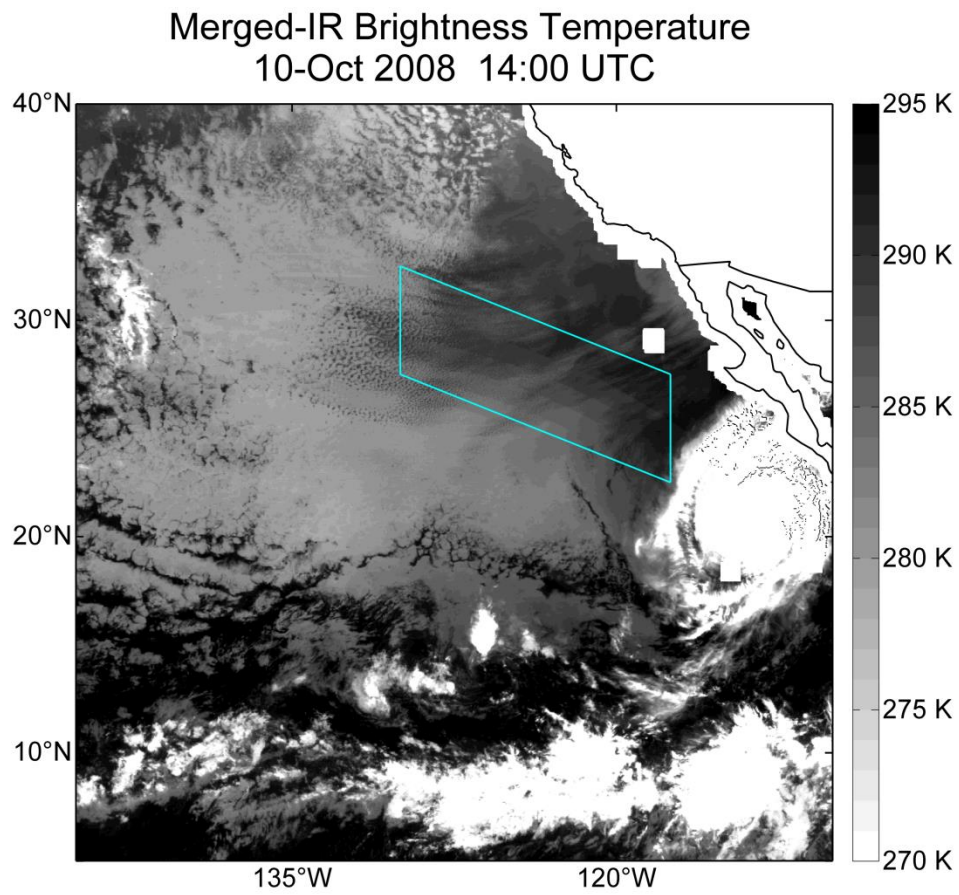


Figure 3.15. Infrared brightness temperatures observed off the coast of California at 14:00 UTC on 10-Oct 2008. An example of the zenith angle correction error can be seen in the arcs of lower brightness temperatures within the blue box.

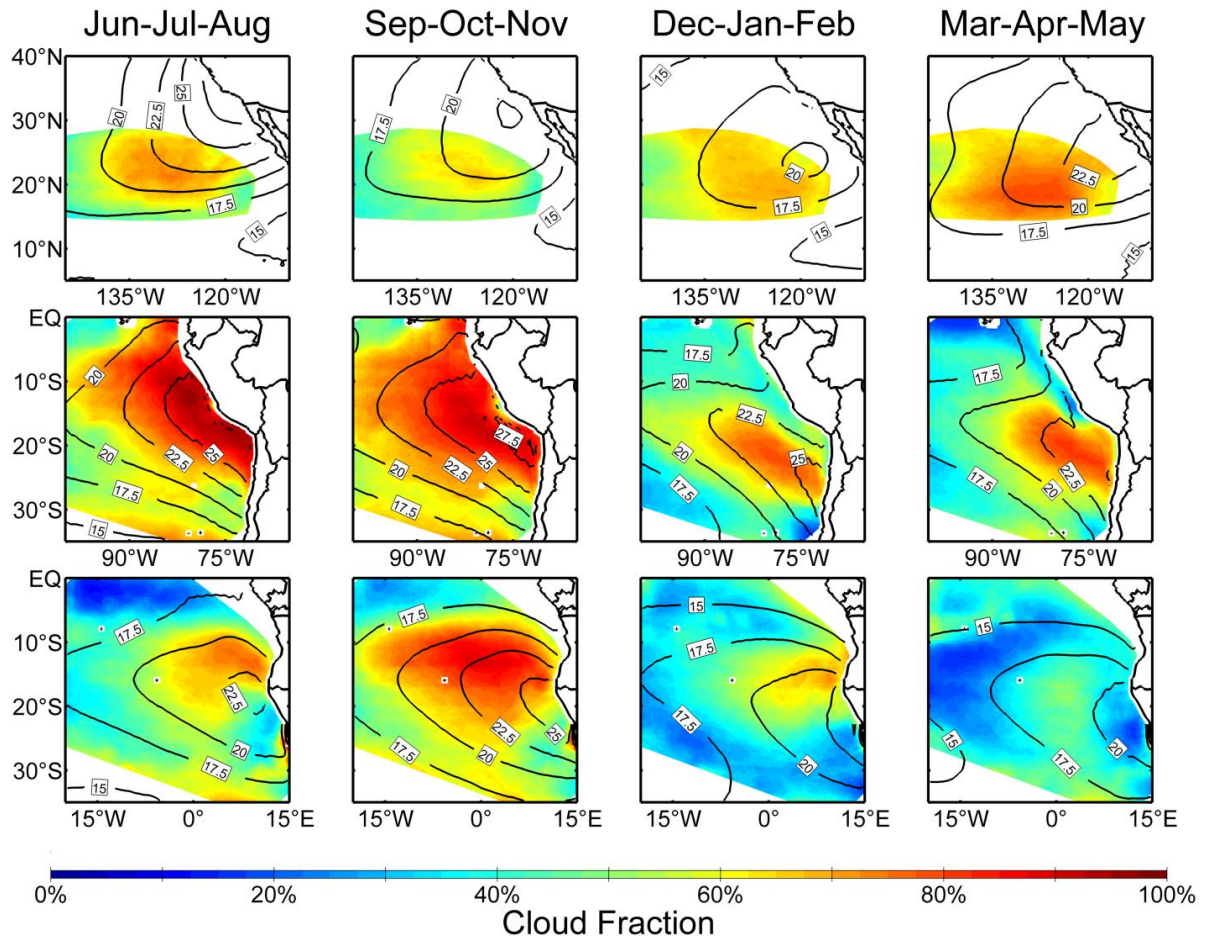


Figure 3.16. Mean merged-IR cloud fraction for each season (column) in the NE Pacific (top row), SE Pacific (middle row), and SE Atlantic (bottom row). Overlaid on each plot are contours of the seasonal mean lower tropospheric stability (K) from ECMWF reanalysis.

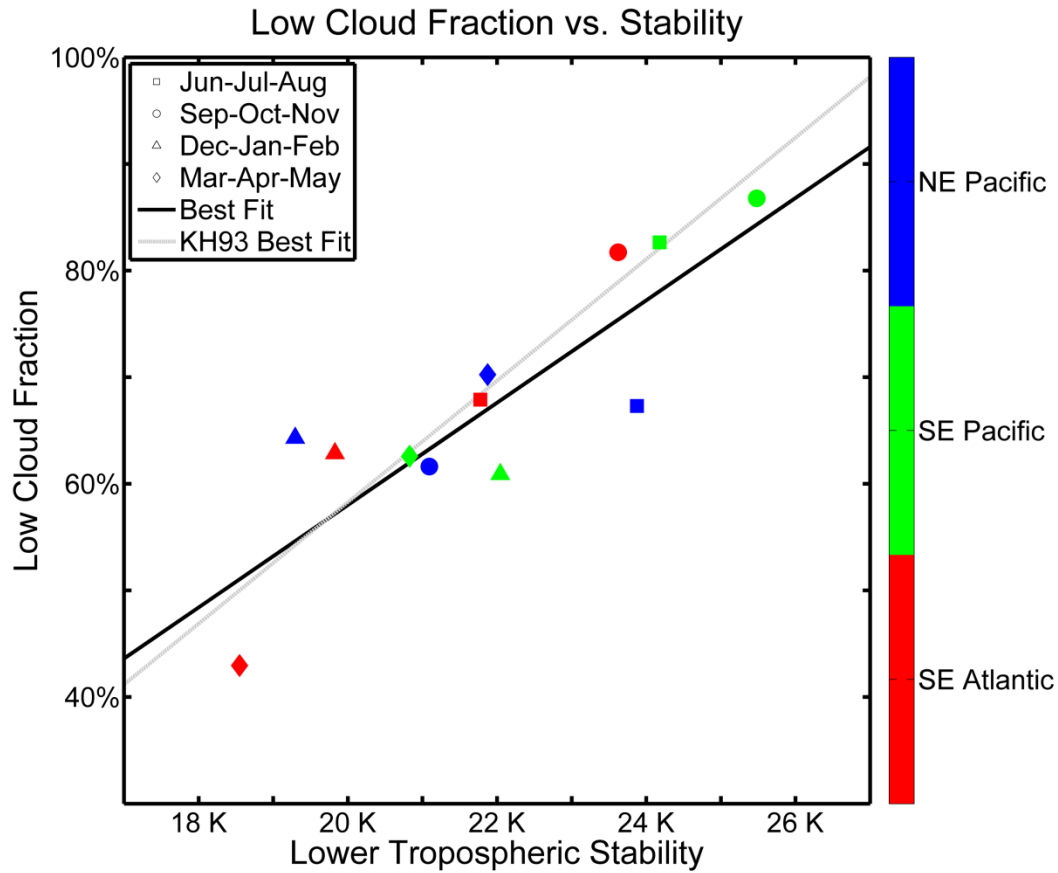


Figure 3.17. Mean lower tropospheric stability (x-axis) and low cloud fraction (y-axis) for each of the four seasons (symbols). The solid black line indicates the best fit relationship and the dotted gray line is the best fit relationship found in Klein and Hartmann (1993). Data are shown for the NE Pacific [130°W:120°W, 20°N:30°N], SE Pacific [90°W:80°W, 0°S:10°S], and SE Atlantic [0°:10°E, 20°S:10°S].

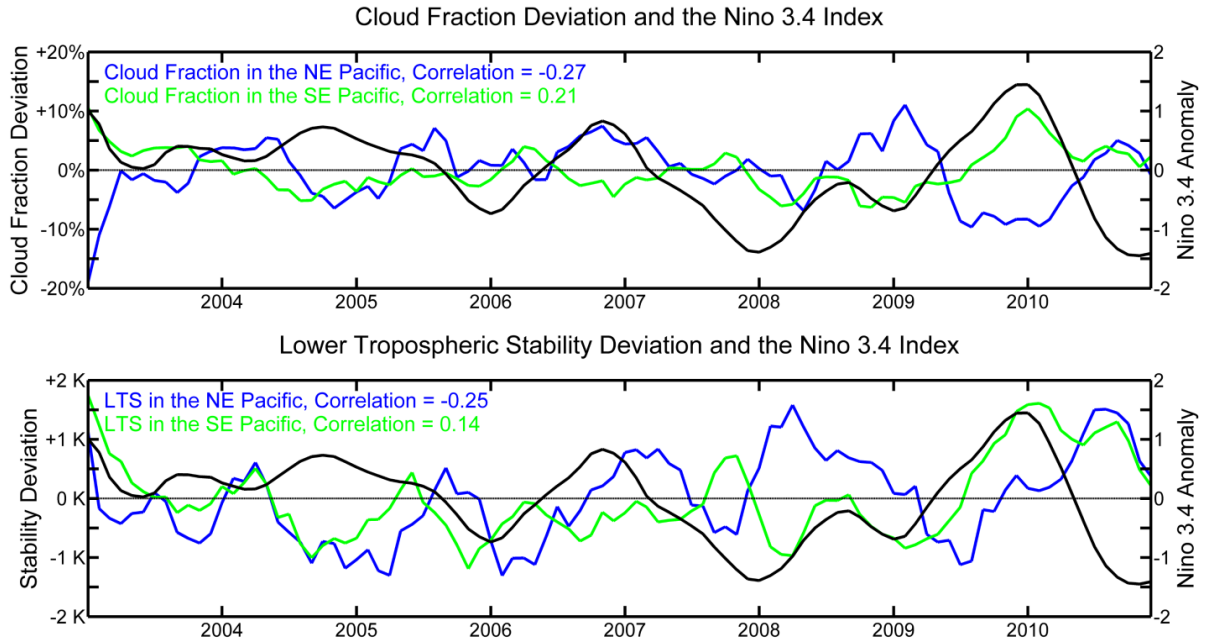


Figure 3.18. Top - Time series of monthly mean low cloud fraction with the mean annual cycle removed in the NE Pacific (blue line) and SE Pacific (green line) and the Niño 3.4 Index anomaly. Bottom - Time series of monthly mean lower tropospheric stability with the mean annual cycle removed in the NE Pacific (blue line) and SE Pacific (green line) and the Niño 3.4 Index anomaly. Cloud fraction and stability were calculated in the box [130°W:120°W, 20°N:30°N] in the NE Pacific and [90°W:80°W, 20°S:10°S] in the SE Pacific. Correlations for each time series are given in the legend.

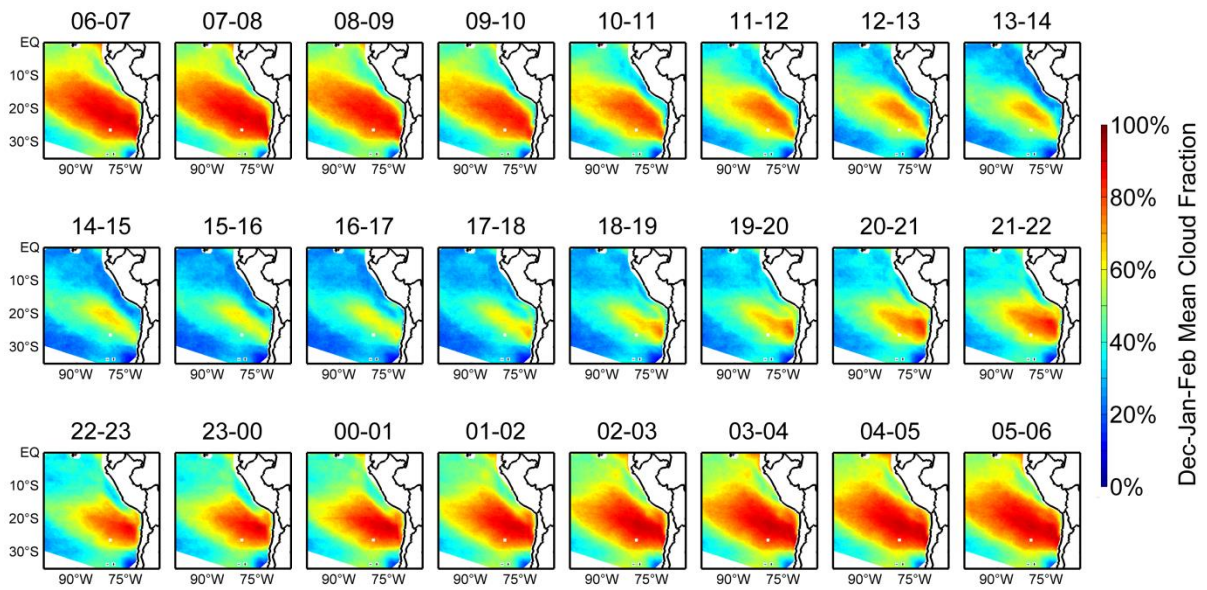


Figure 3.19. Hourly mean cloud fractions across the diurnal cycle during the minimum cloudiness season (December-January-February) in the SE Pacific. The local solar time is given at the top of each plot.

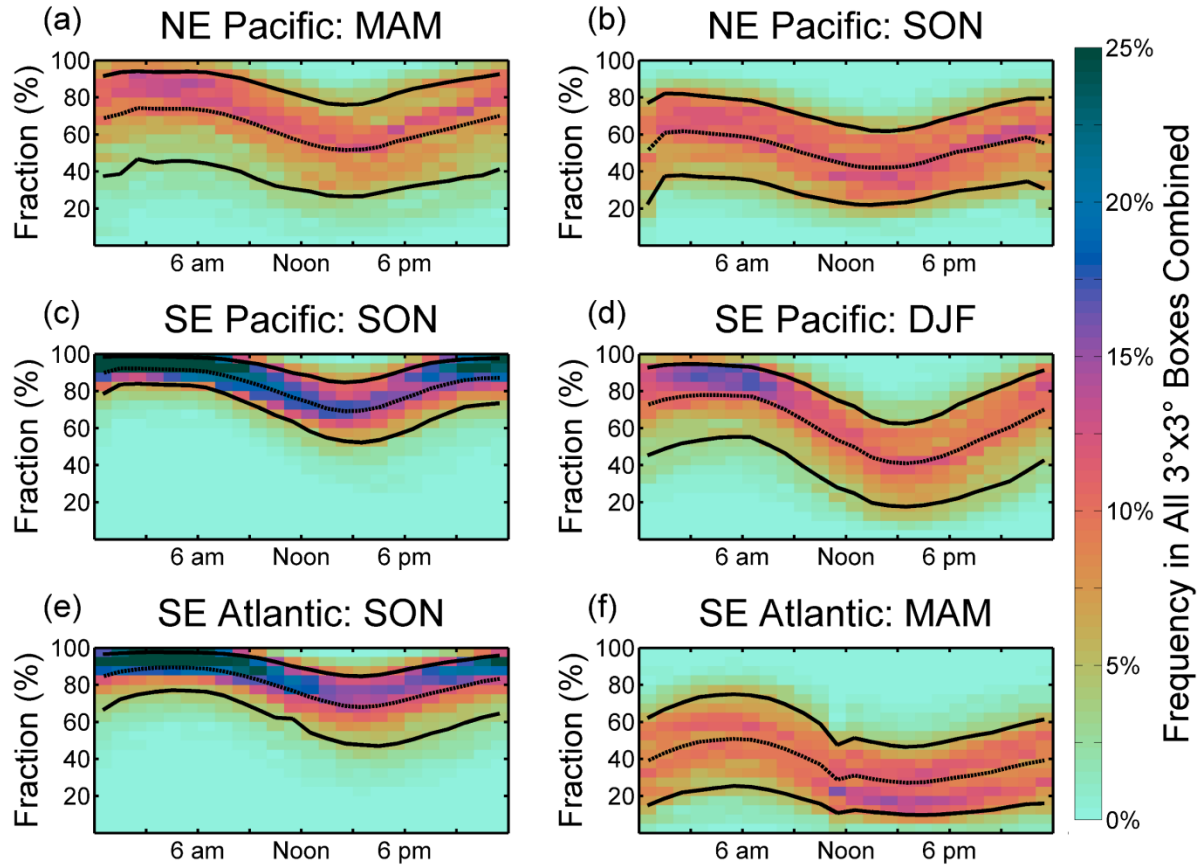


Figure 3.20. Frequency distribution of low cloud fraction across the diurnal cycle during the peak (left column) and minimum (right column) cloudiness seasons in NE Pacific (top row), SE Pacific (middle row), and SE Atlantic (bottom row). Cloud fractions are the total low cloud fraction in the $3^\circ \times 3^\circ$ boxes shown in Fig. 3.10. In all panels the solid black lines indicate the 10th and 90th percentiles of the hourly distribution while the dotted black line indicates the hourly mean.

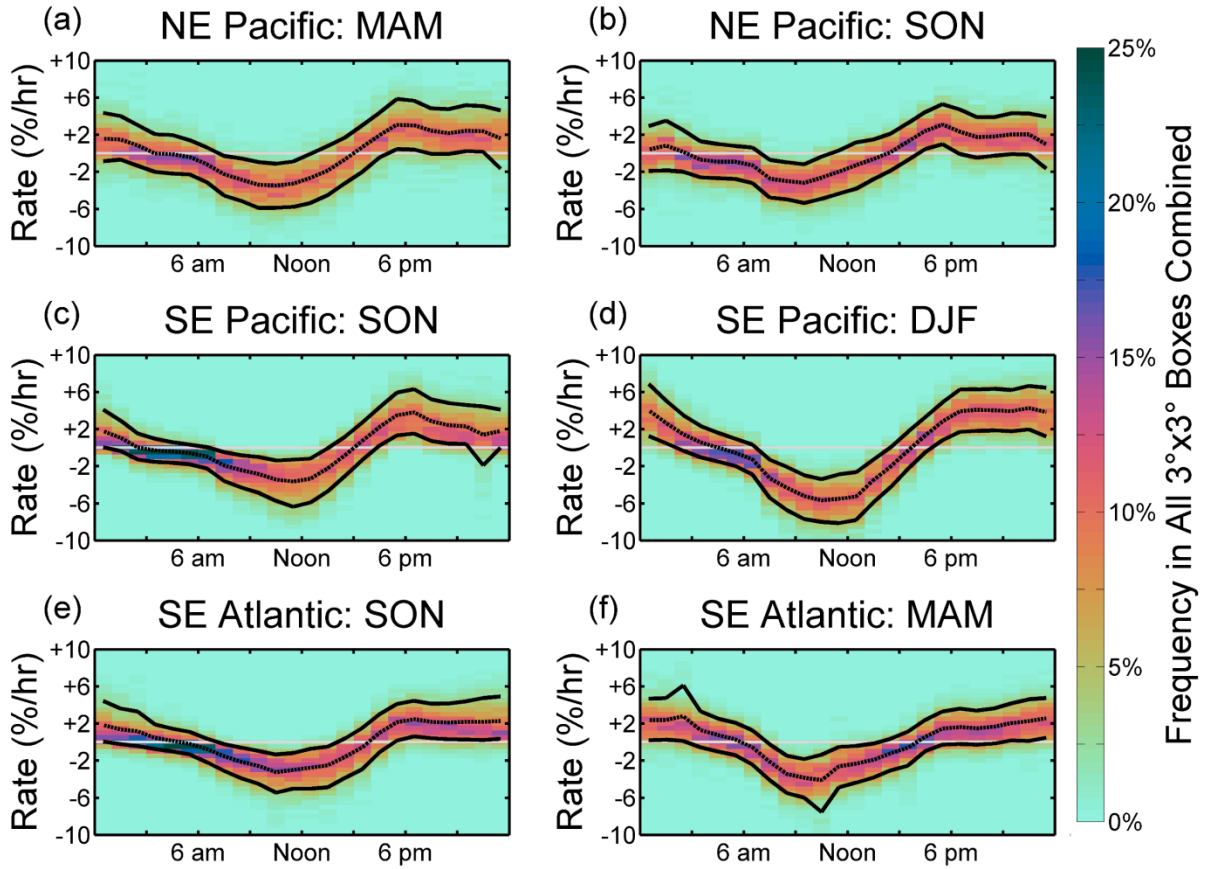


Figure 3.21. Frequency distribution of the rate of change of low cloud fraction between subsequent 30 minute scenes across the diurnal cycle during the peak (left column) and minimum (right column) cloudiness seasons in NE Pacific (top row), SE Pacific (middle row), and SE Atlantic (bottom row). Cloud fractions are the total low cloud fraction in the $3^\circ \times 3^\circ$ boxes shown in Fig. 3.10. In all panels the solid black lines indicate the 10th and 90th percentiles of the hourly distribution while the dotted black line indicates the hourly mean.

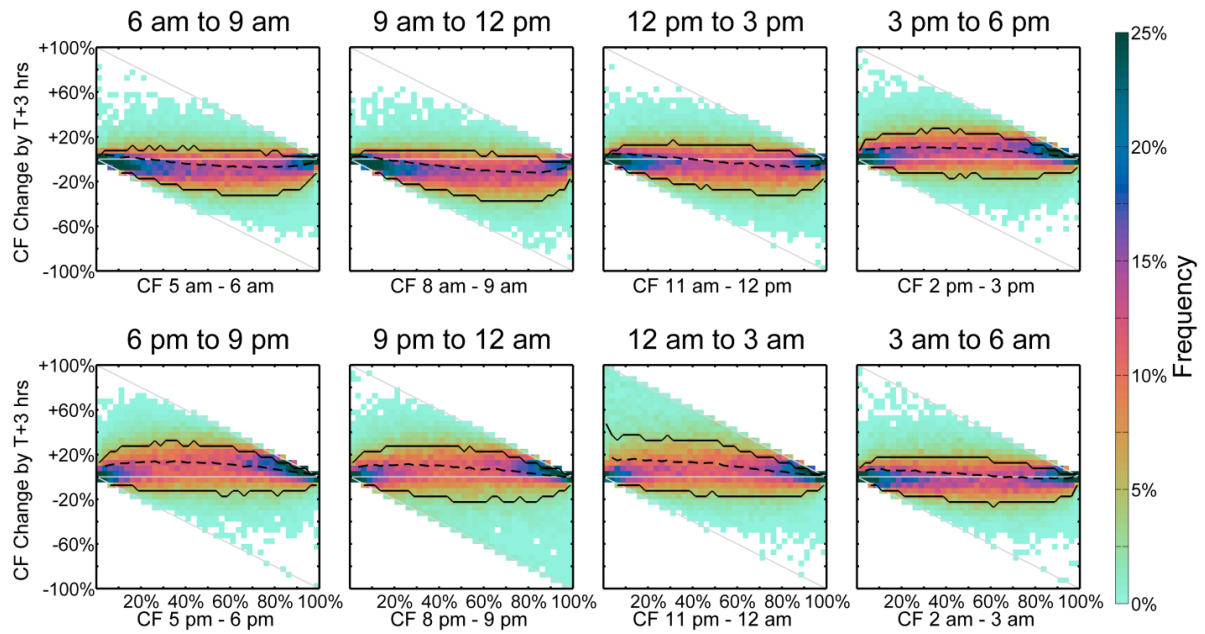


Figure 3.22. Data density diagrams showing the change of cloud fraction (y-axis) in three hour windows across the diurnal cycle conditioned on the starting cloud fraction (x-axis). Cloud fractions are calculated every 30 minutes in the $3^\circ \times 3^\circ$ boxes shown in Fig. 3.10. Darker colors indicate more frequent occurrences. In all panels the solid black lines indicate the 10th and 90th percentiles of the change distribution for a given starting cloud fraction while the dotted black line indicates the mean.

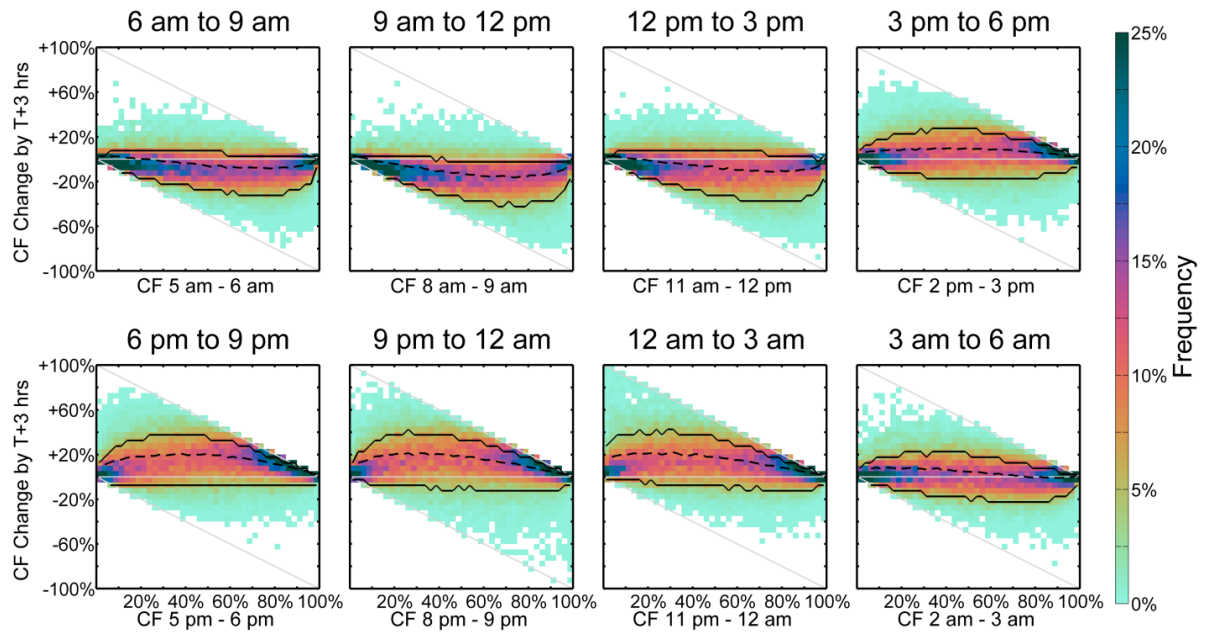


Figure 3.23. As in Figure 3.22 but for the SE Pacific.

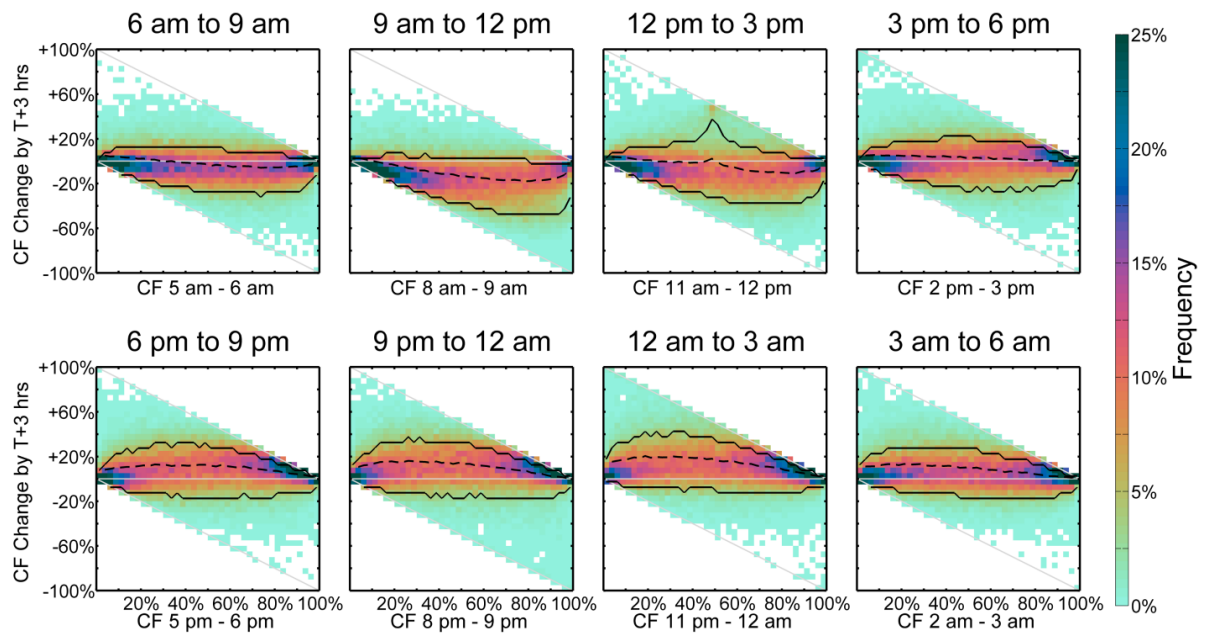


Figure 3.24. As in Figure 3.22 but for the SE Atlantic.

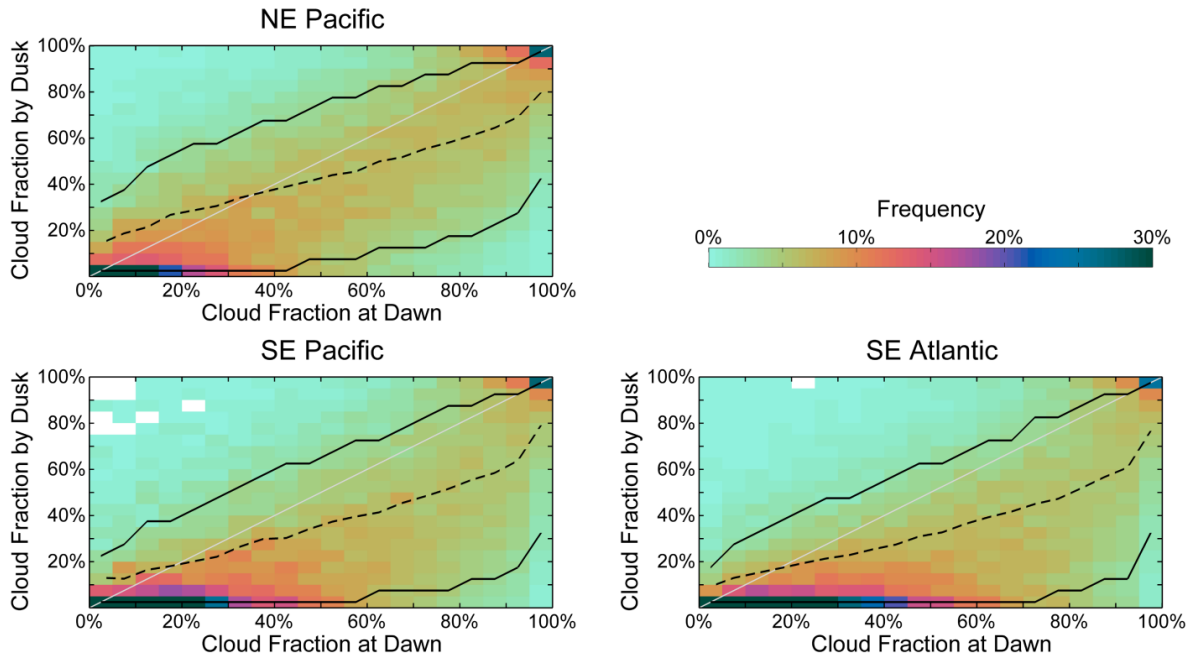


Figure 3.25. Data density diagrams showing the distribution of cloud fraction at dusk (y-axis) conditioned on the cloud fraction at dawn (x-axis). Cloud fractions are calculated in the $3^\circ \times 3^\circ$ boxes shown in Fig. 3.10. Darker colors indicate more frequent occurrences. In all panels the solid black lines indicate the 10th and 90th percentiles of the change distribution for a given starting cloud fraction while the dotted black line indicates the mean.

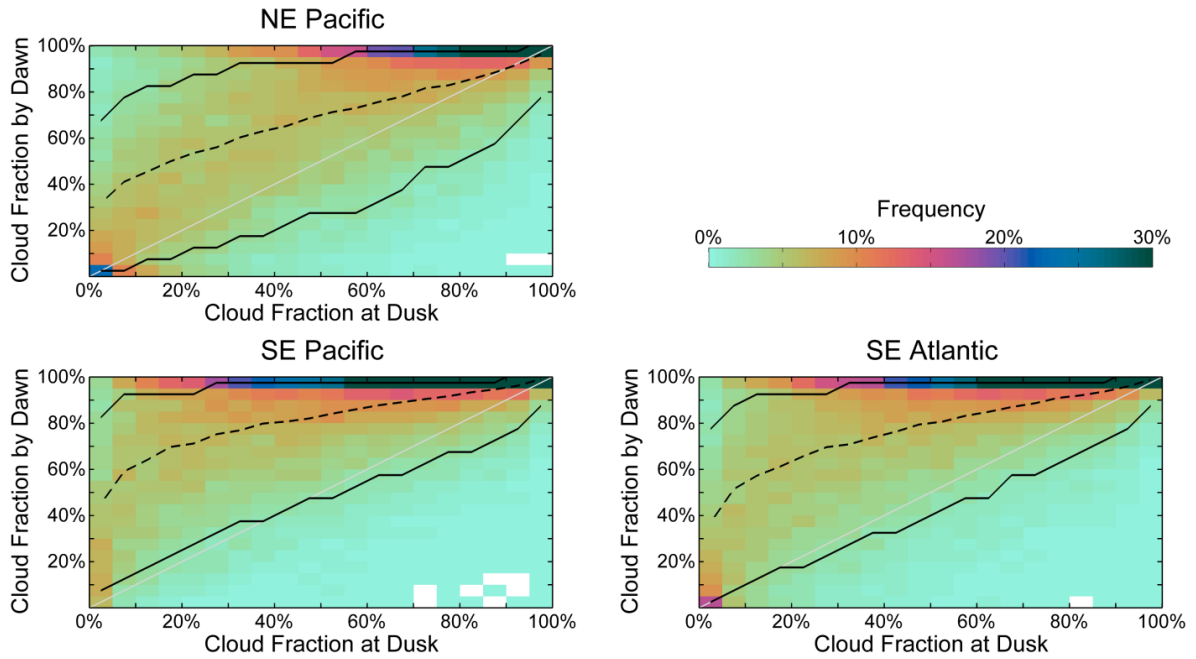


Figure 3.26. Data density diagrams showing the distribution of cloud fraction at dawn (y-axis) conditioned on the cloud fraction at dusk (x-axis). Cloud fractions are calculated in the $3^\circ \times 3^\circ$ boxes shown in Fig. 3.10. Darker colors indicate more frequent occurrences. In all panels the solid black lines indicate the 10th and 90th percentiles of the change distribution for a given starting cloud fraction while the dotted black line indicates the mean.

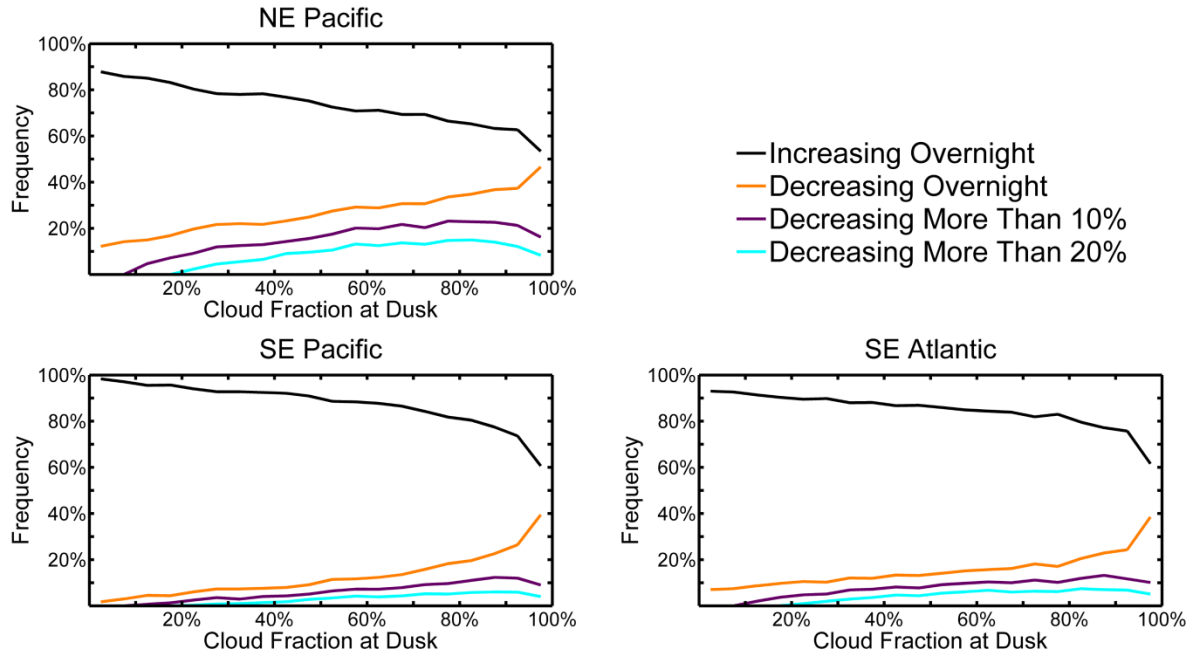


Figure 3.27. Frequency of cloud fraction changes overnight conditioned on the cloud fraction at dusk (x-axis). Cloud fractions are calculated in the $3^\circ \times 3^\circ$ boxes shown in Fig. 3.10.

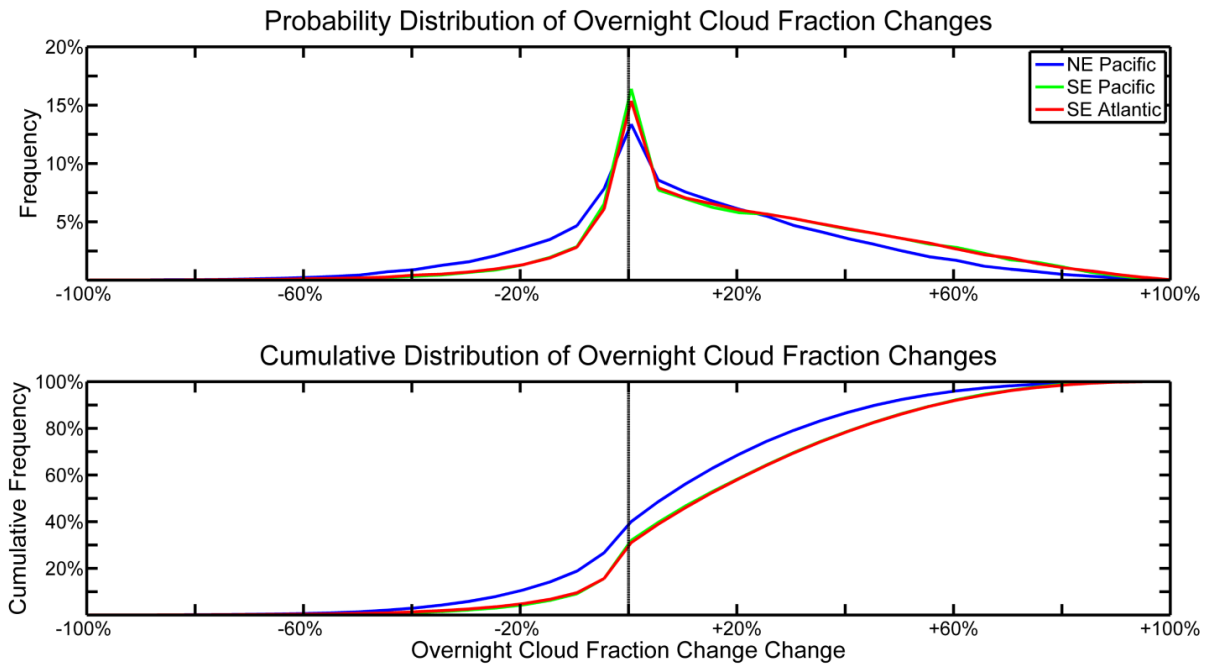


Figure 3.28. Probability (top) and cumulative (bottom) distribution plots of the change in cloud fraction overnight in the NE Pacific (blue line), SE Pacific (green line), and SE Atlantic (red line). Cloud fractions are calculated in the $3^\circ \times 3^\circ$ boxes shown in Fig. 3.10.

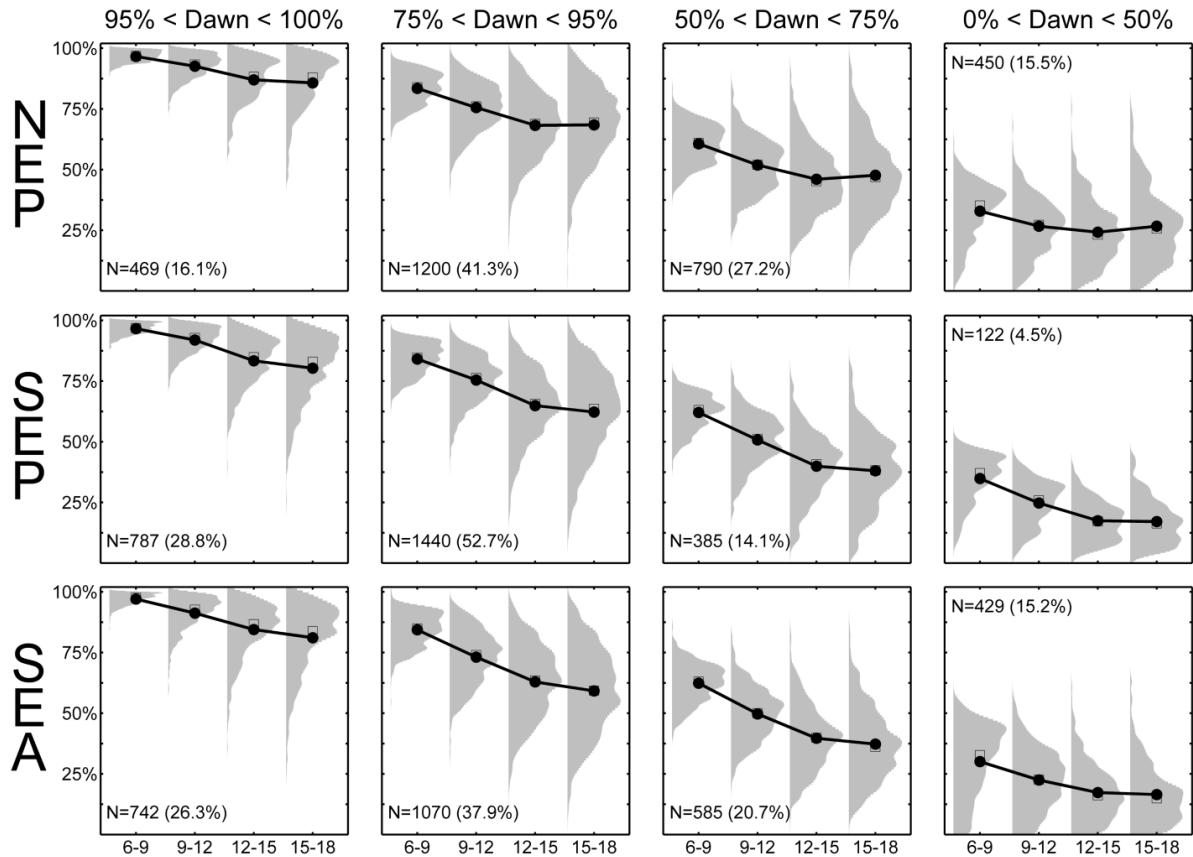


Figure 3.29. Distributions of cloud fraction in three hour time windows after dawn for mean cloud fractions at dawn (5:00 am – 6:00 am) greater than 95% (far left column), between 75% and 95% (center left column), between 50% and 75% (center right column), and less than 50% (far right column). Data are shown for the NE Pacific (top row; [132.5°W:122.5°W, 17.5°N:27.5°N]), SE Pacific (middle row, [87.5°W:77.5°W, 22.5°S:12.5°S]), and SE Atlantic (bottom row, [2.5°W:7.5°E, 20°S:10°S]). For each distribution the open square shows the median value while the filled circle shows the mean value.

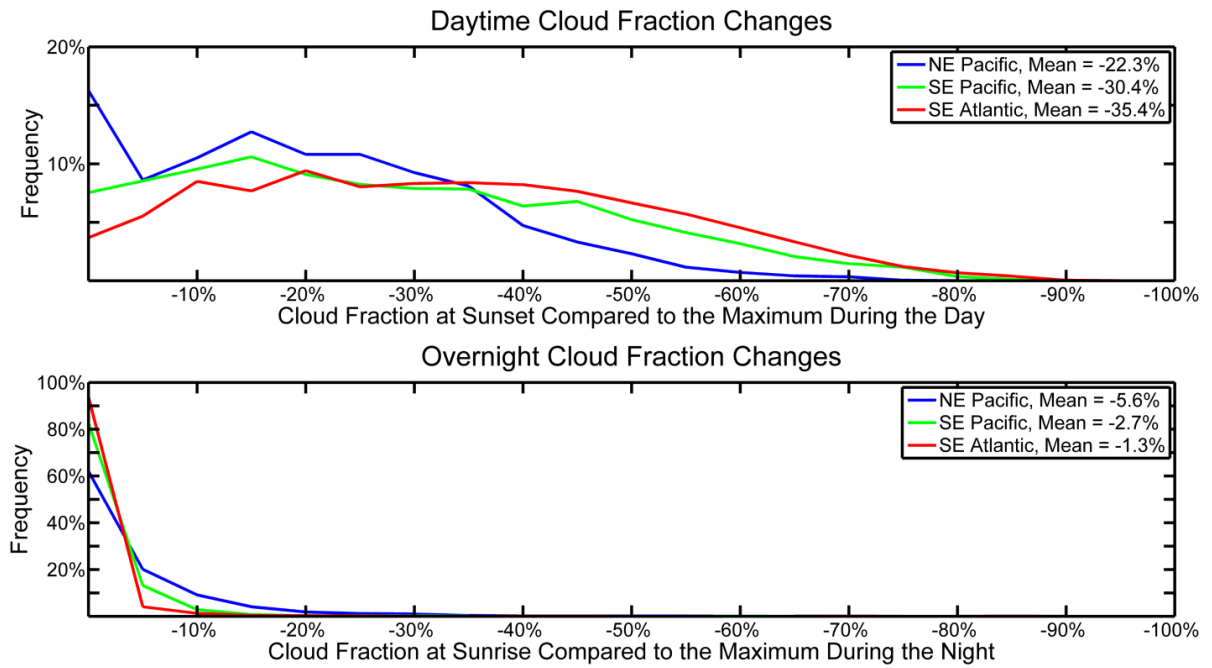


Figure 3.30. The distribution of total cloud fraction at sunset compared to the maximum total cloud fraction at any point during the day (top) and the distribution of cloud fraction at sunrise compared to the maximum total cloud fraction at any point overnight (bottom).

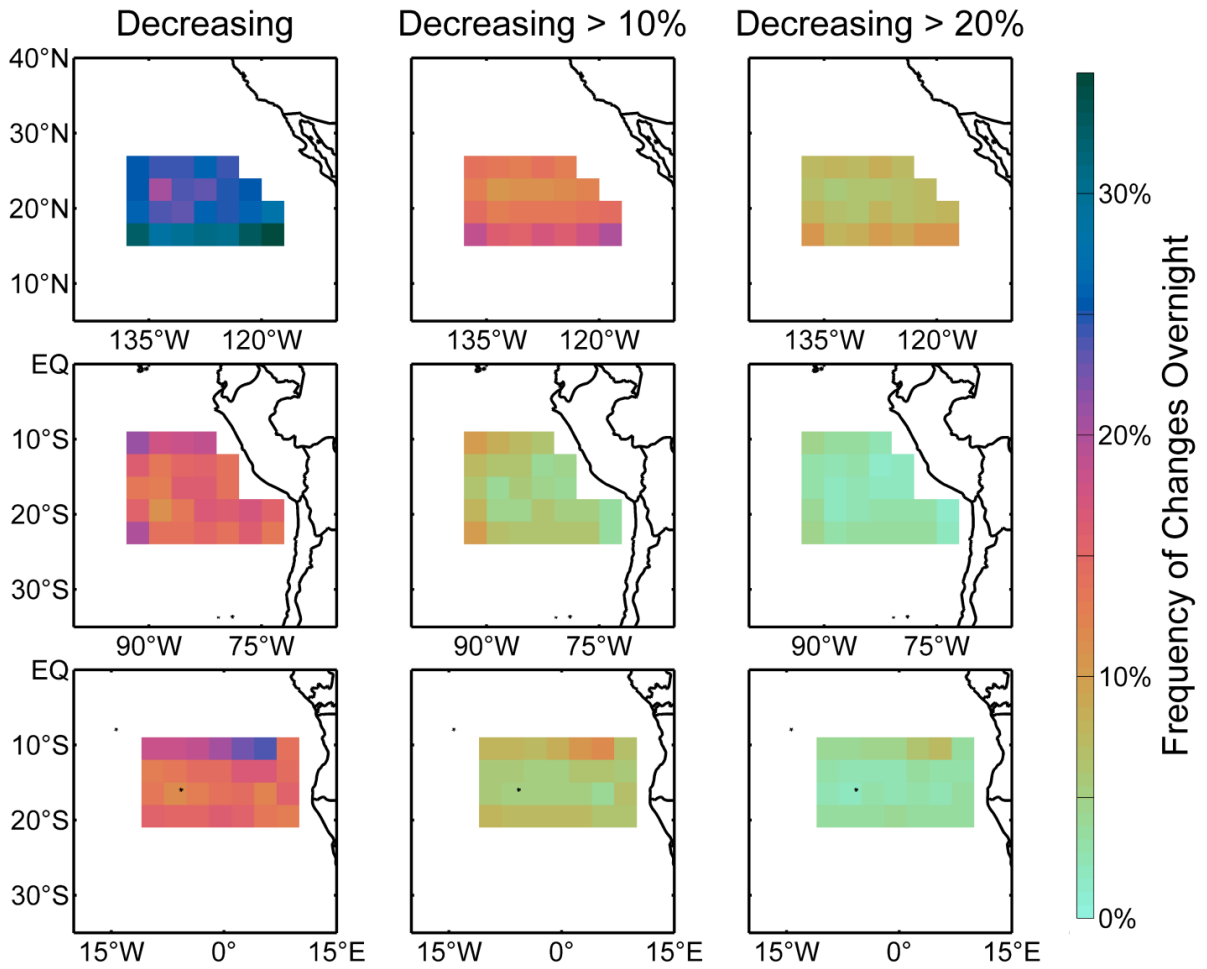


Figure 3.31. Frequency of cloud fraction decreasing (left column), decreasing more than 10% (center column), and decreasing more than 20% (right column) overnight in the NE Pacific (top row), SE Pacific (middle row), and SE Atlantic (bottom row).

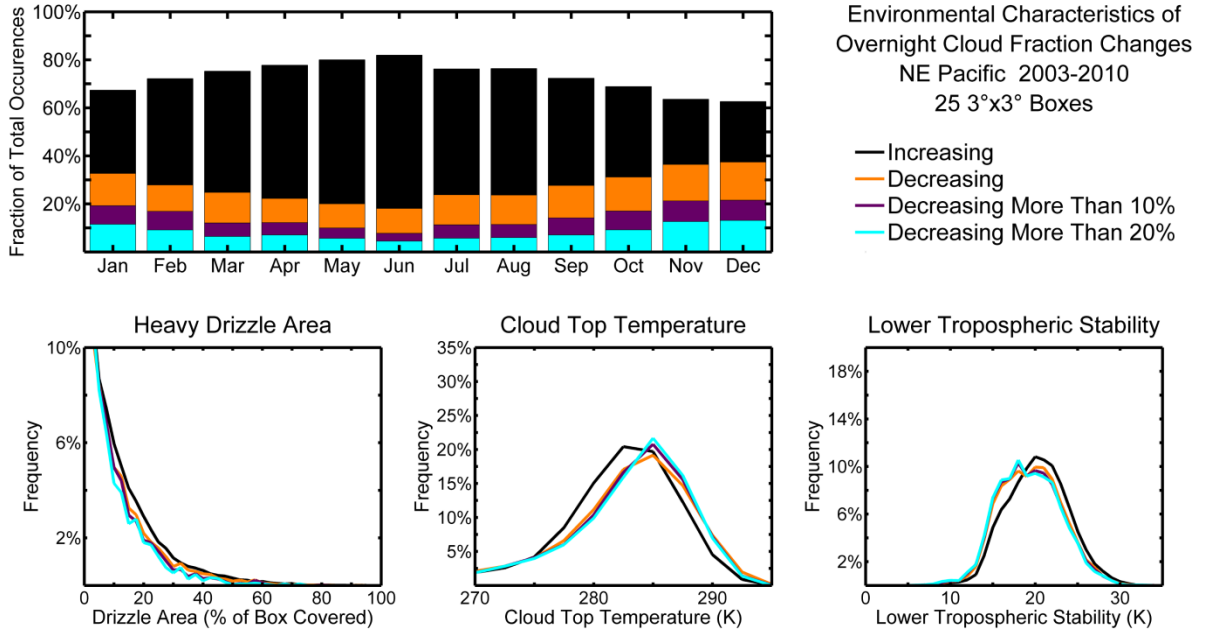


Figure 3.32. Top Row – Fraction of all overnight time series that have a net overnight increase in cloud fraction (black bars), net decrease (orange bars), net decrease greater than 10% (purple bars), and net decrease greater than 20% (cyan bars). Bottom Row – The distribution of drizzle area (bottom left), cloud top temperature (bottom center), and lower tropospheric stability (bottom right) for time series that have a net increase (black lines), net decrease (orange lines), net decrease greater than 10% (purple lines), and net decrease greater than 20% (cyan lines). Data are from 25 3° x 3° boxes in the NE Pacific.

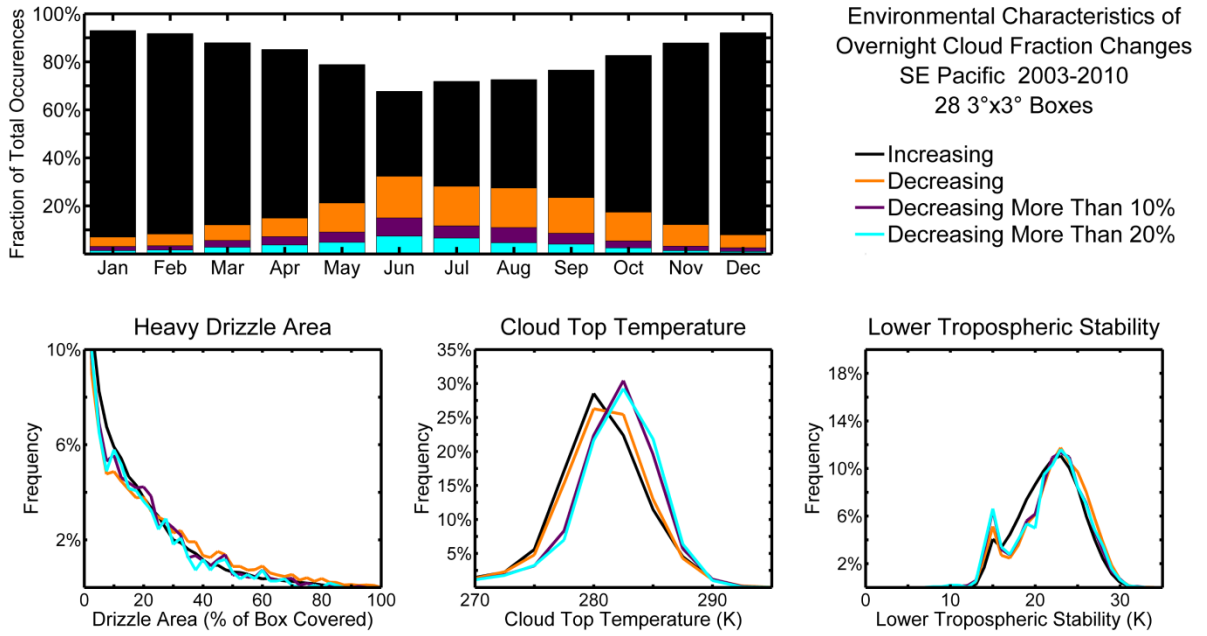


Figure 3.33. As in Figure 3.32 but for 28 3° x 3° boxes in the SE Pacific.

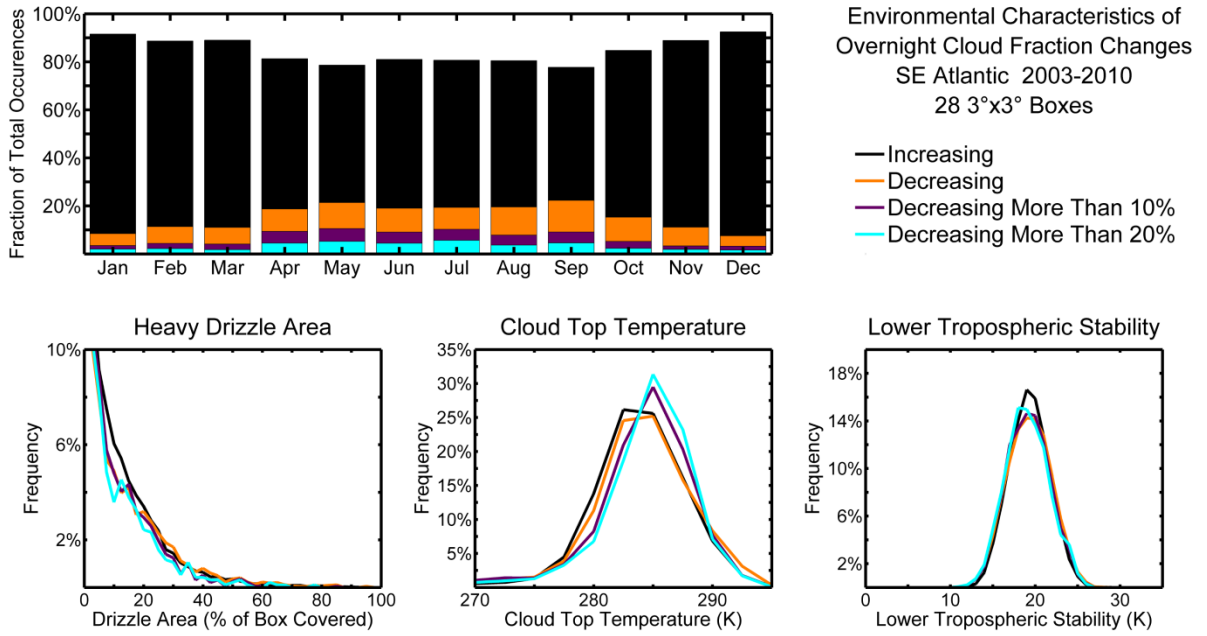


Figure 3.34. As in Figure 3.32 but for 28 3° x 3° boxes in the SE Pacific.

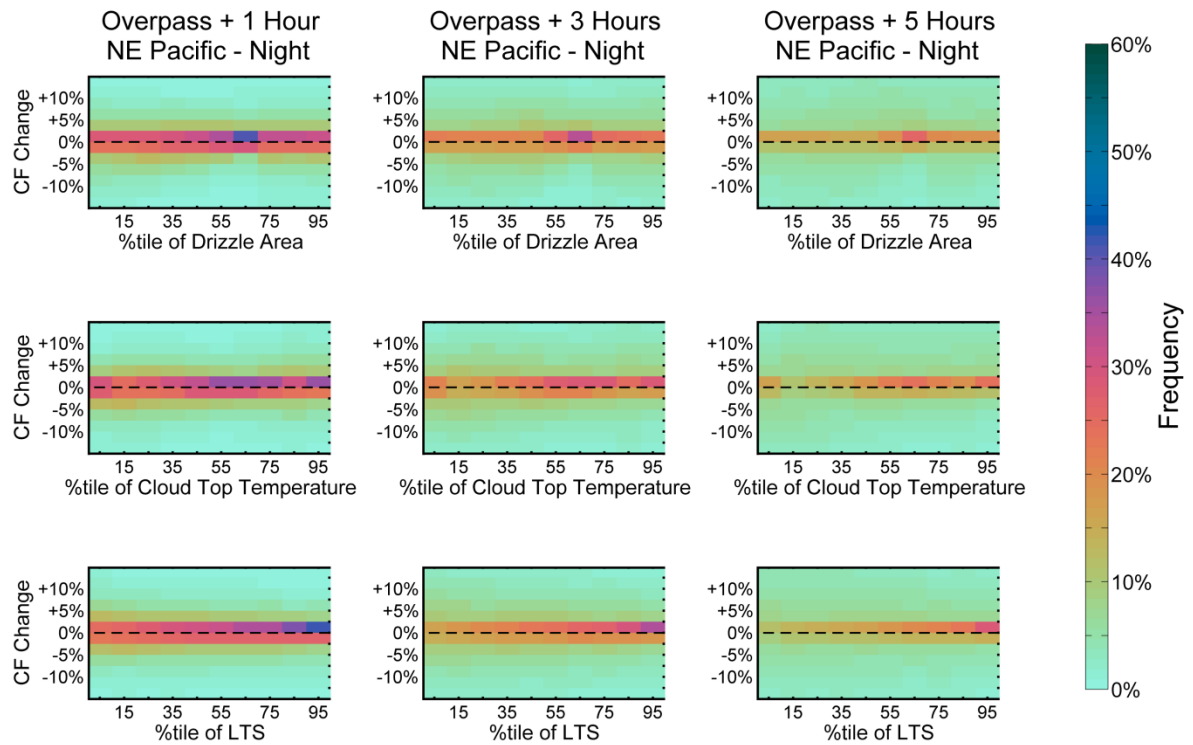


Figure 3.35. The frequency distribution of changes in low cloud fraction 1 hour (left column), 3 hours (center column), and 5 hours (right column) after a MODIS overpass. The frequency distributions are conditioned on the value on the x-axis. On each x-axis we show the percentile of a given environmental variable observed for the same $3^\circ \times 3^\circ$ box. The top row shows the sensitivity to drizzle area, the middle row shows the sensitivity to cloud top temperature (low percentiles are shallow clouds and high percentiles are deeper clouds), and the bottom row shows the sensitivity to lower tropospheric stability.

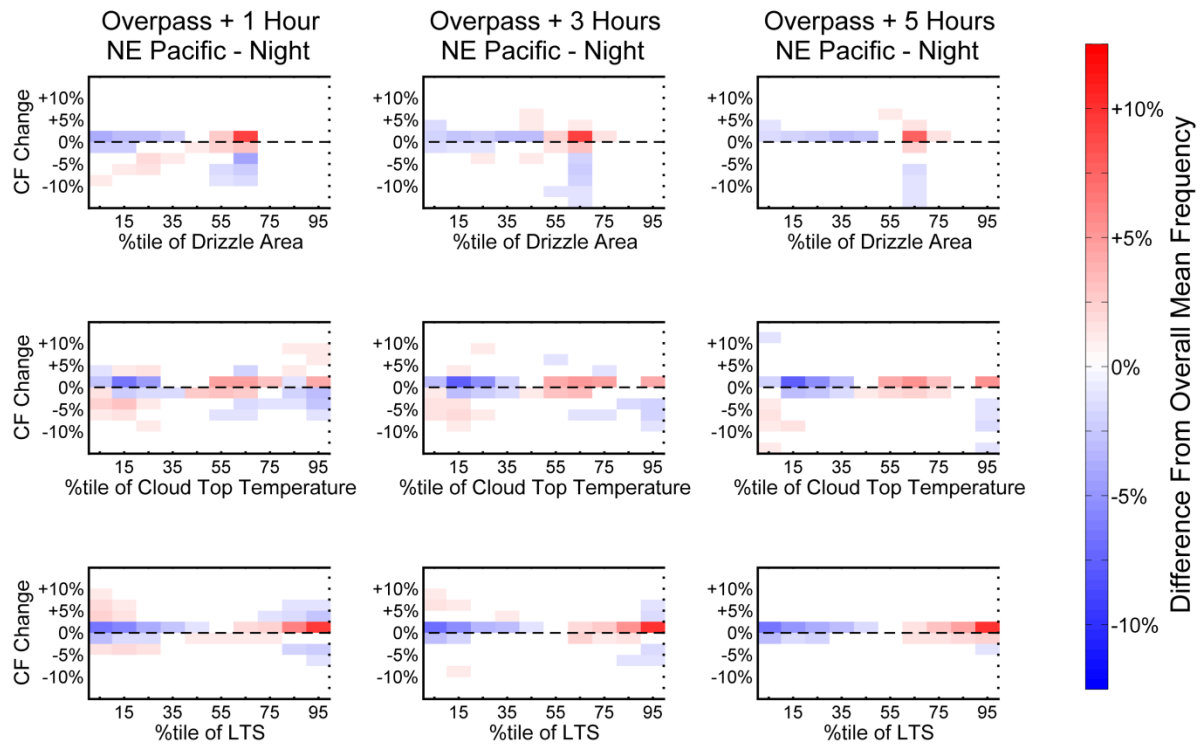


Figure 3.36. Each plot contains the same underlying data in Figure 3.35 but with the overall mean cloud fraction change distribution subtracted out. This shows the deviation from the mean value with red indicating more frequent than the overall mean and blue showing less frequent than the overall mean.

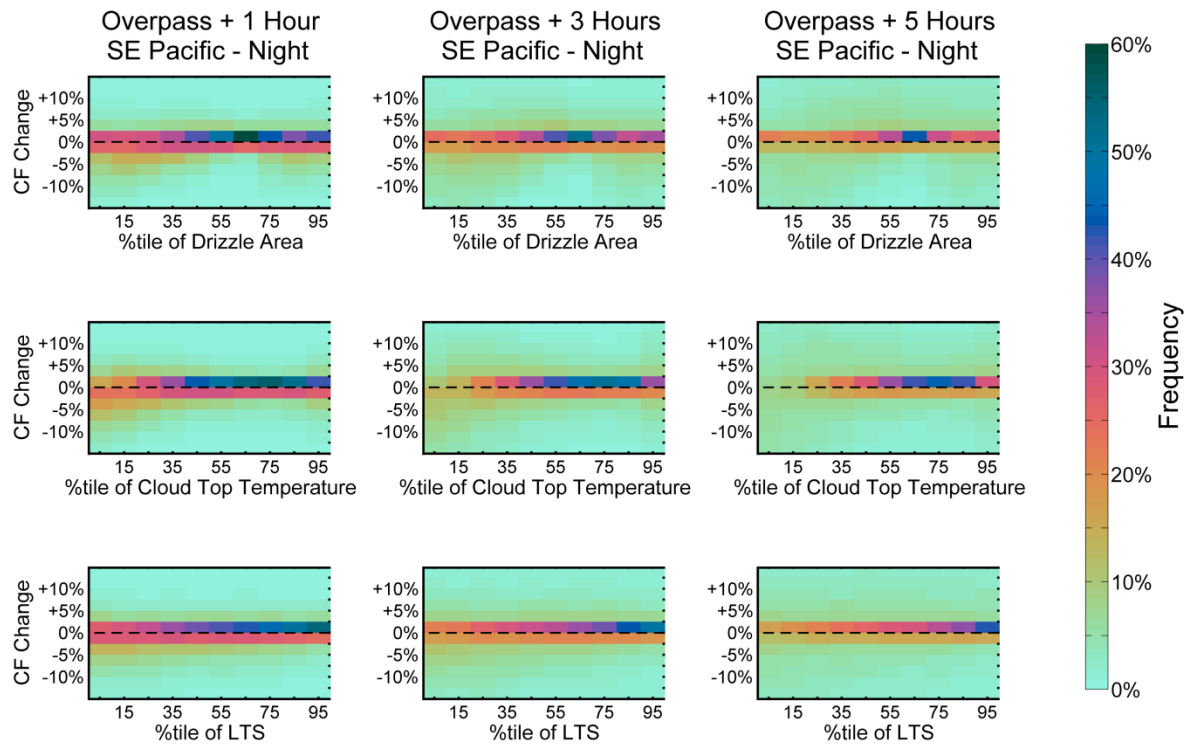


Figure 3.37. As in Figure 3.35 but for the SE Pacific.

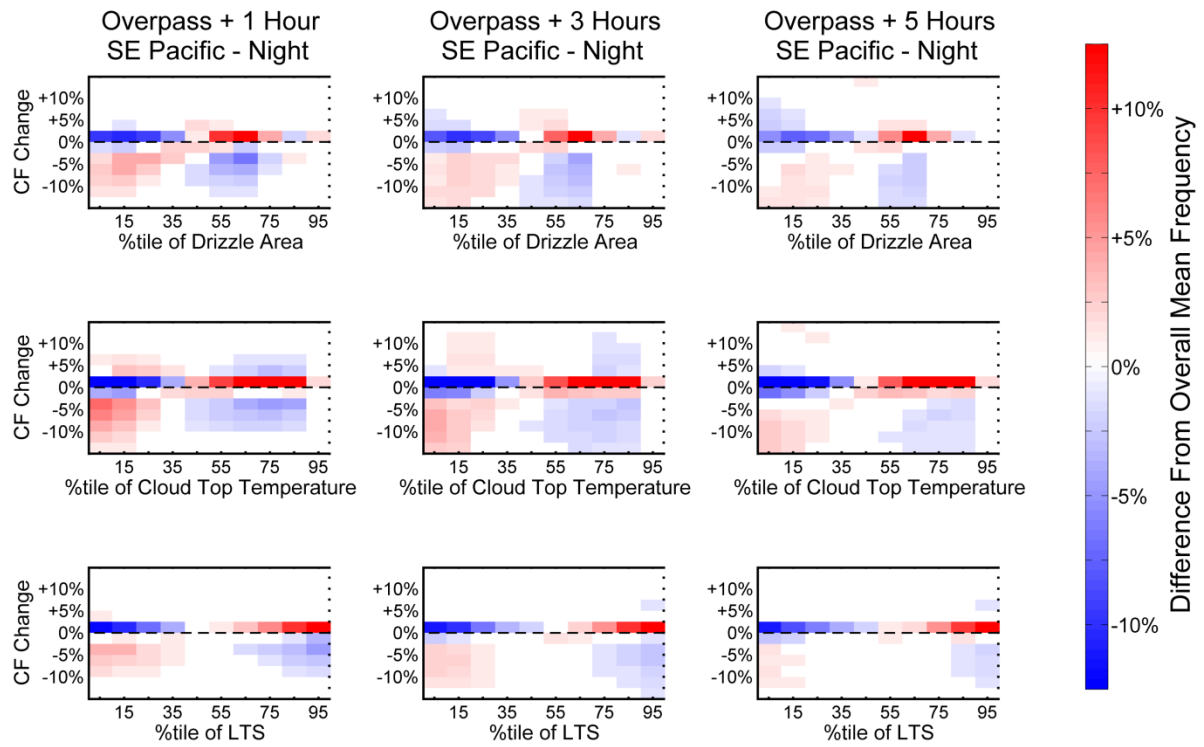


Figure 3.38. As in Figure 3.36 but for the SE Pacific.

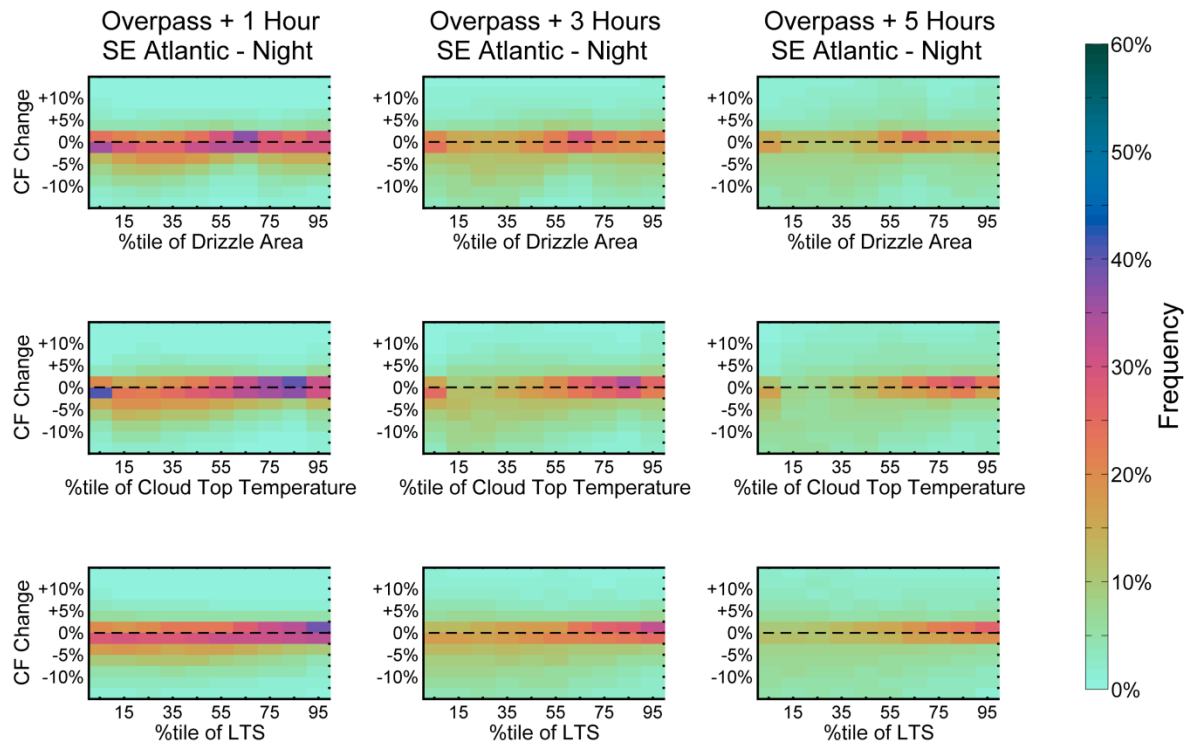


Figure 3.39. As in Figure 3.35 but for the SE Atlantic.

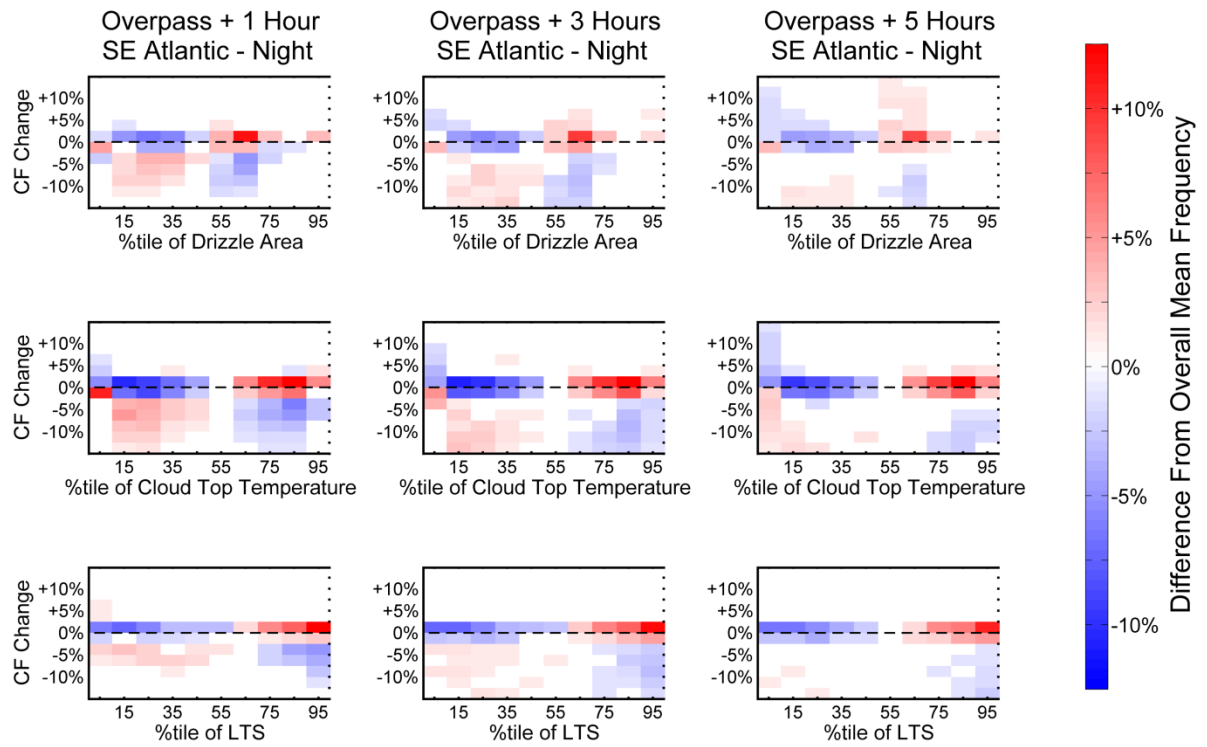


Figure 3.40. As in Figure 3.36 but for the SE Atlantic.

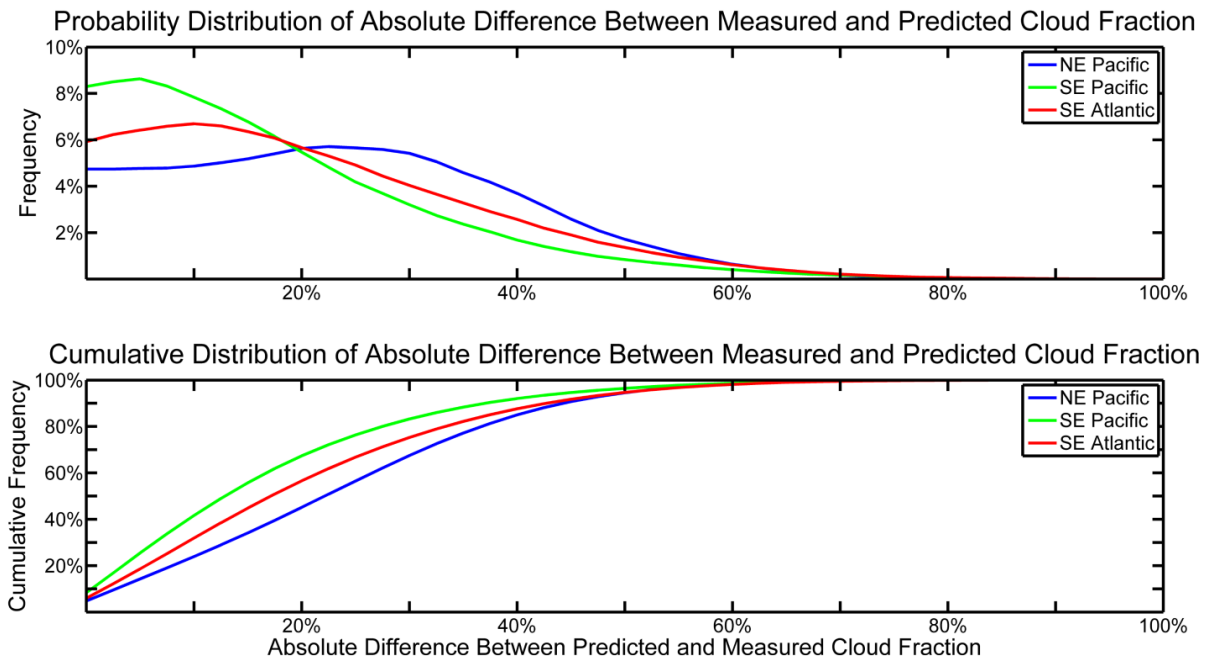


Figure 3.41. Probability (top) and cumulative (bottom) distributions of the absolute difference between the measured cloud fraction and that predicted by a simple model that predicts cloud fraction based solely on time of day and the day of the year. Cloud fractions are calculated every 30 minutes in the $3^\circ \times 3^\circ$ boxes shown in Fig. 3.10. Data are shown for the NE Pacific (blue line), SE Pacific (green line), and SE Atlantic (red line).

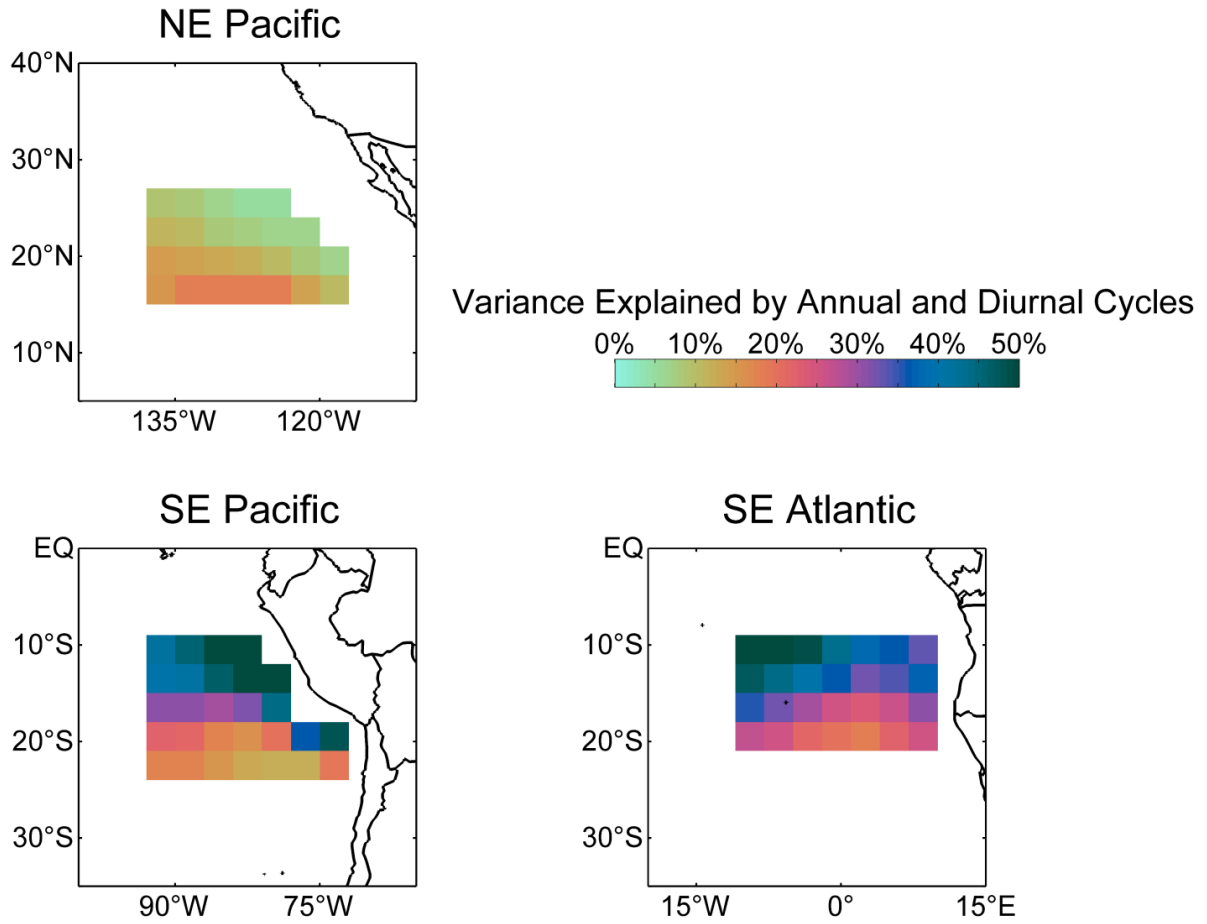


Figure 3.42. Percent of the total variance explained by a simple model that predicts cloud fraction based on the time of day and day of year. Cloud fractions are calculated in the 3° x 3° boxes shown in Fig. 3.10.

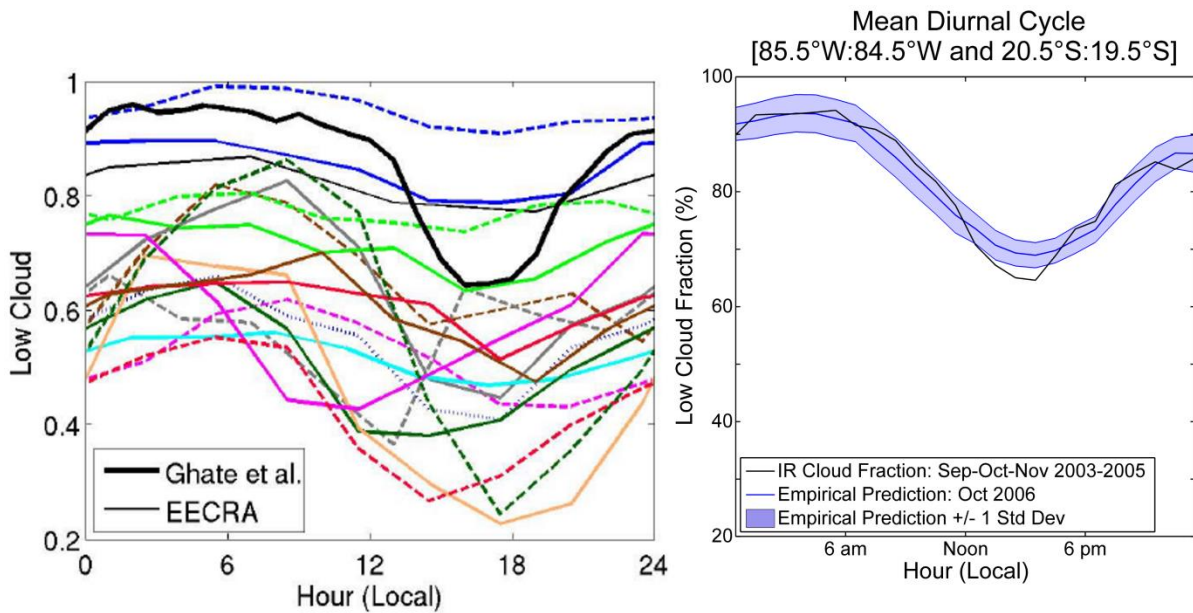


Figure 3.43. Left – Figure 11b from Wyant et al. (2010) showing the mean diurnal cycle in various GCMs (colored and dashed lines) and from point measurements of longwave radiative flux from an ocean buoy at 85°W and 20°S (black line). The buoy cloud fractions are the mean value during September-October-November from 2001-2005. Right – The mean merged-IR cloud fraction calculated over the buoy in September-October-November from 2003-2005 (black line) and the predicted cloud fraction (blue line). Cloud fractions were predicted using a multivariate polynomial regression, built only from values for the time of day and the day of the year, based on all available data from 2003-2010.

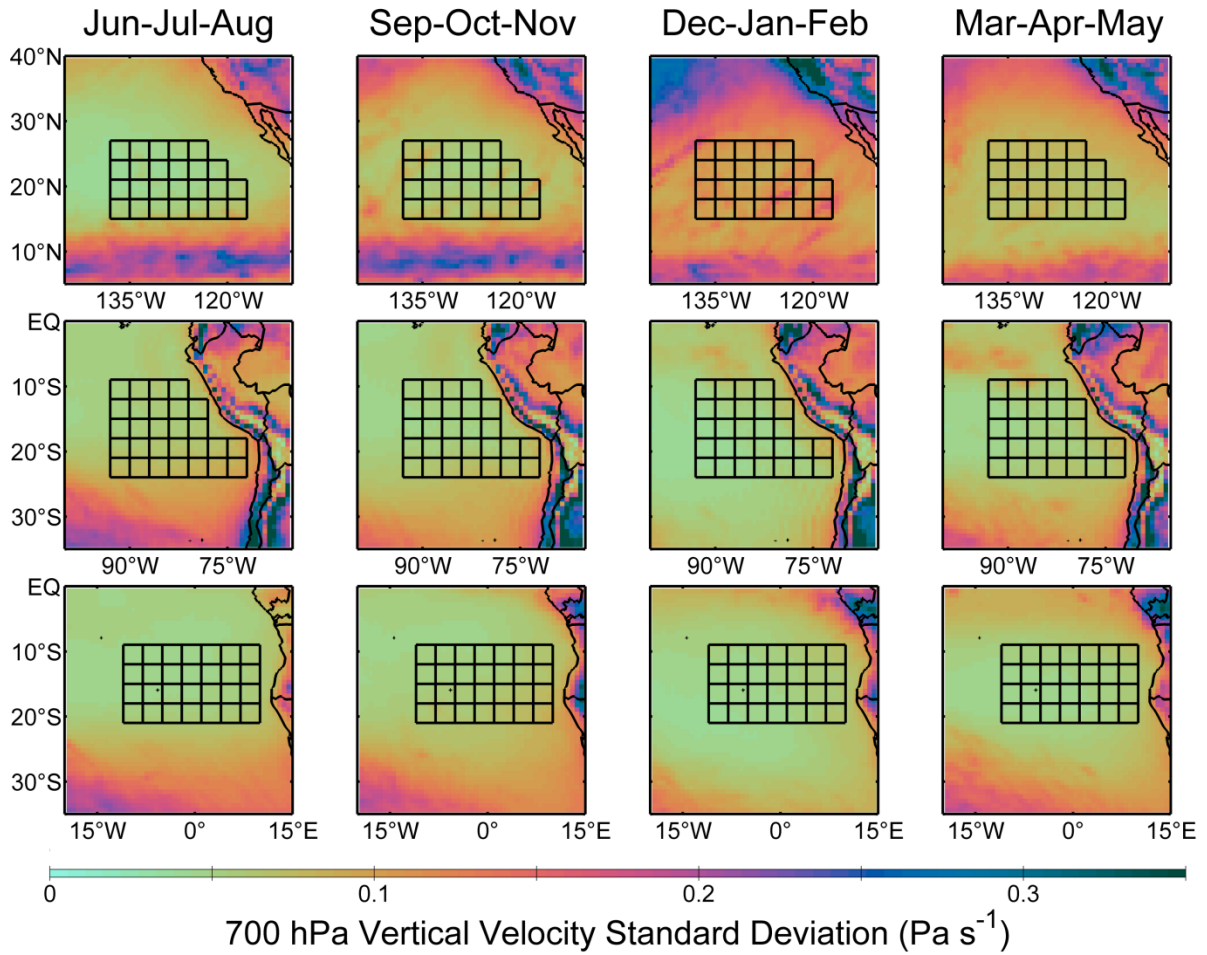


Figure 3.44. Standard deviation of the 700 hPa vertical velocity from ECMWF reanalysis for each season (column) in the NE Pacific (top row), SE Pacific (middle row), and SE Atlantic (bottom row). Black lines outline the 3° x 3° boxes in which low cloud fraction was calculated and are the same as in Fig. 3.10.

Chapter 4

Conclusions and Future Work

4.1 Conclusions

The drive to understand the processes leading to liquid phase cloud formation and dissipation is the underlying motivation behind most stratocumulus work. Understanding these processes is critical to correctly simulating stratocumulus clouds in GCMs and capturing their radiative impact on the climate system. It is not enough to capture the current patterns of cloud variability like one can do with an empirical parameterization. We need to get the processes correct in order to have confidence in the behavior of stratocumulus in GCM simulations of future climates. Examples of statements that outline the need to correctly simulate controlling processes in stratocumulus-topped boundary layers can be found in the beginning of papers dating back several decades. For example, Nicholls (1984) states in his introduction: “The presence of long-lived areas of stratocumulus substantially alters the nature of this [the radiative balance] interaction compared to the clear sky case. However, the dynamics of such cloud layers are surprisingly little understood and, in consequence, forecasting their evolution is particularly uncertain.” Similar statements are found in contemporary papers as well. In his review of the current state of knowledge about stratocumulus clouds Wood (2012) says: “Understanding why, where, when, and how stratocumuli form, and being able to quantify their properties, therefore constitutes a fundamental problem in the atmospheric sciences.”

In the 28 years between the writing of these two papers the community has learned much more about the how, when, where, and why of stratocumulus clouds. This knowledge has been developed via field campaigns, satellites, high-resolution models, GCMs, and basic theory. As outlined in the beginning of Chapter 3, some pieces of the system are well understood. These include the processes leading to variability on annual and diurnal time

scales. The relationship between the seasonal cycles of cloudiness and stability can be traced at least as far back as Klein and Hartmann (1993). Our understanding of the diurnal cycle goes back further. Connections between the diurnal variability of cloud-topped boundary layers and cloud-top radiative balance can be found in James (1959), Lilly (1968), and were clearly stated in Nicholls (1984). The primary contribution of new work that examines variability on annual and diurnal time scales, for example – my paper on the diurnal cycle presented in Chapter 2, is the refinement of the details of these processes.

In the past decade, many more processes have been connected to variations in stratocumulus cloud fraction. As in numerous other fields, new observational platforms and the development of modeling techniques lead to the discovery of finer details of a given system. The origin of many of these connections can be traced to the EPIC and DYCOMS II campaigns in 2001 which generated for the first time simultaneous observations of stratocumulus precipitation, entrainment rates, aerosol concentrations, and the structure of vertical mixing (Stevens et al. 2003; Bretherton et al. 2004). These programs also led to the discovery and popularization of POCs (Bretherton et al. 2004; Stevens et al. 2005a). In the past decade the community has connected precipitation, aerosols, gravity waves, and density currents to POCs (for example - Stevens et al. 2005a; Allen et al. 2012; Terai 2011). The formation and maintenance of POCs was one of the primary motivating questions behind the funding of the VOCALS program (Wood et al. 2011a).

The challenge of modeling the complex stratocumulus-topped boundary layer system has increased as more and more variables are connected to cloud fraction. LES simulations of stratocumulus clouds now have multi-moment bin microphysics, aerosol chemistry packages, internal radiative transfer models, and complex turbulence schemes (e.g. Xue et al. 2007; Bretherton and Park 2008; Savic-Jovicic and Steven 2008; Berner et al. 2003; etc.). Many processes within LES models cannot be resolved in GCMs so more and more intricate parameterization schemes are being designed to account for them. Despite increasing complexity, GCMs (and to a lesser degree LES models) often fail to generate accurate

stratocumulus cloud fractions, cloud thicknesses, or even inversion heights (for example - Abel et al. 2010; Wyant et al. 2010; Medeiros et al. 2012). The community has failed to reach a consensus on why these basic cloud characteristics are not being accurately predicted.

At least part of the problem in deciding where to focus the efforts of the stratocumulus community lies in the fact that it is very difficult to separate the impact of different processes. Processes interact with each other, have positive and negative feedbacks on cloud fraction, and vary on a wide range of temporal and spatial scales. No one dataset can capture all the sources of variability. For example, LES models can replicate many aerosol-cloud-precipitation interactions over multiday runs, but computational limitations limit run-time so the impact of these processes cannot be compared to parameters such as stability which vary over weeks and months. To limit the complications from interactions among processes, many modeling and observational studies are sensitivity studies designed to isolate a specific process. For example, some LES studies are only at night or use diurnally-averaged insolation because the diurnal cycle interferes with the models' ability to reproduce complex aerosol-cloud-precipitation interactions (for example – Bretherton and Wyant 1997; Berner et al. 2013). The research flights conducted during VOCALS-REx were also largely at night so the rich dataset generated cannot be compared across the diurnal cycle (Wood et al. 2011a).

My work in Chapter 3 was to a large degree motivated by the drive to put the various processes into context with each other. I was seeking a way to examine *relative* importance of different processes in modifying the stratocumulus-topped boundary layer system. The merged-IR cloud identification dataset allowed me to some degree to do this. Having high resolution cloud maps at 30 minute intervals allowed for the investigation of cloud fraction variability on a wide range of spatial and temporal scales. The data show that the primary modes of variability occur on annual and diurnal time scales. Large deviations from the mean annual and diurnal cycles happen in a small fraction of the cases examined (Fig. 3.27). While we made no attempt to explicitly characterize or identify POC events, we used overnight

deviations from the basic diurnal cycle to infer information about their relative frequency. Visible and IR satellite data show that POCs do exist and the merged-IR data indicates that once formed they are resistant to closing up even overnight (Fig. 3.29). However, the frequency of POCs and their radiative impact must be evaluated in the context of other sources of variability. In 8 years of data from the SE Pacific and SE Atlantic, total low cloud fraction by sunrise had decreased more than 15% from its maximum overnight value less than 1% of the time (Fig. 3.30). By contrast, on an average day in these regions more than 30% of the cloud deck is removed by sunset. The mean daytime breakup of the cloud deck is an order of magnitude larger than the mean cloudiness decrease overnight. The diurnal march of increasing and decreasing cloudiness is clearly critical to the total changes of the system.

The physical pathway to reduce cloudiness during the day requires no complex interactions between precipitation and aerosols. Early work in stratocumulus explained diurnal variability in simple terms of an interaction between shortwave heating and longwave cooling at cloud top and how the balance between these two parameters leads to the presence or absence of turbulent mixing in the subcloud layer (James 1959; Lilly 1968; Nicholls 1984). This should not come as a surprise – stratocumulus clouds are after all boundary layer clouds. Like boundary layer systems everywhere else in meteorology they are strongly dependent on the sun. The results in Chapter 3 also show that variability on seasonal scales is in most cases at least as large as variability across the diurnal cycle (Fig. 3.15; Fig. 3.18). The physical causes for seasonal variability, changes in stability and inversion strength associated with the location and intensity of the Hadley circulation, are also well established.

Chapter 3 closed with the analysis of a simple model which used only the time of day and the day of the year to predict cloud fraction in a given location. This model was able to explain up to 50% of the total variability present in the SE Atlantic and SE Pacific (Fig. 3.42). We also showed for one month the performance of our simple empirical model against GCMs (Fig. 3.43). The climate models included dozens of processes that we made no attempt to account for, yet were unable to match the accuracy of the simple empirical model.

I am not advocating a switch to empirical modeling for stratocumulus, but rather pointing out that if GCMs are not reproducing stratocumulus cloud fraction it seems much more likely that they are missing the processes responsible for diurnal and seasonal cycles rather than less important components such as aerosol-cloud-precipitation interactions. The results in Chapter 3 provide evidence that until GCMs correctly simulate the location and strength of the inversion and the relationship between boundary layer mixing and shortwave radiative flux they are very unlikely to produce clouds in the right place at the right time. Will simulations be perfect if they account for variability on these two time scales? No. Complete fidelity between the models and observations will likely require the simulation of a wider range of processes that can modify cloudiness. I believe however that the evidence shows the greatest improvement in models will come from correctly simulating seasonal and diurnal cycles.

Chapter 3 also demonstrates the importance of including the diurnal cycle in even short term simulations of stratocumulus clouds. In many papers involving LES or other high-resolution simulations there is a conscious decision to turn off or average solar insolation (for example – Bretherton and Wyant 1997; Berner et al. 2013) or to only run simulations at night (for example – Wang and Feingold 2009; Feingold et al. 2010; Mechem et al. 2012). It seems this is largely due to the fact that it is difficult to evaluate individual processes when they are being constantly modified by the background diurnal cycle. Turning off the diurnal cycle of solar insolation, one of the largest sources of variability within the system, can lead to confusion about how the processes being examined function in the real world. It also sets up situations where conclusions are developed based off of model designs that do not actually exist in nature. For example, the widely cited simulations of Bretherton and Wyant (1997) used diurnally averaged solar insolation over a period of six days. The deepening-warming decoupling they described would, in a simulation containing a diurnal cycle of solar insolation, be modified to an unknown degree by the natural diurnal decoupling that takes place in the stratocumulus-topped boundary layer system. Likewise, Berner et al. (2013) performed most of their sensitivity simulations of the aerosol-cloud-precipitation interactions

that lead to POC formation with a constant diurnally averaged solar insolation for runs out to 20 days. In the simulations where they added a diurnal cycle of solar insolation, the diurnal cycle dominated the variability of the system and their mechanism of POC formation did not occur. More attention should be paid to cases like this where the importance of the diurnal cycle is clearly shown. In order to fully understand the role of each process they should be evaluated in the context of the diurnal cycle.

4.2 Future Work

The merged-IR cloud identification dataset creates many opportunities for further exploration of the stratocumulus system. It can and should also be used for model evaluation. The results in Chapter 3 outline two main avenues that should be explored further. We could use observational data from field campaigns combined with merged-IR cloud fractions to explore the environmental conditions where cloudiness decreases overnight. In this study we used the nighttime MODIS overpass along with reanalysis data to characterize the environment. This has obvious flaws. A single data point from a satellite overpass does not give information about the trends in environmental conditions and a measurement at 1:30 am takes place after hours of cloudiness changes after sunset. Observational data from field campaigns would give many samples during the course of a single night. Additionally, other data sources (especially upper-air soundings, lidar, and cloud radars) would allow us to characterize aspects of the environment, for example cloud depth and boundary layer mixing, that are tougher to measure from satellites. We could also use the reanalysis dataset to take a closer look at synoptic variability in the NE Pacific. Initial efforts were unsuccessful at trying to connect environmental variables that could be used as a proxy for synoptic variability, for example 500 hPa heights, to deviations from the base diurnal cycle in the NE Pacific. Further work using filtered time series in which we focus on variability on weekly time scales might be more successful. Getting more information on the relationship between synoptic variability and stratocumulus cloud fraction will provide better targets for modelers to focus on.

REFERENCES

- Abel, S. J., D. N. Walters, and G. Allen, 2010: Evaluation of stratocumulus cloud precipitation in the Met Office forecast model during VOCALS-REx. *Atmos. Chem. Phys.*, **10**, 10541-10559, doi:10.5194/acpd-10-10541-2010.
- Albrecht, B. A., 1989: Aerosols, cloud microphysics, and fractional cloudiness. *Science*, **245**, 1227-1230.
- Allen, G., and Coauthors, 2012: South east Pacific atmospheric composition and variability sampled along 20°S during VOCALS-REx. *Atmos. Chem. Phys.*, **11**, 5237-5262, doi: 10.5194/acp-11-5237-2011.
- Atkinson, B. W., and J. W. Zhang, 1996: Mesoscale shallow convection in the atmosphere. *Rev. Geophys.*, **34**, 403-431.
- Bennartz, R., 2007: Global assessment of marine boundary layer cloud droplet number concentration from satellite. *J. Geophys. Res.*, **112**, D02201, doi:10.1029/2006JD007547.
- Berner, A. H., C. S. Bretheron, R. Wood, and A. Muhlbauer, 2013: Marine boundary layer cloud regimes and POC formation in an LES coupled to a bulk aerosol scheme. *Atmos. Chem. Phys. Discuss.*, **13**, 18143-18203, doi:10.5194/acpd-13-18143-2013.
- Betts, A. K., 1990: Diurnal variation of California coastal stratocumulus from two days of boundary layer soundings. *Tellus*, **42A**, 302-304.

Bony, S., and J.-L. Dufresne, 2005: Marine boundary layer clouds at the heart of tropical cloud feedback uncertainties in climate models. *Geophys. Res. Lett.*, **32**, L20806, doi:10.1029/2005GL023851.

Bony, S., and Coauthors, 2006: How well do we understand and evaluate climate change feedback processes? *J. Climate*, **19**, 3445-3482.

Boutle, I. A., and S. J. Abel, 2012: Microphysical controls on the stratocumulus topped boundary-layer structure during VOCALS-REx. *Atmos. Chem. Phys.*, **12**, 2849-2863, doi:10.5194/acp-12-2849-2012.

Bretherton, C. S., and M. C. Wyant, 1997: Moisture transport, lower-tropospheric stability, and decoupling of cloud-topped boundary layers. *J. Atmos. Sci.*, **54**, 148-167.

Bretherton, C. S., and Coauthors, 2004: The EPIC 2001 stratocumulus study. *Bull. Amer. Meteor. Soc.*, **85**, 976-977.

Bretherton, C. S., R. Wood, R. C. George, D. Leon, G. Allen, and X. Zheng, 2010: Southeast Pacific stratocumulus clouds, precipitation and boundary layer structure along 20°S during VOCALS-REx. *Atmos. Chem. Phys.*, **10**, 10639-10654, doi:10.5194/acp-10-10639-2010.

Bretherton, C. S., and S. Park, 2008: A new moist turbulence parameterization in the Community Atmosphere Model. *J. Climate*, **22**, 3422-3448.

Burleyson, C. D., S. P. de Szoeke, S. E. Yuter, M. Wilbanks, and W. A. Brewer, 2013: Ship-based observations of the diurnal cycle of southeast Pacific marine stratocumulus clouds and precipitation. *J. Atmos. Sci.*, In-Press.

Caldwell, P., R. Wood, and C. S. Bretherton, 2005: Mixed-layer budget analysis of the diurnal cycle of entrainment in southeast Pacific stratocumulus. *J. Atmos. Sci.*, **62**, 3775-3791.

Clement, A. C., R. Burgman, and J. R. Norris, 2009: Observational and model evidence for positive low-level cloud feedback. *Science*, **325**, 460-464.

Comstock, K. K., R. Wood, S. E. Yuter, and C. S. Bretherton, 2004: Reflectivity and rain rate in and below drizzling stratocumulus. *Quart. J. Roy. Meteor. Soc.*, **130**, 2891-2918.

Comstock, K. K., C. S. Bretherton, and S. E. Yuter, 2005: Mesoscale variability and drizzle in southeast Pacific stratocumulus. *J. Atmos. Sci.*, **62**, 3792-3807.

Comstock, K. K., S. E. Yuter, R. Wood, and C. S. Bretherton, 2007: The three-dimensional structure and kinematics of drizzling stratocumulus. *Mon. Wea. Rev.*, **135**, 3767-3784.

de Szoeke, S. P., C. W. Fairall, D. E. Wolfe, L. Bariteau, and P. Zuidema, 2010a: Surface flux observations on the southeastern tropical Pacific Ocean and attribution of SST errors in coupled ocean-atmosphere models. *J. Climate*, **23**, 4152-4174.

de Szoeke, S. P., S. E. Yuter, D. Mechem, C. W. Fairall, C. D. Burleyson, and P. Zuidema, 2012: Observations of stratocumulus and their effect on the eastern Pacific surface heat budget along 20°S. *J. Climate*, **25**, 8542-8567.

Duynkerke, P. G., 1989: The diurnal variation of a marine stratocumulus cloud: A model sensitivity study. *Mon. Wea. Rev.*, **117**, 1710-1725.

European Centre for Medium-Range Weather Forecasts (ECMWF), 2009: ERA-Interim Project. Research Data Archive at the National Center for Atmospheric Research, Computational and Information Systems Laboratory, Boulder, CO. [Available online at <http://rda.ucar.edu/datasets/ds627.0>.]

Feingold, G., I. Koren, H. Wang, H. Xue, and W. A. Brewer, 2010: Precipitation-generated oscillations in open cellular cloud fields. *Nature*, **466**, 849-852, doi:10.1038/nature09314.

Garreaud, R. D., and R. C. Muñoz, 2004: The diurnal cycle in circulation and cloudiness over the subtropical southeast Pacific: A modeling study. *J. Climate*, **17**, 1699-1710.

George, R. C., and R. Wood, 2010: Subseasonal variability of low cloud radiative properties. *Atmos. Chem. Phys.*, **10**, 4047-4063, doi:10.5194/acp-10-4047-2010.

Ghate, V., B. Albrecht, C. Fairall, and R. Weller, 2009: Climatology of surface meteorology, surface fluxes, cloud fraction, and radiative forcing over the south-east Pacific from buoy observations. *J. Climate*, **22**, 5527-5540.

Grund, C. J., R. M. Banta, J. L. George, J. N. Howell, M. J. Post, R. A. Richter, and A. M. Weickmann, 2001: High-Resolution Doppler Lidar for boundary layer and cloud research. *J. Atmos. Oceanic Tech.*, **18**, 376-393.

Hahn, C. J., and S. G. Warren, 2007: A gridded climatology of clouds over land (1971-96) and ocean (1954-97) from surface observations worldwide. Numeric Data Product NDP-026-E, Carbon Dioxide Information Analysis Center, Oak Ridge National Laboratory, Oak Ridge, Tennessee.

Hartmann, D. L., M. E. Ockert-Bell, and M. L. Michelson, 1992: The effect of cloud type on Earth's energy balance: Global analysis. *J. Climate*, **5**, 1281-1304.

Jaeglé, L., P. K. Quinn, T. S. Bates, B. Alexander, and J.-T. Lin, 2011: Global distribution of sea salt aerosols: new constraints from in situ and remote sensing observations. *Atmos. Chem. Phys.*, **11**, 3137–3157, doi:10.5194/acp-11-3137-2011.

James, D. G., 1959: Observations from aircraft of temperatures and humidities near stratocumulus clouds. *Quart. J. Roy. Meteor. Soc.*, **85**, 120-130.

Janowiak, J. E., R. J. Joyce, and Y. Yarosh, 2001: A real-time global half-hourly pixel-resolution infrared dataset and its applications. *Bull. Amer. Meteor. Soc.*, **82**, 205-217.

Jones, C. R., C. S. Bretherton, and D. Leon, 2011: Coupled vs. decoupled boundary layers in VOCALS-REx. *Atmos. Chem. Phys.*, **11**, 7143-7153, doi:10.5194/acp-11-7143-2011.

Joyce, R. J., and P. A. Arkin, 1994: Improved estimates of tropical and subtropical precipitation using the GOES Precipitation Index. *J. Atmos. Oceanic. Technol.*, **14**, 997-1011.

King, M. D., and Coauthors, 2003: Cloud, aerosol, and water vapor profiles from MODIS. *IEEE Trans. Geosci. Remote. Sens.*, **41**, 442-458.

Klein, S. A., 1997: Synoptic variability of low-cloud properties and meteorological patterns in the subtropical trade wind boundary layer. *J. Climate*, **10**, 2018-2039.

Klein, S. A., and D. L. Hartmann, 1993: The seasonal cycle of low stratiform clouds. *J. Climate*, **6**, 1587-1606.

Klein, S. A., D. L. Hartmann, and J. R. Norris, 1995: On the relationships among low-cloud structure, sea surface temperature, and atmospheric circulations in the summertime northeast Pacific. *J. Climate*, **8**, 1140-1155.

Leon, D. C., Z. Wang, and D. Liu, 2008: Climatology of drizzle in marine boundary layer clouds based on 1 year of data from CloudSat and Cloud-Aerosol Lidar and Infrared Pathfinder Satellite Observations (CALIPSO). *J. Geophys. Res.*, **113**, D00A14, doi:10.1029/2008JD009835.

Lewellen, D. C., and W. S. Lewellen, 1998: Large-eddy boundary layer entrainment. *J. Atmos. Sci.*, **55**, 2645-2665.

Lilly, D., 1968: Models of cloud-topped mixed layers under a strong inversion. *Quart. J. Roy. Meteor. Soc.*, **94**, 292-309.

Manabe, S., and R. F. Strickler, 1964: Thermal equilibrium of the atmosphere with a convective adjustment. *J. Atmos. Sci.*, **21**, 361-385.

Mechem, D. B., S. E. Yuter, and S. P. de Szoeke, 2012: Thermodynamic and aerosol controls in southeast Pacific stratocumulus. *J. Atmos. Sci.*, **69**, 1250-1266.

Mechoso, C. R., and Coauthors, 2013: Ocean-Cloud-Atmosphere-Land Interactions in the Southeastern Pacific: The VOCALS Program. *Bull. Amer. Met. Soc.*, Submitted.

Medeiros, B., D. L. Williamson, C. Hannay, and J. G. Olson, 2012: Southeast Pacific stratocumulus in the Community Atmosphere Model. *J. Climate*, **25**, 6175-6192.

Miller, M. A., and S. E. Yuter, 2013: Detection and characterization of heavy drizzle cells within subtropical marine stratocumulus using AMSR-E 89-GHz passive microwave measurements. *Atmos. Meas. Tech.*, **6**, 1-13, doi:10.5194/amt-6-1-2013.

Miller, R. L., 1997: Tropical thermostats and low cloud cover. *J. Climate*, **10**, 409-440.

Moeng, C.-H., S. Shen, and D. A. Randall, 1992: Physical processes within the nocturnal stratus-topped boundary layer. *J. Atmos. Sci.*, **49**, 2384-2401.

Moran, K. P., S. Pezoa, C. Fairall, C. Williams, T. Ayers, A. Brewer, S. P. de Szoeke, and V. Ghate, 2011: A motion stabilized W-band radar for shipboard cloud observations and airborne studies of sea spray. *Bound.-Layer Meteor.*, **143**, 3–24.

Myers, T. A., and J. R. Norris, 2013: Observational evidence that enhanced subsidence reduces subtropical marine boundary layer cloudiness. *J. Climate*, **26**, 7507-7524.

Neiburger, M., D. S. Johnson, and C. W. Chien, 1961: Studies of the structure of the atmosphere over the eastern Pacific Ocean in summer: Part 1. The inversion over the eastern North Pacific Ocean. University of California Publ. in Meteorology, Vol. 1, University of California Press, 94 pp.

Nicholls, S., 1984: The dynamics of stratocumulus: Aircraft observations and comparisons with a mixed layer model. *Quart. J. Roy. Meteor. Soc.*, **110**, 783-820.

Nicholls, S., and J. Leighton, 1986: An observational study of the structure of stratiform cloud sheets: Part I. Structure. *Quart. J. Roy. Meteor. Soc.*, **112**, 431-460.

Nicholls, S., and J. D. Turton, 1986: An observational study of the structure of stratiform cloud sheets: Part II. Entrainment. *Quart. J. Roy. Meteor. Soc.*, **112**, 461-480.

Painemal, D., R. Garreaud, J. Rutllant, and P. Zuidema, 2010: Southeast Pacific stratocumulus: High-frequency variability and mesoscale structures over San Felix Island. *J. Appl. Met. Climatol.*, **49**, 463-477.

Painemal, D., P. Minnis, and L. O'Neill, 2013: The diurnal cycle of cloud top height and cloud cover over the Southeast Pacific as observed by GOES-10. *J. Atmos. Sci.*, **70**, 2393-2408, doi:10.1175/jas-d-12-0325.1.

Pincus, R., and M. B. Baker, 1994: Effect of precipitation on the albedo susceptibility of clouds in the marine boundary layer. *Nature*, **372**, 250-252.

Platnick, S., M. D. King, S. A. Ackerman, W. P. Menzel, B. A. Baum, and R. A. Frey, 2003: The MODIS cloud products: Algorithms and examples from Terra. *IEEE Trans. Geosci. Remote Sens.*, **41**, 459-473.

Rahn, D. A., and R. D. Garreaud, 2010: Marine boundary layer over the subtropical southeast Pacific during VOCALS-REx – Part I: Mean structure and diurnal cycle. *Atmos. Chem. Phys.*, **10**, 4491-4506, doi:10.5194/acp-10-4491-2010.

Randall, D., and Coauthors, 2007: Climate models and their evaluation. *Climate Change 2007: The Physical Science Basis*, S. Solomon et al. Eds., Cambridge University Press, 588-662.

Richter, I., and C. R. Mechoso, 2006: Orographic influences on subtropical stratocumulus. *J. Atmos. Sci.*, **63**, 2585-2601.

Rogers, D. P., X. Yang, P. M. Norris, D. W. Johnson, G. M. Martin, C. A. Friehe, and B. W. Berger, 1995: Diurnal evolution of the cloud-topped marine boundary layer. Part I: Nocturnal stratocumulus development. *J. Atmos. Sci.*, **52**, 2953-2966.

Rossow, W. B., and R. A. Schiffer, 1991: ISCCP Cloud Data Products. *Bull. Amer. Meteor. Soc.*, **71**, 2-20.

Rozendaal, M., C. B. Leovy, and S. A. Klein, 1995: An observational study of diurnal variations of marine stratiform cloud. *J. Climate*, **8**, 1795-1809.

Ryan, M., M. J. Post, B. Martner, J. Novak, and L. Davis, 2002: The NOAA Ron Brown's shipboard Doppler precipitation radar. Preprints, Sixth Symp. On Integrated Observing Systems, Orlando, FL, Amer. Meteor. Soc., 46-48.

Savic-Jovicic, V., and B. Stevens, 2008: The structure and mesoscale organization of precipitating stratocumulus. *J. Atmos. Sci.*, **65**, 1587-1605.

Siems, S. T., D. H. Lenschow, and C. S. Bretherton, 1993: A numerical study of the interaction between stratocumulus and the air overlying it. *J. Atmos. Sci.*, **50**, 3663-3676.

Shank, L. M., S. Howell, A. D. Clarke, S. Freitag, V. Brekhovskikh, V. Kapustin, C. McNaughton, T. Campos, and R. Wood, 2012: Organic matter and non-refractory aerosol over the remote Southeast Pacific: oceanic and combustion sources. *Atmos. Chem. Phys.*, **12**, 557-576, doi:10.5194/acp-12-557-2012.

Slingo, 1989: A GCM parameterization for the shortwave properties of water clouds. *J. Atmos. Sci.*, **46**, 1419-1427.

Slingo, A., and H. M. Schreker, 1982: On the shortwave radiative properties of stratiform water clouds. *Quart. J. Roy. Meteor. Soc.*, **108**, 407-426.

Slingo, A., R. Brown, and C. L. Wrench, 1982a: A field-study of nocturnal stratocumulus. 3 High-resolution radiative and microphysical observations. *Quart. J. Roy. Meteor. Soc.*, **108**, 145-165.

Soden, B. J., and G. A. Vecchi, 2011: The vertical distribution of cloud feedback in coupled ocean-atmosphere models. *Geophys. Res. Lett.*, **38**, L12704, doi:10.1029/2011GL047632.

Stephens, G. L., and T. J. Greenwald, 1991: Observations of the Earth's radiation budget in relation to atmospheric hydrology. Part II: Cloud effects and cloud feedback. *J. Geophys. Res.*, **96**, 15 325–15 340.

Stephens, G. L., 1978a: Radiation profiles in extended water clouds: 1. Theory. *J. Atmos. Sci.*, **35**, 2111-2122.

Stephens, G. L., and T. J. Greenwald, 1991: Observations of the Earth's radiation budget in relation to atmospheric hydrology. Part II: Cloud effects and cloud feedback. *J. Geophys. Res.*, **96**, 15 325-15 340.

Stevens, B., and Coauthors, 2003a: Dynamics and chemistry of marine stratocumulus – DYCOMS-II. *Bull. Amer. Met. Soc.*, **84**, 579-593.

Stevens, B., G. Vali, K. Comstock, R. Wood, M. VanZanten, P. H. Austin, C. S. Bretherton, and D. H. Lenschow, 2005a: Pockets of open cells (POCs) and drizzle in marine stratocumulus. *Bull. Amer. Met. Soc.*, **86**, 51-57.

Taleb, N. N., 2007: *The Black Swan: The Impact of the Highly Improbable*. Random House, 366 pp.

Taylor, J. P., J. M. Edwards, M. D. Glew, P. Hignett, and A. Slingo, 1996: Studies with a flexible new radiation code. 2. Comparisons with aircraft short-wave observations. *Quart. J. Roy. Meteor. Soc.*, **122**, 839-861.

Tang, I. N., 1996: Chemical and size effects on hygroscopic aerosols on light scattering coefficients. *J. Geophys. Res.*, **101**, D14, doi:10.1029/96JD03003

- Terai, C., 2011: Drizzle and the aerosol indirect effect in marine stratocumulus. Thesis, Department of Atmospheric Sciences, University of Washington, 91 pp.
- Tomlinson, J. M., R. Li, and D. R. Collins, 2007: Physical and chemical properties of the aerosol within the southeastern Pacific marine boundary layer. *J. Geophys. Res.*, **112**, D12211, doi:10.1029/2006JD007771.
- Toniazzo, T., S. J. Abel, R. Wood, C. R. Mechoso, G. Allen, and L. C. Shaffrey, 2011: Large-scale and synoptic meteorology in the south-east Pacific during the observations campaign VOCALS-REx in austral Spring 2008. *Atmos. Chem. Phys.*, **11**, 4977-5009, doi:10.5194/acp-11-4977-2011.
- Toniazzo, T., F. Sun, C. R. Mechoso, and A. Hall, 2012: A regional modeling study of the diurnal cycle in the lower troposphere in the south-eastern tropical Pacific. *Clim. Dyn.*, **41**, 1899-1922, doi:10.1007/s00382-012-1598-3.
- Trenberth, K. E., 1997: The definition of El Niño. *Bull. Amer. Met. Soc.*, **78**, 2771-2777.
- Turton, J. D., and S. Nicholls, 1987: A study of the diurnal variation of stratocumulus using a mixed layer model. *Quart. J. Roy. Meteor. Soc.*, **113**, 969-1009.
- vanZanten, M. C., and B. Stevens, 2005: Observations of the structure of heavily precipitating marine stratocumulus. *J. Atmos. Sci.*, **62**, 4327-4342.
- Wang, H., and G. Feingold, 2009: Modeling mesoscale cellular structures and drizzle in marine stratocumulus. Part I: Impact of drizzle on the formation and evolution of open cells. *J. Atmos. Sci.*, **66**, 3237-3256.

Wang, S., and Q. Wang, 1994: Roles of drizzle in a one-dimensional third-order turbulence closure model of the nocturnal stratus-topped marine boundary layer. *J. Atmos. Sci.*, **51**, 1559-1576.

Wark, D. Q., G. Yamamoto, and J. Lienesch, 1962: Infrared flux and surface temperature determinations from TIROS radiometer measurements. Meteor. Sat. Lab. Rep. 10, Weather Bureau, Washington, D.C., 84 pp. [Available from NOAA/NESDIS, Room 703, 5200 Auth Rd., Camp Springs, MD 20746].

Weare, B., 1996: Evaluation of the vertical structure of zonally averaged cloudiness and its variability in the Atmospheric Model Intercomparison Project. *J. Climate*, **9**, 3419-3431.

Wilbanks, M. C., 2013: Near surface density currents observed in the southeast Pacific stratocumulus-topped marine boundary layer. Thesis, Department of Marine, Earth, and Atmospheric Sciences, North Carolina State University, 163 pp.

Wood, R. 2005a: Drizzle in stratiform boundary layer clouds. Part I. Vertical and horizontal structure. *J. Atmos. Sci.*, **62**, 3011-3033.

Wood, R., 2012: Review – Stratocumulus Clouds. *Mon. Wea. Rev.*, **140**, 2373-2423.

Wood, R., and C. S. Bretherton, 2004: Boundary layer depth, entrainment, and decoupling in the cloud-capped subtropical and tropical marine boundary layer. *J. Climate*, **17**, 3576-3588.

Wood, R., and C. S. Bretherton, 2006: On the relationship between stratiform low cloud cover and lower tropospheric stability. *J. Climate*, **19**, 6425-6432.

Wood, R., and D. L. Hartmann, 2006: Spatial variability of liquid water path in marine low clouds: The importance of mesoscale cellular convection. *J. Climate*, **19**, 1748-1764.

Wood, R., K. K. Comstock, C. S. Bretherton, C. Cornish, J. Tomlinson, D. R. Collins, and C. W. Fairall, 2008: Open cellular structure in marine stratocumulus sheets. *J. Geophys. Res.*, **113**, D12207, doi:10.1029/2007JD009371.

Wood, R., M. Köhler, R. Bennartz, and C. O'Dell, 2009: The diurnal cycle of surface divergence over the global oceans. *Quart. J. Roy. Meteor. Soc.*, **135**, 1484-1493.

Wood, R., and Coauthors, 2011a: The VAMOS Ocean-Cloud-Atmosphere-Land Study Regional Experiment (VOCALS-REx): Goals, platforms, and field operations. *Atmos. Chem. Phys.*, **11**, 627-654, doi:10.5194/acp-11-627-2011.

Wood, R., C. S. Bretherton, D. Leon, A. D. Clarke, P. Zuidema, G. Allen, and H. Coe, 2011: An aircraft case study of the spatial transition from closed to open mesoscale cellular convection over the Southeast Pacific. *Atmos. Chem. Phys.*, **11**, 2341-2370, doi:10.5194/acp-11-2341-2011.

Wyant, M. C., and Coauthors, 2006: A comparison of low-latitude cloud properties and their response to climate change in three AGCMs sorted into regimes using mid-tropospheric vertical velocity. *Clim. Dyn.*, **27**, 261-279, doi:10.1007/s00382-006-0138-4.

Wyant, M. C., and Coauthors, 2010: The PreVOCA experiment: Modeling the lower troposphere in the Southeast Pacific. *Atmos. Chem. Phys.*, **10**, 4757-4744, doi:10.5194/acp-10-4757-2010.

Xue, H., G. Feingold, and B. Stevens, 2007: Aerosol effects on clouds, precipitation, and the organization of shallow cumulus convection. *J. Atmos. Sci.*, **65**, 392-406.

Yang, M., and Coauthors, 2011: Atmospheric sulfur cycling in the southeastern Pacific – longitudinal distribution, vertical profile, and diel variability observed during VOCALS-REx. *Atmos. Chem. Phys.*, **11**, 5079–5097, doi:10.5194/acp-11-5079-2011.

Zhang, Y., B. Stevens, B. Medeiros, and M. Ghil, 2009: Low-cloud fraction, lower-tropospheric stability, and large-scale divergence. *J. Climate*, **22**, 4827-4844, doi:10.1175/2009JCLI2891.1.

Zuidema, P., P. E. Westwater, C. Fairall, and D. Hazen, 2005: Ship-based liquid water path estimates in marine stratocumulus. *J. Geophys. Res.*, **110**, D20206, doi:10.1029/2005JD005833.

Zuidema, P., D. Painemal, S. de Szoeki, and C. Fairall, 2009: Stratocumulus cloud-top height estimates and their climatic implications. *J. Climate*, **22**, 4652-4666.

Zuidema, P., D. Leon, A. Pazmany, and M. Cadeddu, 2012: Aircraft millimeter-wave passive sensing of cloud liquid water and water vapor during VOCALS-REx. *Atmos. Chem. Phys.*, **12**, 355-369, doi:10.5194/acp-12-355-2012.

APPENDICES

Appendix A

Peak and Minimum Season Mean Diurnal Cycle Images

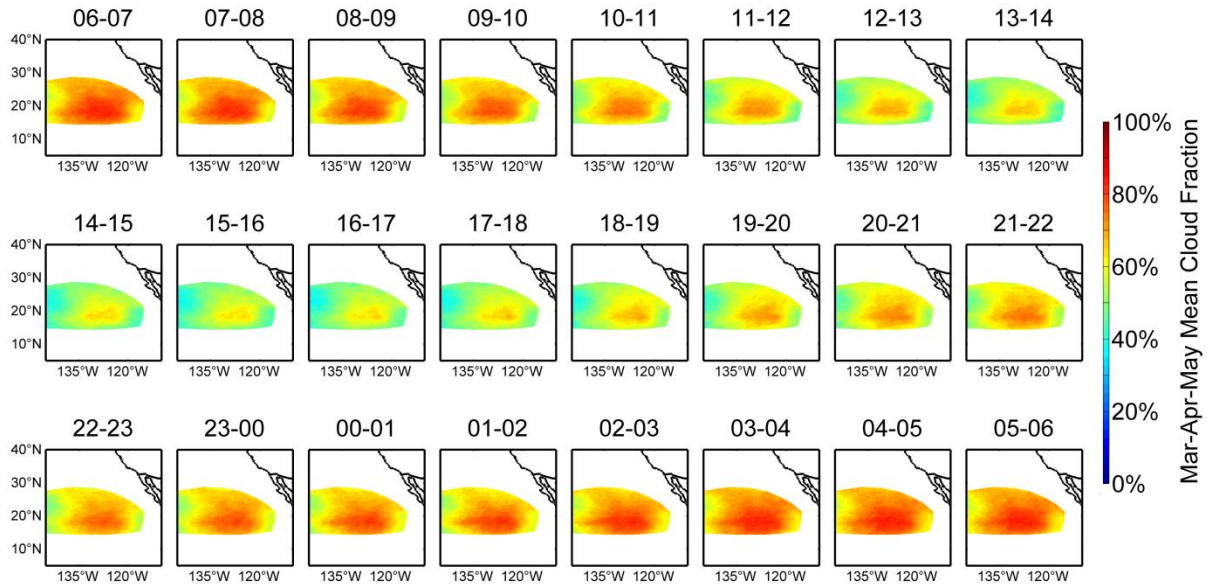


Figure A.1. Hourly mean cloud fractions across the diurnal cycle during the peak cloudiness season (March-April-May) in the NE Pacific.

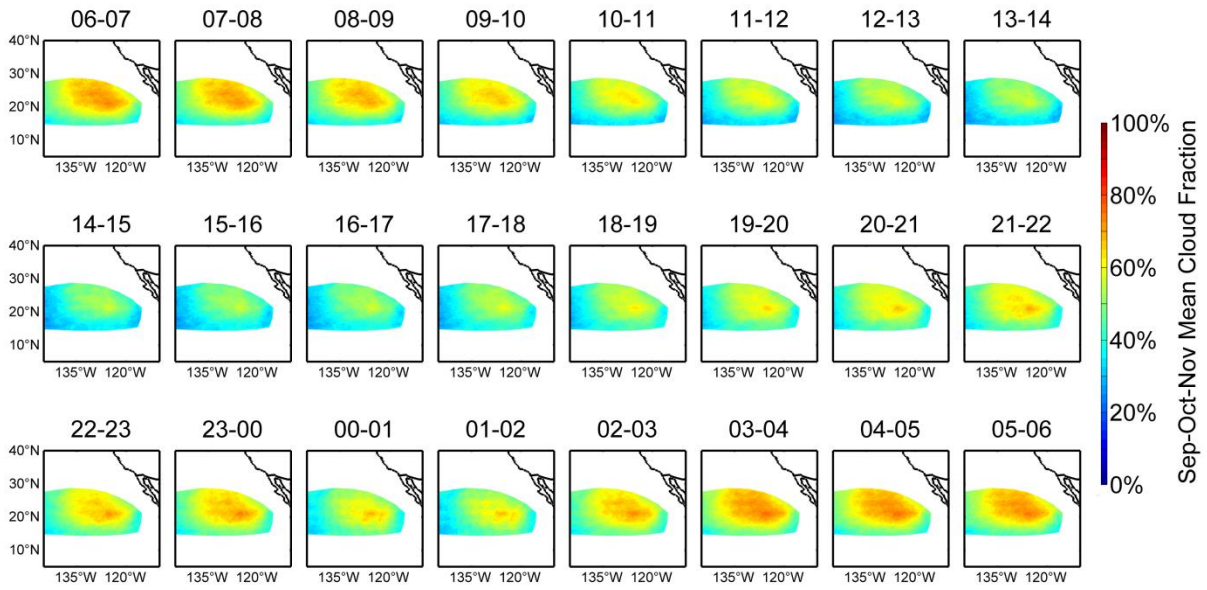


Figure A.2. Hourly mean cloud fractions across the diurnal cycle during the minimum cloudiness season (September-October-November) in the NE Pacific.

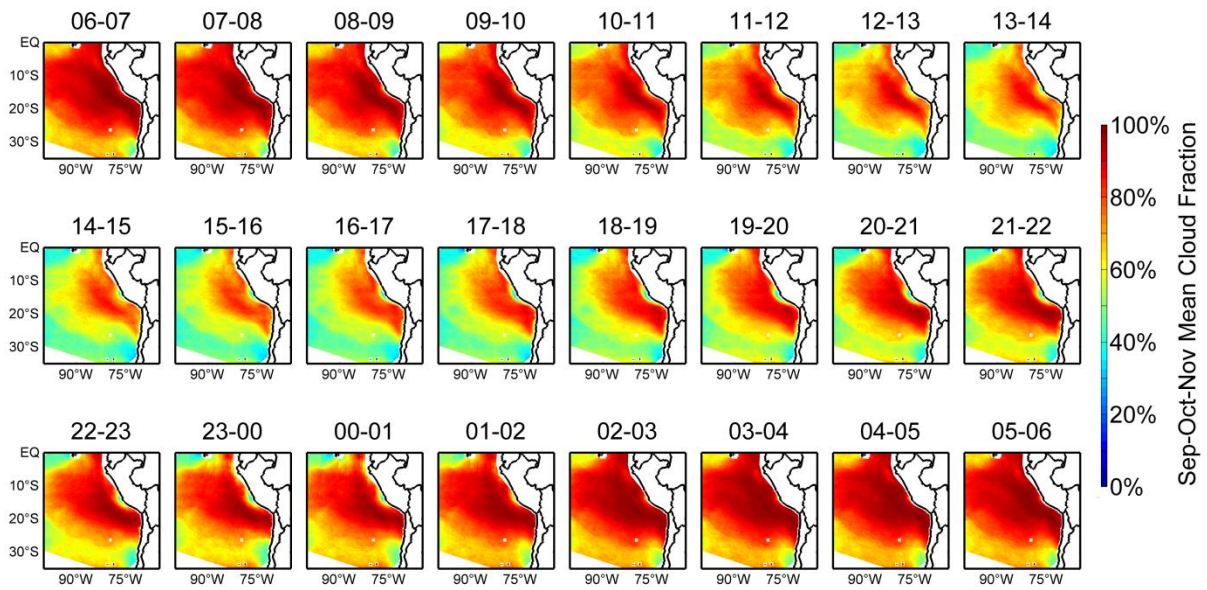


Figure A.3. Hourly mean cloud fractions across the diurnal cycle during the peak cloudiness season (September-October-November) in the SE Pacific.

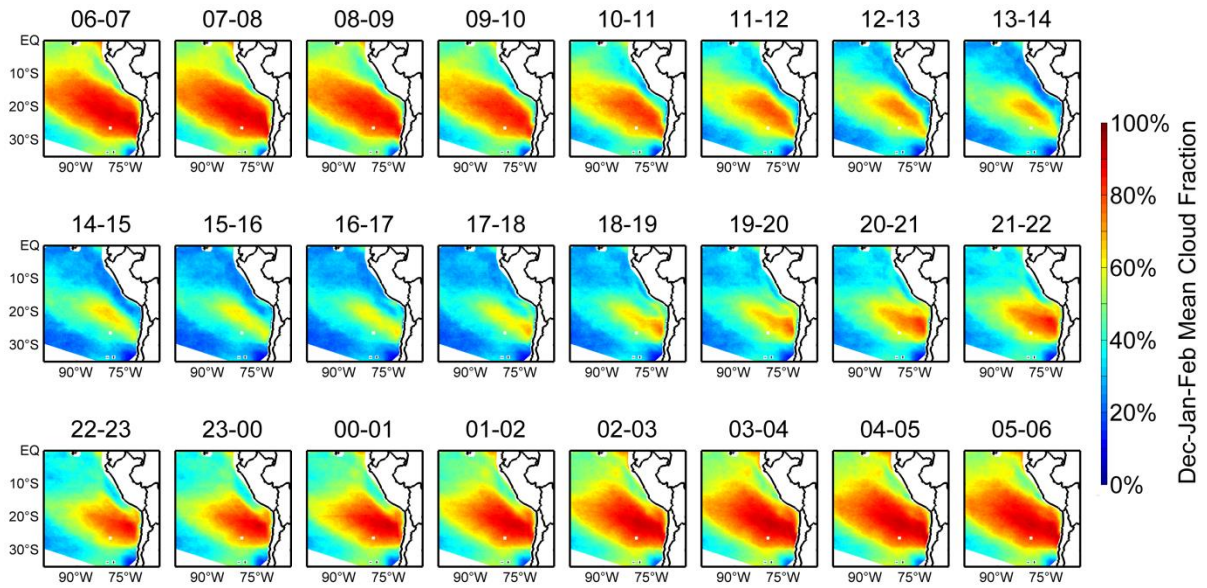


Figure A.4. Hourly mean cloud fractions across the diurnal cycle during the minimum cloudiness season (December-January-February) in the SE Pacific.

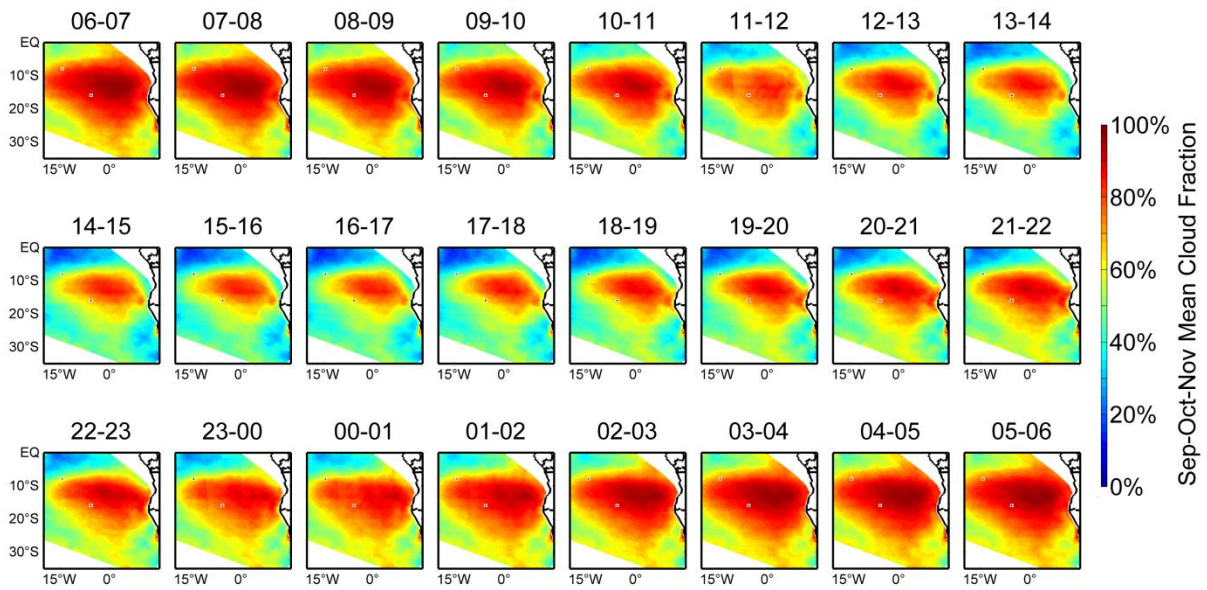


Figure A.5. Hourly mean cloud fractions across the diurnal cycle during the peak cloudiness season (September-October-November) in the SE Atlantic.

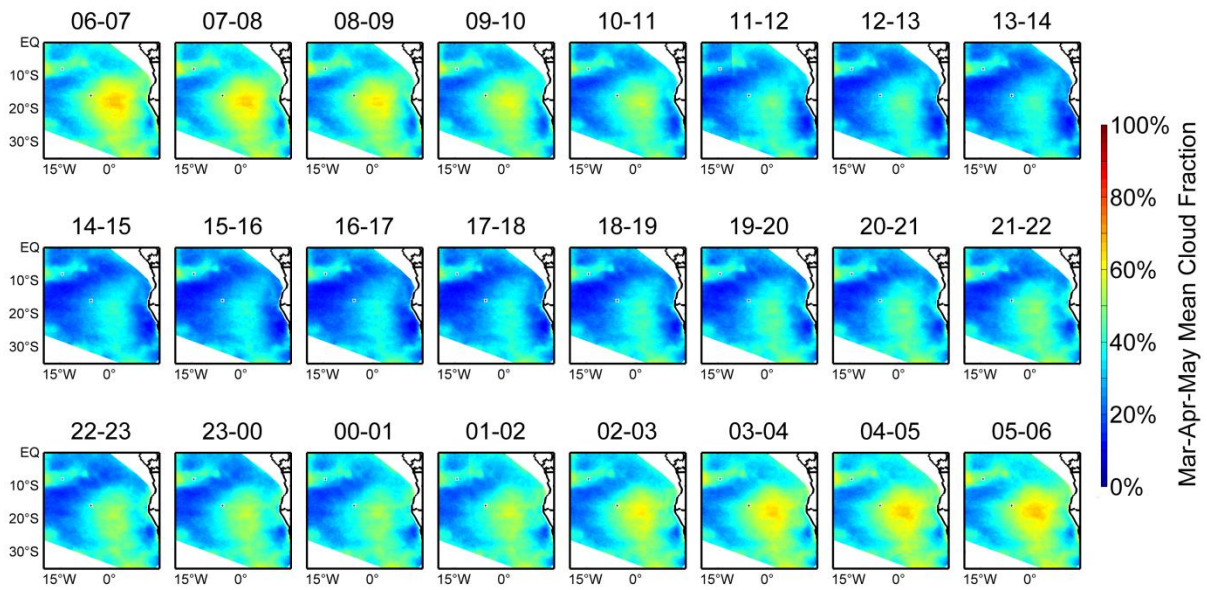


Figure A.6. Hourly mean cloud fractions across the diurnal cycle during the minimum cloudiness season (March-April-May) in the SE Atlantic.

Appendix B

A 10-Year Examination of Precipitation Around Lake Victoria

B.1 Introduction

Lake Victoria in eastern Africa is the primary source of food and fresh water for over 30 million people in the countries of Kenya, Tanzania, and Uganda. The fishing industry built around the lake employs roughly 200,000 people and hydroelectric power generated from the lake is the primary energy source for the region. Since 2005, there have been several well publicized incidents involving ferries and large fishing craft capsizing during severe weather events on the lake (East African Community [hereafter EAC] Report 2011). In addition to the 78 fatalities associated with these tragedies there are an estimated 5,000 weather-related deaths each year from the fishermen who work on the lake (EAC Report 2011). Fishermen, who primarily work at night and in small boats, are often caught in intense thunderstorms that are common to the area. In the vicinity of winds and large waves associated with these storms their boats can capsize and the fishermen often drown as a result. Local meteorological agencies struggle to correctly forecast the location and timing of these storms and to communicate imminent danger to those on the lake.

Information on the nature of the precipitation on and around Lake Victoria is limited. Most of the prior work focuses on long-term climate issues related to water levels in the lake. For example, Mbungu et al. (2012) looked at the climate trends in precipitation extremes during the long (March to May) and short (October to December) rainy seasons. Contributing to the lack of studies is the scarcity of atmospheric data being collected in the region. East African meteorological agencies do make surface weather observations, but all of the data points are inland or on the surrounding shorelines rather than over the lake itself (EAC 2011). Hourly surface reports are incorporated into synoptic map analyses which are used to forecast large scale weather systems. Nowcasting efforts, which might be useful in the case

of fishermen being impacted by severe storms, are largely driven by regional modeling. The lack of a validation dataset over the lake is one of a number of hindrances to efforts aimed at improving the modeling severe storms over the lake (Semazzi et al. 2012).

There have been a handful of relevant studies to build upon. Kizza et al. (2012) used a merged rain gauge and satellite dataset to document the enhancement of rainfall over the lake compared to the surrounding shore. More relevant to this effort, Song et al. (2004) and Anyah and Semazzi (2004) showed the relationship between precipitation location and frequency and the mesoscale circulations associated with topography and the lake itself using a regional climate model. Anyah et al. (2006) built upon these works and used simulations from a fully-coupled regional climate model to examine the role different forcing mechanisms in controlling the location of the heaviest precipitation across the diurnal cycle. The lack of observations over the lake has prevented analysis into the fidelity of these modeling studies at replicating the important components of the atmospheric environment around Lake Victoria.

In this Appendix we document the variability of precipitation in the Lake Victoria basin with the motivation to lay the groundwork for future studies by filling in some gaps in the knowledge base in this sparsely studied region. We use satellite observations of precipitation and reanalysis wind fields over and around the lake to examine various forcing mechanisms thought to be responsible for precipitation variability on diurnal and seasonal scales. The use of satellite data allows us to study similarities and differences in the frequency and intensity of precipitation over the lake compared to the surrounding shores.

B.2 Data and Methods

Due to the near-complete lack of in-situ and remote sensing instrumentation in the region, the analysis we present in this paper relies primarily on satellite data. In particular, we are using a novel high-resolution data product built from the precipitation radar (PR) aboard

the NASA Tropical Rainfall Measuring Mission (TRMM) satellite. Data from the TRMM 2A25 product are aggregated in time at near-native spatial resolution ($0.05^\circ \times 0.05^\circ$) from 1998-2007. This data product is described in more detail in Sobel et al. (2011) and Biasutti et al. (2012). Because the data is used at a very fine native resolution, we must group the data in large blocks of time in order to maintain viable sample sizes. This tradeoff means our data product is suitable for looking at the gross precipitation characteristics of the region, but not for examining individual storms. We use 3-hourly blocks for all 10 years (roughly 200-250 samples at each pixel) to examine the diurnal cycle of precipitation and single month blocks for all hours of the day to look at the seasonal cycle of precipitation (roughly 125-175 samples at each pixel). Each of the three hour blocks used in the diurnal cycle analysis are based on UTC time (i.e. 00-03 UTC, etc.), but times given have been converted to local solar time to ease interpretation. Our analysis focuses on the spatial and temporal variability of precipitation frequency, as changes in frequency (as opposed to intensity) are the primary drivers of variability of tropical precipitation accumulation (Biasutti et al. 2012; Biasutti and Yuter 2013).

To supplement the precipitation observations from the TRMM PR, we use the ERA-Interim reanalysis from the European Center for Medium-Range Weather Forecasting (ECMWF 2009) to get information about the variability of the near surface wind field for the region. The reanalysis data is available every six hours at roughly $0.70^\circ \times 0.70^\circ$ spatial resolution. Model analyzed fields from consecutive six hourly data points are interpolated in time to match the resolution of our precipitation product. All of our data products are available in the $20^\circ \times 20^\circ$ box shown in Fig. A1.

B.3 Results

B.3.1 Diurnal Cycle of Precipitation Frequency

The mean precipitation frequency in three hour time blocks across the diurnal cycle is shown in Fig. B2. Examining the diurnal cycle using the high resolution precipitation product

reveals the detailed spatial variability in precipitation around the lake. As hypothesized in the previous modeling studies, the spatial patterns observed at different times of day can be largely explained in terms of a combination of mesoscale circulations that result from diurnal heating and cooling. The Lake Victoria region provides an interesting place to study these circulations as it combines a significant land-lake breeze with a nearby mountain-valley breeze. Different sectors of the lake combine these circulations in multiple ways across the diurnal cycle. Biasutti et al. (2011; their Fig. 16) contains a clear conceptual schematic of these simple circulations.

Starting from the midmorning hours and into the early afternoon (Fig. B2a; 11:15 am – 2:15 pm), precipitation frequency in the vicinity of the lake is near a diurnal minimum. The most frequent precipitation is located near individual mountain peaks in the highlands of western Kenya. This orographic precipitation results from a combination of the lifting of easterly trade winds as they impinge on the topography and upward motion associated with the daytime mountain-valley circulation, which should be weakly upslope at this time. Precipitation frequency around the lake increases significantly into the afternoon (Fig. B2b; 2:15 pm – 5:15 pm). Precipitation is minimized over the lake, but increases rapidly over the surrounding shoreline as frictional convergence of the onshore lake-land breeze leads to forced ascent over land. Onshore flow is convergent with easterly trade winds on the eastern shore of the lake but is divergent (in the same direction) on the western shore. This east-west difference results in enhanced precipitation immediately onshore on the eastern side of the lake and a reduction in frequency on the western shoreline. In the northeast corner of the lake, onshore flow from the land-lake breeze is also lifted upwards by the topography, resulting in a localized maximum of precipitation frequency on the Kenyan side of the lake. The same general pattern persists through sunset (Fig B2c; 5:15 pm – 8:15 pm).

Thermally induced circulations are weaker in the period just after sunset (Fig. B2d; 8:15 pm – 11:15 pm), resulting in a reduction of precipitation frequency everywhere on and around the lake. The maximum frequency in this window is still located over land on the

eastern half of the lake where the daytime forcing was strongest. The thermally-induced circulations are reversed after midnight and there is, in general, an offshore land-lake breeze and a downvalley mountain-valley breeze. The flow onto the lake from the land results in a slow increase in precipitation frequency over the lake. The highest frequencies over the lake are located in the northeast corner, where the localized curvature of the shoreline results in a convergence of the offshore land-lake breeze (Fig. B2e; 11:15 pm – 2:15 am).

In the window between 2:15 am and 5:15 am (Fig. B2f), flow from the shore onto the lake is strongest as nocturnal cooling over land is maximized. The offshore land-lake breeze converges in the northern half of the lake, resulting in a maximum of precipitation frequency there. The precipitation maximum moves from the northern to the northwestern section of the lake in the time window centered on sunrise (Fig. B2g; 5:15 am – 8:15 am). This period also corresponds to the most frequent precipitation over the lake. The east-west and north-south discrepancy in the location of the most frequent precipitation can be explained by looking at the relationship between the offshore land-lake breeze and the trade winds for the region. On the eastern and southern shores of the lake these two flows are roughly in the same direction. In contrast, the offshore land-lake breeze is convergent with the trade winds on the western and northern shores, resulting in localized frequency maxima over the northern and western portion of the lake. This general pattern persists through the early morning hours (Fig. B2h; 8:15 am – 11:15 am).

B.3.2 Seasonal Cycle of Precipitation Frequency

The monthly mean frequency over the lake and the surrounding shoreline is shown in Fig. B3. The lines represent the mean frequency for all pixels over the lake (blue line) and over land (red line) that lie within the black box in Figs. B3b-d. As Kizza et al. (2012) pointed out, the dominant signal on an annual scale is the bimodal peaks in rainfall frequency that correspond to the long (March through May) and short (October through December) rains. These distinct rainy seasons are coincident with the meridional migration of the Intertropical Convergence Zone (ITCZ) (Kizza et al. 2012). Rainfall during April (Fig. B3b),

corresponding to the south-to-north movement of the ITCZ over the lake, is more frequent over both the lake and the surrounding shoreline compared to the November time period when the ITCZ migrates from north-to-south (Fig. B3d). Easterly trade winds during the long rainy season are more convergent over the lake after they are forced north and south around the terrain in western Kenya. In contrast, during November the winds to the south of the lake remain weak and variable, limiting the amount of surface convergence over the lake from the larger scale wind patterns. Even during the rainy seasons, where frequency is relatively high everywhere, the high spatial resolution precipitation product shows a distinct spatial structure to the frequency patterns over the lake. The most frequent precipitation occurs in the western portion of the lake during both the long and short rainy seasons.

In between the two rainy seasons there are distinct lulls in the precipitation frequency from May through September and January through March. July is the month with the least rainfall of the year. The rainfall frequency map in Fig. B3c shows a near total absence of precipitation over the lake and only scattered and infrequent storms in northern and central Uganda. Because the intensity of the convection does not vary through the year (not shown), the annual cycle of precipitation accumulation very closely resembles the temporal pattern of precipitation frequency.

B.3.3 Differences in Precipitation Over Land Versus Over The Lake

Examining the differences between the properties of precipitation over the lake and the surrounding shoreline provides insight into the underlying processes driving the system. Precipitation is more frequent over the lake compared to the surrounding land (Fig. B3a). The distribution of conditional reflectivity measured by the radar, which is directly related to precipitation intensity, is shown in Fig. B4. Precipitation over the lake is slightly but consistently more intense than over the surrounding shore. This pattern holds at the surface (solid lines in Fig. B4) as well as aloft (dashed lines). The land-shore contrast in intensity is opposite to what might be expected in a hot equatorial region where solar heating of the land

is more intense than over the lake, thus generating increased instability and intense precipitation.

The diurnal cycle of precipitation shows that the spatial distribution of precipitation is highly conditioned on the diurnal variations in the land-lake and mountain-valley mesoscale circulations. The spatial patterns observed combined with the increased intensity over the lake point to a system in which lifting from the collision of mesoscale circulations provides a larger portion of the lifting than does thermal instability.

B.4 Conclusions and Future Work

Precipitation on and around Lake Victoria is examined using a 10 year high resolution dataset from the TRMM precipitation radar. Diurnal variations in the spatial distribution of precipitation demonstrate the influence of thermally-driven mesoscale circulations such as the land-lake breeze and the mountain-valley breeze in determining the timing and location of precipitation. The role of lifting from convergent boundaries is further evidenced by increased storm intensities over the lake compared to the surrounding land.

The local meteorology of Lake Victoria is a complex problem that forecasters in the region struggle with. This work indicates that future efforts to better understand controlling factors in the location and onset storms would be well served to include measurements to determine the exact timing and spatial scales of the land-lake and mountain-valley circulations. The interaction of these two circulations in the northeastern corner of the lake would be an intriguing facet to examine in future field campaigns.

B.5 Appendix B References

Anyah, R. O., and F. H. M. Semazzi (2004): Simulation of the response of Lake Victoria basin climate to lake surface temperatures. *Theor. Appl. Climatol.*, **79**, 55-69.

Anyah, R. O., F. H. M. Semazzi, and L. Xie (2006), Simulated physical mechanisms associated with multi-scale climate variability over Lake Victoria Basin in East Africa, *Mon. Wea. Rev.*, **134**, 3588-3609.

Biasutti, M., S. E. Yuter, C. D. Burleyson, and A. H. Sobel (2012), Very high resolution rainfall patterns measured by TRMM precipitation radar: Seasonal and diurnal cycles. *Clim. Dyn.*, **39**, 239-258, doi:10.1007/s00382-011-1146-6.

Biasutti, M., and S. E. Yuter (2013), Observed frequency and intensity of tropical precipitation from instantaneous estimates. *J. Geophys. Res.*, revised 7/2013.

EAC [East African Community] Report (2011), Enhancing safety of navigation and efficient exploitation of natural resources over Lake Victoria and its basin by strengthening meteorological services. [http://climlab.meas.ncsu.edu/Final_Report_LVBC.pdf]. Authors, Fredrick Semazzi et. al.

European Centre for Medium-Range Weather Forecasts (2009), ERA-Interim Project, <http://rda.ucar.edu/datasets/ds627.0>, Research Data Archive at the National Center for Atmospheric Research, Computational and Information Systems Laboratory, Boulder, Colo. (Updated monthly).

Kizza, M., I. Westerberg, A. Rodhe, and H. N. Ntale (2012), Estimating areal rainfall over Lake Victoria and its basin using ground-based and satellite data. *J. Hydrol.*, **464-465**, 401-411, doi:10.1016/j.hydrol.2012.07.024.

Mbungu, W., V. Ntegeka, F. C. Kahimba, M. Taye, and P. Williams (2012), Temporal and spatial variations in hydro-climatic extremes in the Lake Victoria basin, *Phys. Chem. Earth.*, **50-52**, 24-33, doi:10.1016/j.pce.2012.09.002.

Semazzi, F., S. Benedict, and P. J. van Oevelen (2012), A regional hydroclimate project for Lake Victoria basin (HYVIC), *Global Energy and Water Cycle Experiment (GEWEX) Newsletter*, **22**, 9-12.

Sobel, A. H., C. D. Burleyson, and S. E. Yuter (2011), Rain on small tropical islands. *J. Geophys. Res.*, 116, D08102, doi:10.1029/2010JD014695.

Song, Y., F. H. M. Semazzi, and L. J. Ogallo (2004), A coupled regional climate model for Lake Victoria basin of East Africa. *Int. J. Climatol.*, **24**, 57-75.

B.6 Appendix B Figures

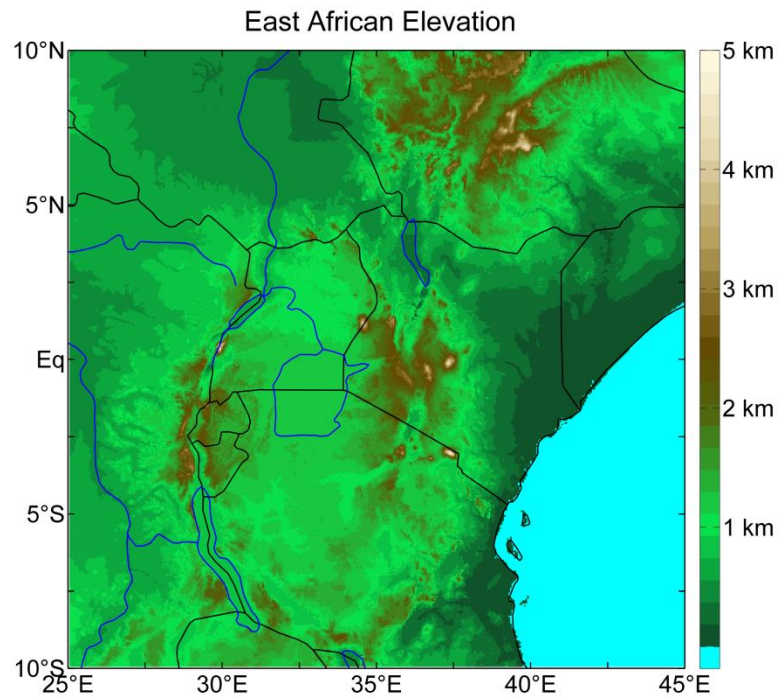
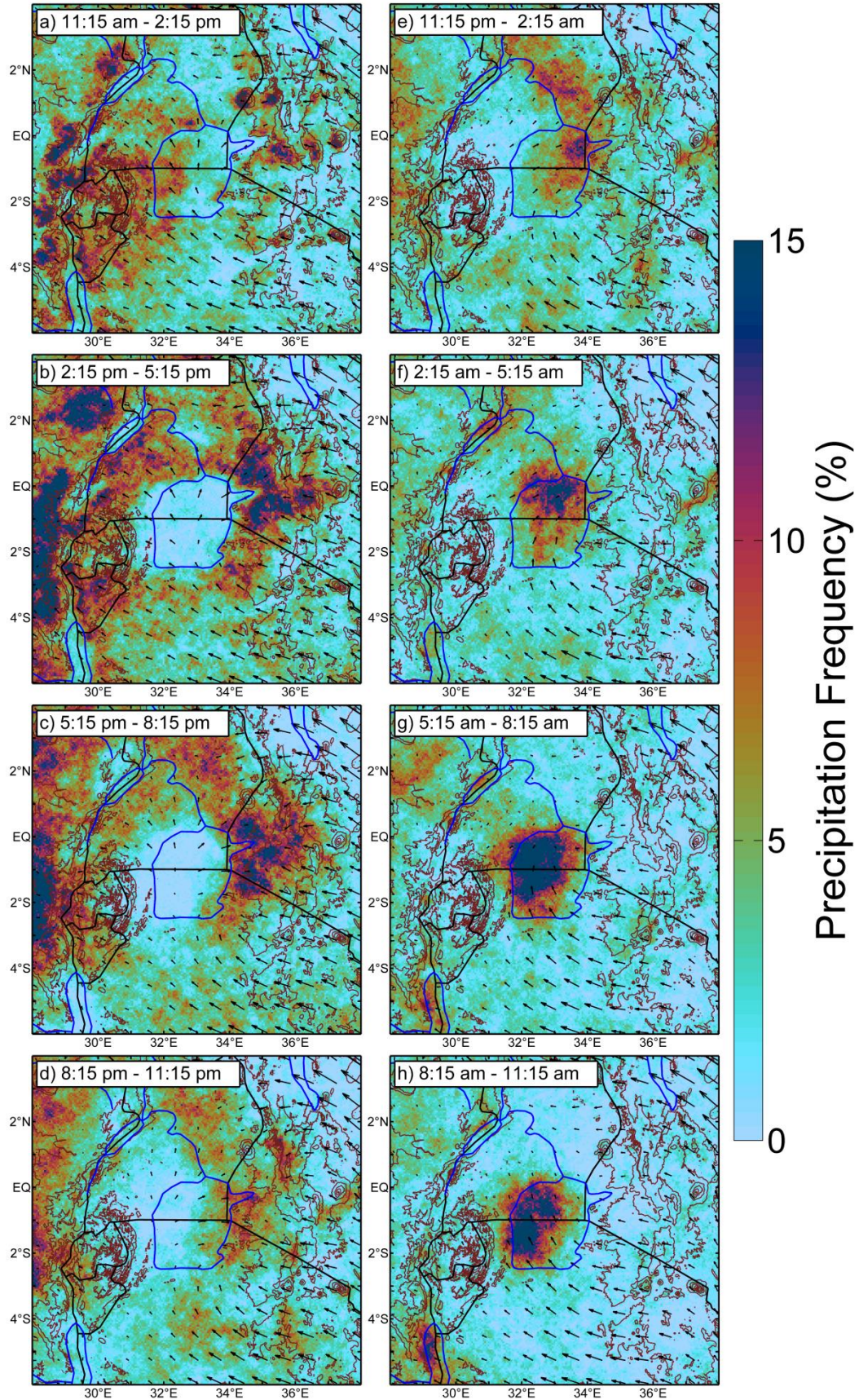


Figure B.1. Elevation in the Lake Victoria region of East Africa. Data are from the Global Land One-km Base Elevation (GLOBE) Project and are gridded at a 1-km spatial resolution.

Figure B.2. Mean precipitation frequency in 3-hour increments across the diurnal cycle. Brown lines are contours of elevation at 750 m intervals. Frequency is defined as the number of rainy pixels divided by the total number of TRMM overpasses at a given pixel. Wind vectors are surface wind speed and direction from the ECMWF reanalysis dataset.



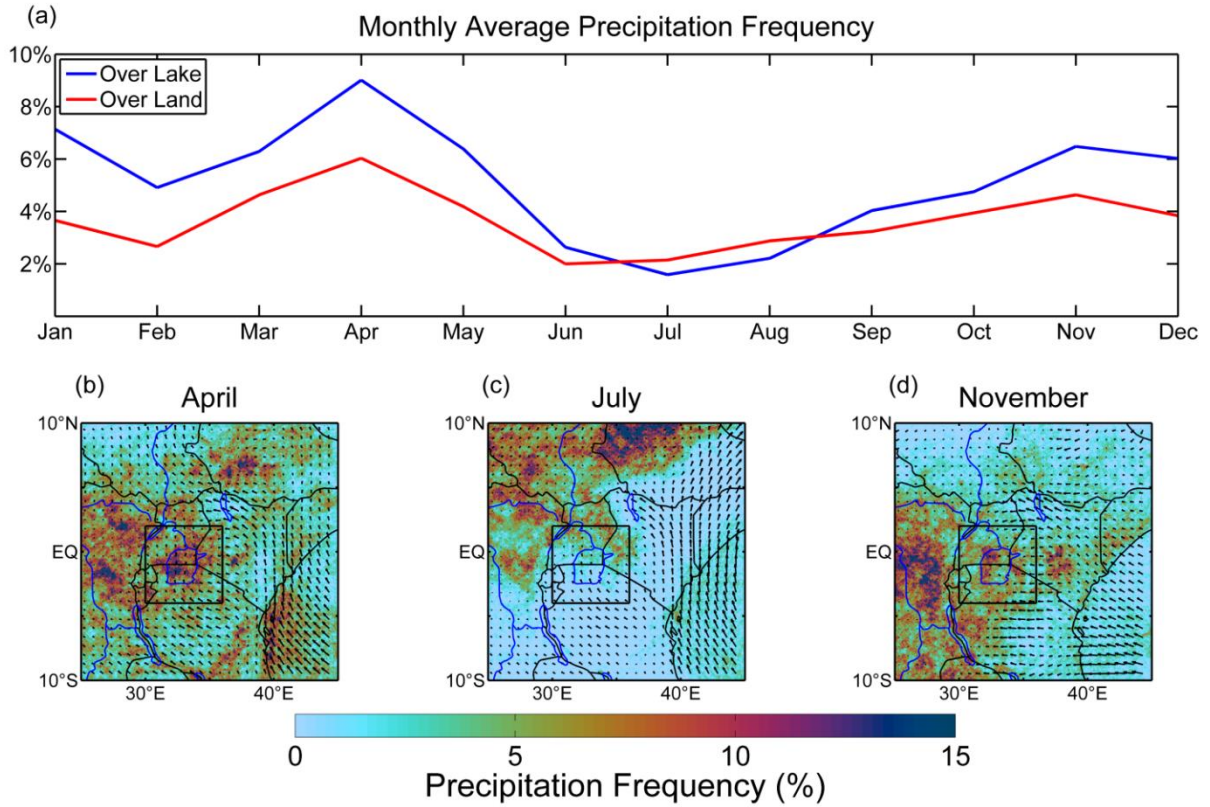


Figure B.3. Monthly mean precipitation frequency over the lake (blue line) and over the surrounding land (red line) with select months shown in the bottom panel. Averaging for the pixels over the lake and over land is done within the black box shown panels b-d. Brown lines are contours of elevation at 750 m intervals. Frequency is defined as the number of rainy pixels divided by the total number of TRMM overpasses at a given pixel. Wind vectors are surface wind speed and direction from the ECMWF reanalysis dataset.

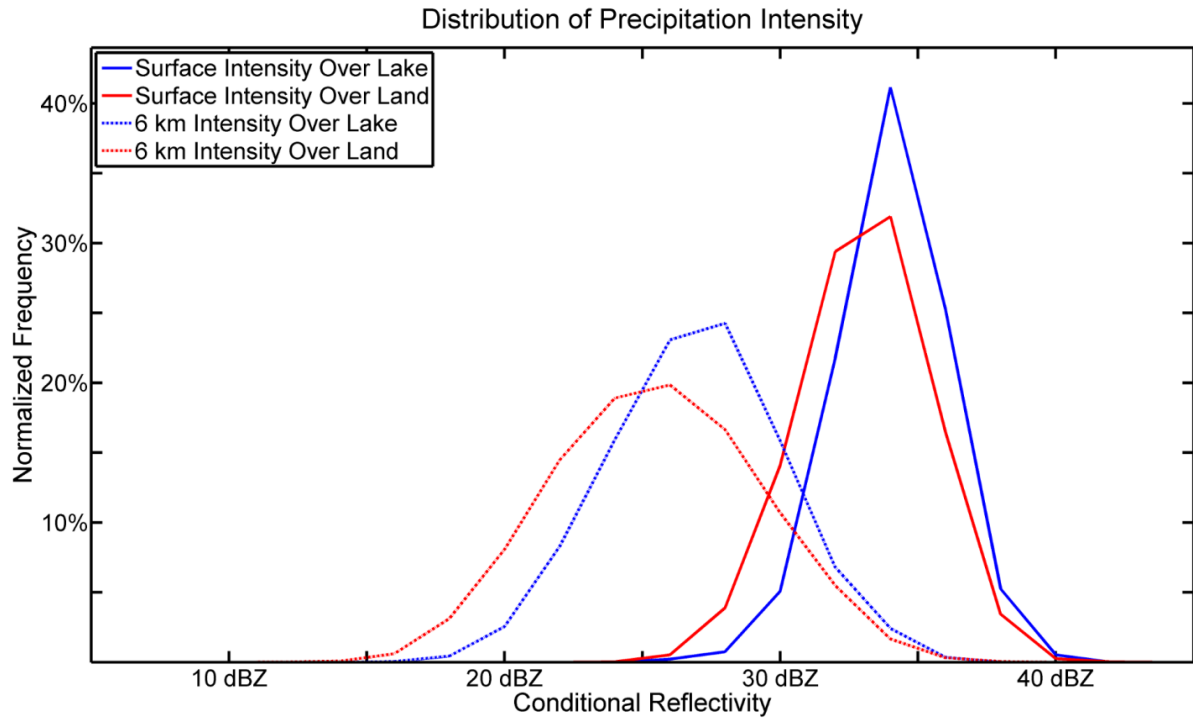


Figure B.4. Distribution of reflectivities for rainy pixels over water (blue lines) and land (red lines) on and around Lake Victoria. The solid lines indicated the distribution of near-surface reflectivity values while the dotted lines indicated the distribution of intensities measured at 6 km. Averaging for the pixels over the lake and over land is done within the black box shown panels b-d of FIG. B3.